Guidance, Navigation, and Control for Very Small Asteroid Mitigation Missions

Y. Garu Sanchez

Technische Universiteit Delft

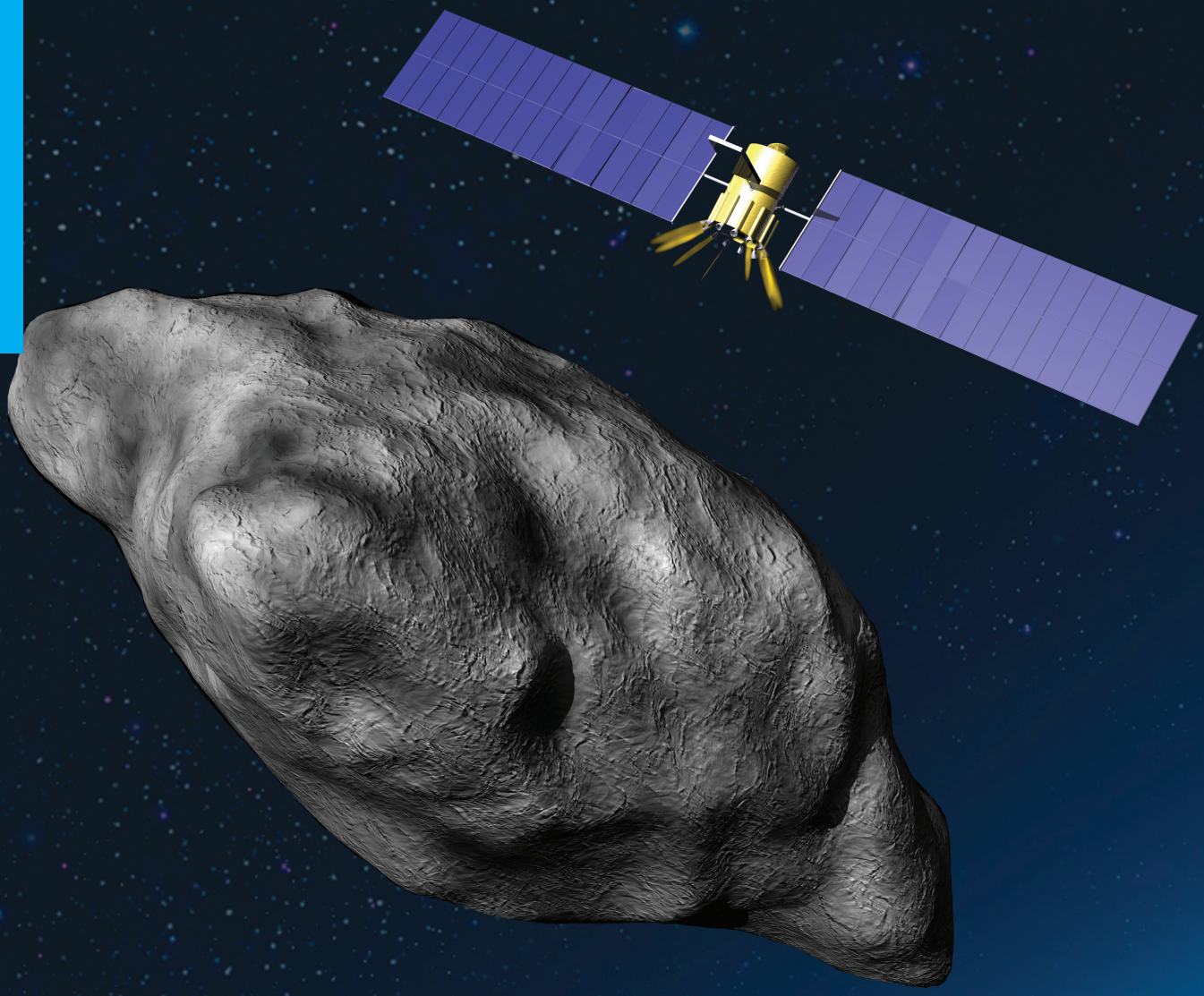

TU Delft Delft University of Technology

Challenge the future

GUIDANCE, NAVIGATION, AND CONTROL FOR VERY SMALL ASTEROID MITIGATION MISSIONS

by

Y. Garu Sanchez

in partial fulfillment of the requirements for the degree of

Master of Science
in Aerospace Engineering

at Delft University of Technology,
to be defended publicly on Wednesday November 29, 2017 at 9:30 AM.

Student number:	4513541	
Supervisors:	Dr. ir. E. Mooij,	TU Delft
	Ir. S. Delchambre,	Airbus Defence and Space GmbH Friedrichshafen
Thesis committee:	Prof. dr. ir. P.N.A.M. Visser,	Astrodynamics and Space Missions, TU Delft (Chair)
	Dr. ir. E. Mooij,	Astrodynamics and Space Missions, TU Delft (Internal examiner)
	Ir. S. Delchambre,	Airbus DS GmbH Friedrichshafen (External examiner, Skype)
	Dr. ir. E. van Kampen,	Control and Simulation, TU Delft (External examiner)

Cover image: courtesy of NEOShield-2 project. Website http://www.neoshield.eu/.

TU Delft Delft University of Technology

ACKNOWLEDGEMENTS

This thesis is the conclusion of two years of hard work and amazing experiences, living in two countries and making friends around the world. However, it would not have been possible without my supervisors Simon Delchambre and Tobias Ziegler. I would like to express my gratitude for giving me the opportunity to develop my thesis in the AOCS department, for their constant support and for allowing me to be part of the NEOShield-2 family.

My special thanks to Erwin, for his constant support providing me with invaluable feedback and material and for his constant monitoring regardless the distance.

On a personal level, I could not find the words to express my gratitude to Nacho, who has helped me in uncountable occasions and has followed me constantly during this two year journey, being a constant support. My special thanks to Charlotte, for the unforgettable moments and her special ability to hear out and solve my problems.

Finally, to Nicolas and Chachou for all the evenings of apéro, cheese and saucisson and to Carmen for avoiding me to sleep in the street during the last 15 days.

Thanking you all,

Y. Garu Sanchez
Friedrichshafen, September 2017

ABSTRACT

Airbus Defence and Space GmbH in Friedrichshafen is the project coordinator of the NEOShield-2 project whose purpose is to develop the technology needed for near-Earth object (NEO) impact prevention. This research is located within the scope of a kinetic impactor mission which typically consists of two spacecraft: impactor and observer. This master's thesis focuses on the latter and starts from a preexisting translational Image Processing (IP) navigation to develop a guidance and control algorithm for the translational motion and a complete guidance, navigation and control (GNC) algorithm for the attitude one. The study focuses on bodies with diameter less or equal than 300 m and the asteroid 2001 QC34 is taken as a baseline. First, the main perturbations influencing the dynamics of the spacecraft are assessed, showing that the best strategy is to do near-inertial hovering. Due to navigation purposes, the objective is set to minimize the amount of manoeuvres needed to keep the spacecraft in the desired location. Classical methods, based on reflecting or inverting the velocity vector, all based on the concept of control box, are simulated showing limitations for long hovering periods. Two new strategies also based on dead-band control theory are shown, one operating at the nominal performance (1 manoeuvre per day) and the second reducing by half these ones (0.5 manoeuvres per day). However, both methods suffer very much from initial conditions and on orbit operations, this being the reason why a second approach is formulated. A method based on Lyapunov control function is proposed showing that it reduces the commanded manoeuvres a ~ 25% with respect to the classical ones (0.6-0.8 manoeuvres per day). It was also found that increasing the control box improves the propellant consumption. For the Lyapunov case, an increment in size of ~ 30% has savings of ~ 8% of propellant.

The study continues with the implementation of the attitude GNC which uses only star tracker measurements for attitude estimation. The absolute performance error (APE) was found to be 0.15 deg, or distributed per axis as [0.005, 0.01, 0.01] deg. This pointing performance is in line with the establish in other space missions such as Rosetta. The main sources of error were found to be the bias of the star tracker and the gyroscopic term coming from angular momentum of the reaction wheels. The latter source can be reallocated per axis changing the initial conditions of these ones. The APE was only lost when translational manoeuvres were performed. This was due to the torque induced into the spacecraft because of thrusters errors. These manoeuvres can cause that the star tracker reach its physical limitations.

Finally, the momentum dumping of the reaction wheels has been studied. Due to the distribution of the propulsion system, a thruster management function needs to be implemented for thrust allocation. For this purpose, linear programming (LP) techniques are used. In particular, using a new approach, and combining machine learning techniques (neural networks) with a pulse-width pulse-frequency (PWPF) modulator. The study shows that although momentum dumping manoeuvres are within the sensor physical limitations, the fact of having both rotational and translational motion coupled and the errors induced by the PWPF modulator, cause that the spacecraft needs to also correct after each desaturation manoeuvre its translational motion. For coarse pointing the method might work, but for momentum dumping where the frequency of the manoeuvres is low, classical methods are preferred as no relevant savings in terms of computational speed can be achieved by the inclusion of DNNs.

CONTENTS

Acronyms and Abbreviations

ACT	Advanced Concepts Team
APE	Absolute Performance Error
BFF	Body-Fixed Frame
CMP	Chemical Propulsion System
DCM	Direction Cosine Matrix
DE	Differential Evolution
DLS	Direct Least-Squares
DNN	Deep Neural Network
E2ESS	End-to-End Science Simulator
EKF	Extended Kalman Filter
EP	Electric Propulsion
ESA	European Space Agency
FoV	Field of View
FVT	Final Value Theorem
GNC	Guidance, Navigation and Control
ICRF	International Celestial Reference Frame
IP	Image Processing
JAXA	Japanese Aerospace Exploration Agency
JPL	Jet Propulsion Laboratory
KF	Kalman Filter
LP	Linear Programming
LQR	Linear Quadratic Regulator
MIB	Minimum Impulse Bit
MRF	Mechanical Reference Frame
MSER	Maximally Stable Extremal Regions
NAC	Narrow Angle Camera
NASA	National Aeronautics and Space Administration
NEA	Near-Earth Asteroid
NEC	Near-Earth Comet
NEO	Near-Earth Object

PaGMO	Parallel Global Multiobjective Optimizer
PD	Proportional-Derivative
PGSO	Photo-Gravitationally Stable Orbit
POSIT	Pose from Orthography and Scaling with ITerations
PSELIKA	Pseudo-Linear Kalman Filter
PWPF	Pulse-Width Pulse-Frequency
PyGMO	Python Parallel Global Multiobjective Optimizer
ReLu	Rectified Linear Unit
SRP	Solar Radiation Pressure
SSSBs	Small Solar System Bodies
SURF	Speed-Up Robust Features
WAC	Wide Angle Camera
YORP	Yarkovsky–O'Keefe–Radzievskii–Paddack

List of Symbols

All symbols used in this study are listed here. Subscripts and superscripts that are self-explanatory are not included. Newton's, Leibniz' notation for a temporal derivative, respectively $\dot{x}$, $\frac{dx}{dt}$, are used in this report. However, for non-temporal derivative x' or $\frac{d}{dx}$ is used equally. The full stop is used to denote the decimal point. Vectors are noted using the bold notation and small letter. Matrices are noted using the bold notation and capital letter. Estimated values are noted by $\hat{x}$ and measured ones by $\tilde{x}$. Unitary vectors are also noted by $\hat{\boldsymbol{x}}$. In both cases, this is clearly stated in the report. The notation of the vectors follows the following rule: left upper corner: reference system; right upper corner: origin; right lower corner: end of vector. The subscript and superscript are dropped out for simplicity when the space is required to express any other attribute. In this case, the reference frame is clearly stated.

Symbol	Meaning (unit)
Roman Letters	
a	Semi-major axis (m)
$\mathbf{a}$	Acceleration vector (m s^{-2})
A	Area (m^2)
$\mathbf{A}$	Distribution matrix
$C_{i,j}$	Harmonic coefficient
$\mathbf{C}$	Direction Cosine Matrix
$\mathbf{d}$	Disturbance vector (m s^{-2} / Nm)
$\mathbf{d}$	Distance vector (m)
e	Eccentricity
f	Force (kg m s^{-2})
$\mathbf{f}$	Force vector (kg m s^{-2})
$\mathbf{g}$	Gravitational acceleration (m s^{-2})
$\mathbf{h}$	Angular momentum (Nms)
$\mathbf{J}$	Inertia tensor (kg m^2)
k	Gain
K	Gain
$\mathbf{K}$	Gain Matrix
m	Mass (kg)
$\mathbf{n}$	Normal vector
$\mathbf{q}$	Quaternion
r	Distance (m)
$\mathbf{r}$	Distance vector (m)
t	Torque (Nm)
$\mathbf{t}$	Torque vector (Nm)
U	Gravitational potential (m^2 s^{-2}
$\mathbf{u}$	Acceleration control vector (m s^{-2} / Nm)
$\mathbf{v}$	Velocity vector (m s^{-1})
x	Cartesian position (m)
$\mathbf{x}$	State vector
y	Cartesian position (m)
z	Cartesian position (m)

Symbol	Meaning (unit)
Greek Letters	
α	Ellipsoid coefficient (x-axis)
β	Ellipsoid coefficient (y-axis)
γ	Ellipsoid coefficient (z-axis)
δ	Latitude (rad)
Δ	Variation
ϵ	Error
θ	Angle (rad)
$\boldsymbol{\theta}$	Angle vector (rad)
λ	Longitude (rad)
μ	Gravitational parameter ($m^3\ s^{-2}$)
μ	Statistical parameter: Bias (rad)
ξ	Damping coefficient
π	Constant
ρ	Average reflectance of a body
σ	Statistical parameter: Standard deviation
σ	Density ($kg\ m^{-3}$)
$\boldsymbol{\tau}$	Torque control vector (Nm)
ω	Natural frequency ($rad\ s^{-1}$)
ω	Angular velocity ($rad\ s^{-1}$)
$\boldsymbol{\omega}$	Angular velocity vector ($rad\ s^{-1}$)

1

INTRODUCTION

Near-Earth objects (NEOs) have impacted and will continue hitting the Earth in the future. Although they have contributed to evolution, as many scientific researches highlight, they have also been responsible for massive extinctions. To avoid this, mitigation measures are being studied.

This thesis focuses on the design of a guidance, navigation and control (GNC) algorithm for an observer spacecraft orbiting a NEO. It is part of the preliminary studies carried out by the NEOShield-2 consortium under the supervision of Airbus Defence and Space GmbH in Friedrichshafen, with the objective, among others, of developing the technology needed for missions in close vicinity of asteroids and comets. This chapter introduces the research objective by first contextualising the problem in Section 1.1. Then Section 1.2 provides information about the previous work developed, which includes previous missions as well as tools and research studies already done on-site. From this information, the research objective together with the mission requirements are formulated in Section 1.3. Finally, the structure of the thesis is given in Section 1.4.

1.1. BACKGROUND

A NEO is by definition any solar system body whose perihelion is less than 1.3 au[1]. Among NEOs, two kinds can be differentiated: near-Earth asteroids (NEAs) and near-Earth comets (NECs).

NEOs impact the Earth every day. Whilst most of them are very small and burn up in the atmosphere, some reach the surface with disastrous consequences. Probably, the most famous recent event is the one occurred in 1908 near the Stony Tunguska River, Siberia, when a 40 m-large asteroid impacted the area, flattening 2000 km^2 of forest and destroying 80 million trees [2]. It is precisely small bodies who suppose a problem, as they are very difficult to detect and anticipate them.

To prevent potential catastrophic damages, mitigation measures could be adopted. Among the possible techniques, there are three that are mainly being investigated: kinetic impactor, gravity tractor and blast deflection. This research is allocated within the scope of the former technique.

A kinetic impactor mission consists of at least two spacecraft, one (impactor) that crashes in the asteroid deflecting the body, and a secondary spacecraft (observer) that measures the asteroid in detail before and after the impact to evaluate the success of the mission. This study focuses on the observer and develops a robust guidance and control algorithm for the translational motion, and a guidance, navigation and control algorithm for the attitude pointing.

This thesis also focuses in small NEO for being the main potential threat. However, this poses an added problem, as the dynamics around the body become complicated due to its irregular shape, weak gravity field and non-trivial solar-perturbation effects.

1.2. MISSION HERITAGE

During the last years, there have been several successful missions to characterize the dynamics around small bodies such as NEAR, Stardust, Hayabusa, Deep Impact, Dawn and most recently Rosetta. However, this

[1] What are NEOs? - NEOShield2 project http://www.neoshield.eu/what-are-neos/. Accessed: 22-07-2017

[2] Threat from NEOs - NEOShield2 project http://www.neoshield.eu/protecting-earth-asteroids-comets-neos/asteroid-neo-impact-threat-earth/. Accessed: 22-07-2017

is just the beginning and new missions are being proposed and launched. Examples are Hayabusa 2 and OSIRIS-REx that are already on their way to asteroids 162173 Ryugu and Bennu, respectively, or AIDA which is currently in preliminary design phases.

As highlighted by NASA's Jet Propulsion Laboratory (JPL) in Quadrelli et al. (2015), the technology used for these missions is still at its early stage and the problem of close-proximity trajectory design for small-body missions represents one of the challenges in GNC that the space industry is going to face in the current decade (2013-2022).

In this section, relevant examples of missions to small bodies are given, together with the approach followed by NEOShield-2.

1.2.1. NEAR

Near Earth Asteroid Rendezvous (NEAR) was a NASA's mission whose objective was to characterize the asteroid 433 Eros. NEAR was launched in 1996 and it was the first mission to orbit and land into an asteroid (Yeomans, 1995). The dimensions of 433 Eros are 34.4 × 11.2 × 11.2 km with a mean diameter value of 16.84 km [3].

To estimate the physical parameters of Eros, the spacecraft was injected into uncontrolled terminator circular orbits of semi-major axis of 50 km and 35 km (Miller et al., 2002). For the orbit determination, optical imaging of landmarks combined with Doppler and range tracking measurements were used.

Regarding the spacecraft characteristics, the spacecraft propulsion system consisted in a main engine of 450 N bi-propellant thruster for large velocity adjustments supported by four 21 N monopropellant thrusters for orbit corrections. Seven 3.5 N monopropellant thrusters were also used for orbit maintenance, attitude corrections and momentum dumping (Santo et al., 1995). The attitude control was completed using a set of four redundant reaction wheels with maximum storage capacity of 4 Nms and maximum torque of 0.025 Nm each, keeping the spacecraft pointing performance below 1.7 mrad (~ 0.1 deg) (Cheng, 2002). Spacecraft attitude determination was obtained using a star tracker, a fully redundant inertial measurement unit, and redundant Sun sensors. The mass of the spacecraft at launch was 787.8 kg.

1.2.2. HAYABUSA

Hayabusa was the first mission to return a sample of material from the surface of a NEO. Impulsed by Japanese Aerospace Exploration Agency (JAXA) and launched in 2003 [4], Hayabusa spacecraft orbited Itokawa before touching down and landing on the asteroid. The dimensions of Itokawa are 540 × 270 × 210 m or a mean average diameter of 330 m[5].

During the observation phase, Hayabusa made use of an optical navigation wide camera with a field of view of 60×60 deg and LIDAR measurements integrated into a Kalman filter (Kominato et al., 2006). Hayabusa was the first mission to employ hovering strategies (i.e. keep the spacecraft in a fixed position relative to the body) for both observation and landing. In particular, Hayabusa used both near-inertial hovering, with the spacecraft fixed in the Sun-NEO frame, and body-fixed hovering, with the spacecraft fixed relative to the NEO (Scheeres, 2016). However, the information about the strategy adopted is very limited and no work so far has been reported on the performance.

Hayabusa had an ion engine system as a primary propulsion system with four thruster heads mounted on two axis gimbals controlled by the attitude and orbit control unit that allowed to control the angular momentum around the perpendicular axes. Furthermore, twelve 20 N monopropellant thrusters were used for orbit corrections, attitude manoeuvres and momentum dumping. These thrusters were located allowing independent translational and rotational motion (Kubota et al., 2006). The attitude control was completed by three reaction wheels exactly aligned with each axis with maximum storage capacity of 4 Nms. Spacecraft attitude determination was obtained using a star tracker, a fully redundant inertial measurement unit, and redundant Sun sensors. The mass of the spacecraft at launch was 510 kg (Uo et al., 2006). Unfortunately, during its operation, the spacecraft suffered the lost of two reaction wheels, forcing the spacecraft to be controlled using the attitude thrusters which lowered the pointing performance. Due to this issue, Hayabusa was also highly ground supported.

[3] 433 Eros, JPL Small-Body Database Browser: http://ssd.jpl.nasa.gov/sbdb.cgi?sstr=433. Accessed: 28-01-2017
[4] Hayabusa, JPL California Institute of Technology: https://www.jpl.nasa.gov/missions/hayabusa/. Accessed: 28-01-2017
[5] Itokawa, JPL Small-Body Database Browser: https://ssd.jpl.nasa.gov. Accessed: 28-01-2017

1.2.3. ROSETTA

Rosetta was an European mission within the ESA's Horizons 2000 Science Programme. It was finally launched in 2004 and its mission was to study the comet 67P/Churyumov-Gerasimenko. It was the first mission to orbit in close proximity of a comet's nucleus, including landing on its surface (Lautenschlager, 2015). The dimensions of Comet 67P/Churyumov-Gerasimenko are $2.3 \times 2.6 \times 1.8$ km (small lobe) and $1.8 \times 4.1 \times 3.3$ km (large lobe)[6].

Terminator orbits of 10×10 km and 10×5 km were used for observing candidate sites for deploying Philae. The navigation system was composed by 4 cameras that were used for relative navigation with different resolutions and field of views (Muñoz et al., 2012). This was the first time that the European Space Agency (ESA) made use of landmark navigation for spacecraft operations.

The spacecraft iwas 3-axis stabilised, controlled with four reaction wheels with 40 Nms momentum storage capacity and able to deliver 0.2 Nm torque. Rosetta made also use of star trackers and laser gyros as attitude sensors (Fiebrich et al., 2004). Ion propulsion system was used as a primary engine and the coarse attitude control and orbit manoeuvres were performed using two redundant sets of 12 bi-propellant thrusters of 10N. Four parallel thrusters for major orbital manoeuvres and eight allocated to produce force free torque for coarse pointing modes and wheel off-loading (Fiebrich et al., 2004). Due to design specifications, the attitude pointing error was limited to 0.05 deg ($8.7 \cdot 10^{-4}$ rad). The total mass (orbiter + lander) at launch was 3000 kg.

1.2.4. OSIRIS-REX

The Origins Spectral Interpretation Resource Identification Security - Regolith Explorer (OSIRIS-REx) is a NASA mission launched in 2016 whose target is the asteroid Bennu. The main objective is to map potential interesting areas and briefly touch the surface and collect samples that will be sent back to Earth about 2023-2025. The diameter of the body is ~500 m (Chesley et al., 2014).

Landmark based optical navigation with the support of a 3D LIDAR is used for orbit determination during the science phase when a 1 km terminator orbit is followed. This phase is the responsible for site selection for the touch and go event. When entering this phase, the characterization of the asteroid will be already completed (Antreasian et al., 2016).

The propulsion system is composed by twenty-eight engines divided into four groups. A main propulsion system of four 275 N thrusters, six medium 22 N thrusters to deliver pitch and yaw control during main engine burns and for accelerating after the touch and go, sixteen 4.5 N thrusters for attitude control and momentum dumping and two ultra-low thrust engines that deliver 0.08 N for high precision operations during the touch and go. The reason for using high thrust propulsion instead of electric propulsion was due to the high accessibility of the asteroid. The attitude determination and control system is completed with four reaction wheels, star trackers, sun sensors and laser gyros. The mass of the spacecraft at launch was 860 kg [7].

1.2.5. NEOSHIELD-2

As stated before, small asteroids are the most likely to hit the Earth, because it is complicated to long term predict a potential impact. The impact of NEOs, however, it is an actual problem that is threatening the Earth everyday. To overcome this, the aim of NEOShield-2 is to demonstrate that with the current technology a kinetic impactor mission could be successfully executed. This implies the use of COTS, as developing new technology requires time. For this reason, NEOShield-2 sets out a cost-effective approach to design the spacecraft. For this study, 2001 QC34 has been chosen as a baseline asteroid (mean average diameter of 190 m). The motivation behind the selection resides in the fact that 2001 QC34 is considered a potential threat for the Earth due to its orbit and to its previous and estimated future close approaches. Furthermore, simulations have shown that after a mitigation action, the minimum encounter distance always increases which ensures that the target moves away from the Earth trajectory. The very low risk of the mission makes this asteroid a perfect candidate [8].

The spacecraft is similar to the one developed for Rosetta mission. Electric propulsion is used as a main propulsion system, together with twelve monopropellant 20 N thrusters. Four of these thrusters are located in the same direction of the electric propulsion system to use them for orbit corrections and orbit mainte-

[6] Comet 67P/Churyumov-Gerasimenko - Vital Statistics: http://www.esa.int/spaceinimages/Images/2015/01/Comet_vital_statistics. Accessed: 28-01-2017

[7] OSIRIS-REx Spacecraft - Spaceflight 101: http://spaceflight101.com/osiris-rex/osiris-rex-spacecraft-overview/. Accessed: 28-05-2017

[8] NEOShield2 project http://www.neoshield.eu/

nance. Coarse attitude manoeuvres and momentum dumping is provided by the rest, allowing independent translational and rotational motion. The spacecraft is 3-axis stabilised, controlled with four reaction wheels. It also counts with three star trackers, redundant inertial measurement units and sun sensors. The optical navigation is composed by two cameras with different field of views (wide and narrow ONC). The narrow angle camera (NAC) has a field of view of 10.3° with a pixel resolution of 2048 × 2048, whereas the wide angle camera (WAC) has a field of view of 21.8° with a pixel resolution of 1024 × 1024. The total mass of the spacecraft with 20% of margin is expected to be 667.5 kg at launch. The selection of ADCS sensors and actuators have been recommended by DEIMOS Space, whose properties will be given along this study. The location of these components can be found in Appendix B, together with the spacecraft properties at arrival. An overview of the spacecraft in deployed configuration is given in Figure 1.1.

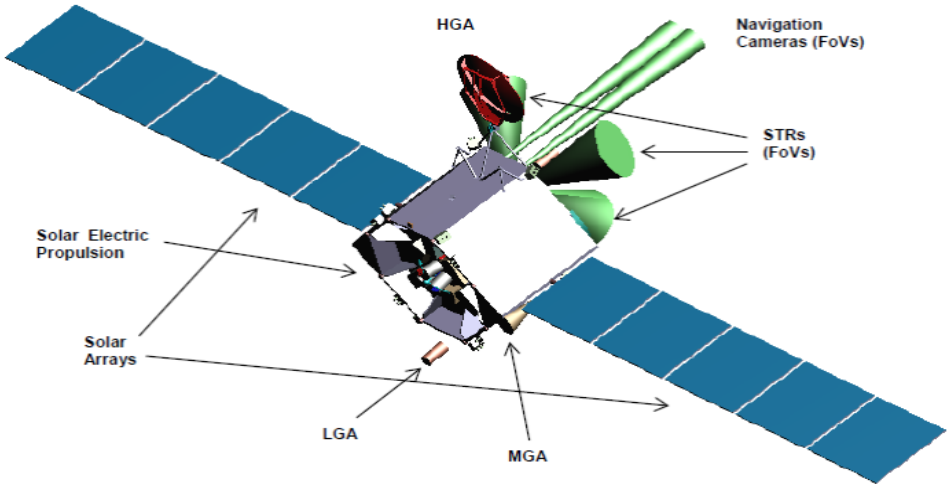

Figure 1.1: Overview of the observer spacecraft in deployed configuration (Ziegler and Delchambre, 2016).

In Delchambre et al. (2017b); Harbulot (2017) and Maurice and Delchambre (2016), an IP based navigation with limited computational cost (star tracker + accelerometer + monocamera) was developed together with a high fidelity end-to-end science simulator (E2ESS) that models the translational motion of the spacecraft around 2001 QC34. The simulator has been validated using Airbus in house tools and includes all the major accelerations acting in the environment. The details about the navigation algorithm behind it can be found in Section 3.2.

In this sense, the simulator provides a perfect environment to test different strategies for designing the guidance and control algorithm for the translational motion. However the frequency of the simulator is not high enough (1/60 Hz) to provide support for the attitude dynamics and a dedicated attitude simulator must be implemented for this purpose. Validated Airbus libraries specially created for handling quaternion operations have been used to speed up the implementation process.

1.3. RESEARCH OBJECTIVE

So far, most of the missions carried out have selected NEOs in which terminator orbits are allowed because the gravitational acceleration is high enough to keep the spacecraft in orbit. Hayabusa was the first one to abandon this approach, suggesting the use of hovering techniques to control the relative position of the spacecraft with the NEO. However, few documentation regarding the performance of hovering techniques or strategies followed are available. This study will evaluate potential uncontrolled orbit strategies around the NEO but it will focus on hovering techniques, as Hayabusa approach suggests to be the best solution around very small bodies.

This thesis seeks to go one step forward regarding the size of the NEO and tackle the problem of close-proximity trajectory design at Small Solar System Bodies (SSSBs) with a diameter less than 300 m, in particular around asteroid 2001 QC34. Attitude dynamics will be integrated to see the influence of orbit operations with respect to the pointing performance. Furthermore, a command sent from the Earth to a spacecraft orbiting a NEO can take up to 30 min to arrive. This communication delay makes the operations near the asteroid

critical when orbiting in close proximity and demands the need for autonomy. The spacecraft must be able to operate autonomously to avoid a potential collision with the NEO in case of any failure. With this information, the research objective is formulated as:

> *The research objective is to investigate the feasibility, safety and robustness to autonomously control a spacecraft to hover in the close proximity of a Small Solar System Body (SSSB) with a diameter less than 300 m and to determine (if feasible) its performance.*

To address the research objective, the study will answer two research questions:

1. Is it feasible to hover autonomously around 2001 QC34 in a safe and robust way with the current baseline spacecraft?
   - 1.1. What are the forces that drive the motion of the spacecraft and how is the spacecraft affected by these ones?
   - 1.2. Which is the distance recommended to hover in a safe way?
   - 1.3. Is the opNav system able to allow hovering manoeuvres with an accuracy and update rate enough to ensure safe conditions?
   - 1.4. Is the control algorithm robust enough to deal with the operational conditions?
2. What is the performance of the GNC system?
   - 2.1. Does the GNC system ensure the minimum performance requirements?
   - 2.2. What is the autonomy of the spacecraft and how many manoeuvres per day are required?
   - 2.3. What is the ΔV needed to hover 2001 QC34?
   - 2.4. What is the nominal pointing performance?
   - 2.5. What is the impact of external disturbances on pointing performance?
   - 2.6. What is the impact of sensors and actuators on pointing performance?
   - 2.7. What is the impact of orbital and momentum dumping manoeuvres on pointing performance?

Mission requirements given in Table 1.1 must be met by the spacecraft to ensure a minimum performance for both translational and rotational motion.

1.4. REPORT OUTLINE

To solve the research problem the master's thesis is structured as follows: Chapter 2 gives the reference frames needed for the research, it also studies the environment and the different forces and torques acting on the spacecraft and concludes providing the equations of motion. Chapter 3 is focused on the translational GNC and it starts by reviewing the different options to orbit around the NEO (guidance) and once the orbit strategy is selected develops a control algorithm. Chapter 4 develops a guidance, navigation and control algorithm for the attitude pointing including the unloading of reaction wheels. Finally, Chapter 5 presents the conclusions and recommendations for future work.

Table 1.1: NEOShield-2 top level requirements.

ID	Requirement
NS-FUN-01	The GNC system shall provide autonomous translational and rotational GNC function for close proximity operations.
Rationale	Although not essential to mission feasibility, longer GNC autonomy is seen as attractive in order to reduce operational cost (manpower and ground station fees), and potentially reduce the number of interruptions to science operations caused by the S/C going into collision avoidance mode.
NS-FUN-02	The GNC system shall be able to provide 3-axis attitude control in the observation mode.
Rationale	The spacecraft needs to be controlled independently in the three axis to: observe 2001 QC34, as the NEO has to be centered in the image of the optical camera, and communicate with the Earth.
NS-GNC-01	The spacecraft shall remain within the specified boundaries with a maximum error less than 5% of the size of the control box with an accuracy and confidence of 95%. The size of the control box is TBD.
Rationale	Chemical propulsion is used for orbit corrections, introducing the impossibility of continuously thrust and thus, needing a boundary limit to actuate. Here a control box includes any geometry that limits the boundaries. A square box was used as a control box in Hayabusa mission.
NS-GNC-02	The spacecraft shall not exceed 2 orbit manoeuvres per day with an accuracy and confidence of 95%.
Rationale	Thruster activation affects the performance of the navigation system. Long periods without any thrust activity are desired.
NS-GNC-03	The spacecraft shall not exceed a ΔV of 4 cm/s per day with an accuracy and confidence of 95%.
Rationale	Hayabusa near-inertial hovered from 20 to 3 km distance to Itokawa. At 5 km distance from 2001 QC34, a ΔV of 1.5 cm/s is needed to compensate the accelerations acting in the spacecraft during one day. This would be the case of continuously thrust in the reference position (low propulsion) which is technically not possible. 4 cm/s per day allows to compensate displacements from the reference position apart from the nominal accelerations.
NS-GNC-04	The absolute performance error shall not exceed an absolute value of 0.05 deg with 3σ accuracy with a confidence of 95%. Distributed along the three axis this implies an error of 0.05/3 deg per axis.
Rationale	Rosetta absolute performance error was limited to 0.05 deg during the observation phase.
NS-GNC-05	The angular velocity shall not exceed an absolute value of 1.25 deg/s with 3σ accuracy with a confidence of 95%.
Rationale	To avoid blurring in the image, a rule of thumb consist of limiting that the image moves more than 1/4 of a pixel during the opening times. Considering the NAC and assuming an opening time of 1 ms, this is: $1/4\,\text{pixels} \cdot 10.3\,\text{deg}/2048\,\text{pixels} \cdot 1/0.001\,\text{s}$.

2

SPACECRAFT-NEO DYNAMICS

Before tackling the problem of GNC design, it is important to evaluate the environment in which both spacecraft and NEO coexist and assess the different accelerations and torques that will drive the relative motion between the two bodies. To describe the dynamics of a certain body with respect to another, reference frames are required.

The aim of this chapter is to do that and it is structured as follows. Section 2.1 introduces the different reference frames that will be used throughout this study together with the different transformations between them. Then, in Section 2.2, the influence of the forces and torques acting in both spacecraft and NEO are evaluated. Finally, the chapter concludes with the formulation of the equations of motion that will be used through the thesis (Section 2.3).

2.1. REFERENCE FRAMES

The concept of reference frame is abstract and the type used is usually related to the suitability for representing the movement of a certain body with respect to a set of reference points. Reference frames can be classified as inertial or non-inertial and the main difference between them resides in the appearance of fictitious forces in the latter or, in other words, Newton's laws only hold for inertial reference frames.

As stated before, the definition of a reference frame is based on its suitability for representing a certain movement. For example, a reference frame used for describing the motion of the Solar System might not be the ideal for describing the relative motion between two bodies, or a reference frame used for describing the relative motion between two bodies, the ideal for describing components within the spacecraft. This fact provokes that in practice, several reference frames are used.

INTERNATIONAL CELESTIAL REFERENCE FRAME (J)

The International Celestial Reference Frame (ICRF) is located at the center of mass of the Solar System and their axes point towards distant quasars and active galactic nuclei. Because of the distance to these objects no relative motion is observable, representing thus the most accurate choice for expressing the dynamics of celestial objects both in and outside the Solar System (Wakker, 2015). The realization of ICRF was made to coincide almost exactly with the J2000 frame, for that reason both are considered to be the same (NASA/NAIF, 2017). The notation J is used for simplicity when writing the equations. This frame is used in the E2ESS for integrating the dynamics of the spacecraft, 2001 QC34 and other relevant Solar System bodies. It helps to locate the NEO as a function of the central body and allows to observe the relative distances with respect to other bodies.

NEO INERTIAL FRAME (NCI)

Following the same definition of ICRF but locating the origin in the asteroid center of mass, the NEO inertial frame is obtained. This reference frame allows to express the motion centered in the small body center of mass and provides a direct motion of the spacecraft around the body of interest.

NEO ROTATING FRAME (NEOS)

For certain analysis or for data visualization, it is useful to define a reference frame that contains the motion of the spacecraft relative to both a central body (the Sun) and the body of interest (the NEO).

The NEO rotating frame is then defined within the context of the restricted three-body problem (Sun-NEO-spacecraft). The x-axis is pointing along the Sun-NEO line, the z-axis is perpendicular to the small-body orbital plane and the y-axis completes the right-hand frame. Its origin is the center of mass of 2001 QC34 and this frame rotates at the same rate as the NEO does around the Sun. The direction cosine matrix (DCM) transforming from J2000 to neoS is obtained as:

$$\mathbf{C}^{\mathrm{J}}_{\mathrm{neoS}} = \left[{}^{\mathrm{neoS}}\mathbf{x} \quad {}^{\mathrm{neoS}}\mathbf{y} \quad {}^{\mathrm{neoS}}\mathbf{z}\right] \tag{2.1}$$

where

$${}^{\mathrm{neoS}}\mathbf{x} = {}^{\mathrm{J}}\mathbf{d}_{\mathrm{NEO}} \,/\, |{}^{\mathrm{J}}\mathbf{d}_{\mathrm{NEO}}| \tag{2.2}$$

$${}^{\mathrm{neoS}}\mathbf{y} = \mathrm{RHS} \tag{2.3}$$

$${}^{\mathrm{neoS}}\mathbf{z} = \left({}^{\mathrm{J}}\mathbf{d}_{\mathrm{NEO}} \times {}^{\mathrm{J}}\mathbf{v}_{\mathrm{NEO}}\right) / |{}^{\mathrm{J}}\mathbf{d}_{\mathrm{NEO}} \times {}^{\mathrm{J}}\mathbf{v}_{\mathrm{NEO}}| \tag{2.4}$$

NEO BODY-FIXED FRAME (NEOB)

The body-fixed coordinate frame is chosen with its origin at the NEO center of mass and the axes are aligned with the principal axes of inertia of 2001 QC34. The x-axis points along the smallest moment of inertia, the z-axis along the largest and the y-axis according to the right-hand rule. The rotating axis forms 75 deg with respect to the Vernal equinox ($[\cos 75^\circ \; 0 \; \sin 75^\circ]$). All this data is assumed, as no information is available about the shape or rotation axis of 2001 QC34.

This frame is particularly useful for several reasons. The spacecraft relative state provided by the IP navigation system is obtained in this frame. Besides, the information about the latitude and longitude is needed in order to determine the higher order gravity field (Equation (2.12)). Finally, if body-fixed hovering strategies are required all the parameters are conveniently expressed in this frame.

At reference epoch (January 1st, 2000 at 12:00 GMT), the DCM transforming from the nci frame to the neoB is written as:

$$\mathbf{C}^{\mathrm{J}}_{\mathrm{neoB}} = \begin{bmatrix} 0.9659 & 0 & -0.2588 \\ 0 & 1 & 0 \\ 0.2588 & 0 & 0.9659 \end{bmatrix} \tag{2.5}$$

whereas any NEO attitude after this epoch can be obtained propagating with the angular velocity of the body (Table A.1).

BODY-FIXED FRAME (BFF)

The body-fixed frame (BFF) frame is chosen with its origin at the spacecraft center of mass and its axes aligned with the mechanical reference frame (MRF) (Appendix B). The reason for this is that all the subsystems are referred to this frame in terms of location and DCMs. Complete information can be found in Ziegler and Delchambre (2016) and specific information used in this study in Appendix B. This frame is used for the attitude determination and the rotational dynamics are expressed and integrated in this frame.

SUMMARY

The different reference frames are summarized in Table 2.1. Here, the notation used when expressing the variables in these frames is given together with their origins and axes orientation. J or nci frames will be used to integrate the dynamics of the spacecraft, neoS for analytic analyses, data visualization and guidance and control design, neoB to obtain the gravity field representation and to support the pre-existing IP navigation system and BFF for attitude dynamics.

2.2. NEO ENVIRONMENT

An important aspect when modelling the dynamics around an asteroid is to understand the different forces and perturbations that affect the motion of the spacecraft. In this section, the formulation of the different forces and torques that appear in the proximity of an asteroid together with the assumptions taken for this study are given.

Table 2.1: Summary of the reference frames used. The axes are normalized (i.e, unitary vectors).

Notation	Origin	Axes
J	Solar System Barycentre	x: Mean spring equinox y: Earth's mean equator z: According to right-hand rule
nci	NEO center of mass	Axes parallel to J
neoS	NEO center of mass	x: Sun-NEO CoM vector y: According to right-hand rule z: Angular momentum NEO orbit
neoB	NEO center of mass	x: Smallest axis of inertia y: According to right-hand rule z: Largest axis of inertia
B	S/C center of mass	Axes parallel to MRF

2.2.1. NEO GRAVITY FIELD

Due to the irregularities in the shape and non-uniform mass distribution of the NEOs, the representation of their gravity fields need special treatment. This is typically done using either spherical harmonic expansions or closed-form solutions for a constant density polyhedron. When in close proximity to the body, the latter is preferred as the spherical harmonic expansion diverges at the circumscribing sphere (Scheeres, 2016). In our case, the shape of 2001 QC34 is unknown and a scaled version of Itokawa has been used as a baseline. This is because typically, the information regarding the asteroid's shape and composition is obtained during the characterization phase, which precedes the observation phase. Figure 2.1 shows a finite element representation of the scaled version that will be used during this study.

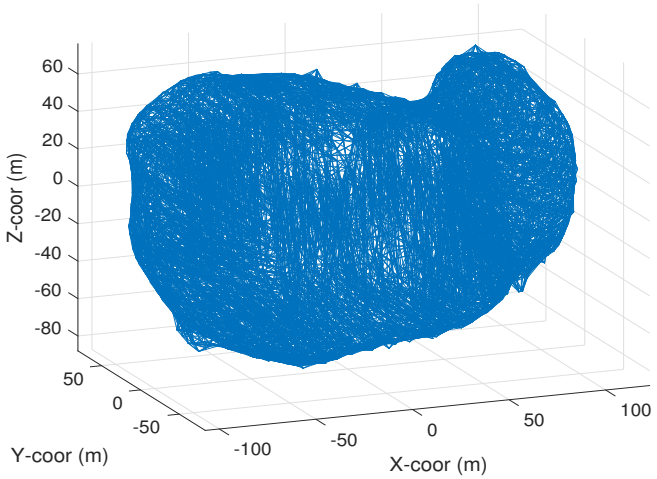

Figure 2.1: Representation of 2001 QC34: Scaled version of Itokawa where the largest axis has been reduced to 230 m and the others adapted to 164 m.

At early stages of the mission, where the mass distribution of the NEO is unknown, an assumption that can be made is to consider the body with uniform mass distribution (i.e, constant density) (Scheeres, 2016). This assumption is then relaxed when an appropriate measurement of the gravity field is done during the characterization phase of the mission. Assuming constant density and given a 3D representation of the NEO (Figure 2.1), the most accurate way to represent its gravity field is using the expression originally developed by Werner for a polyhedron with triangular faces. A summarized version of this method can be found in Scheeres (2016). However, for a detailed development of the expressions, the original paper is recommended, as it also offers a straightforward way for numerical implementation (Werner and Scheeres, 1996). The gravitational potential is given by:

$$U(\mathbf{r}) = \frac{G\sigma_{\text{NEO}}}{2}\left[\sum_{e\,\in\,\text{Edges}} \mathbf{r}_e^T \mathbf{E}_e \mathbf{r}_e L_e - \sum_{f\,\in\,\text{Faces}} \mathbf{r}_f^T \mathbf{F}_f \mathbf{r}_f \omega_f\right] \tag{2.6}$$

whereas the gravity field is given by:

$$\frac{\partial U}{\partial \mathbf{r}} = -G\sigma_{\text{NEO}}\left[\sum_{e\,\in\,\text{Edges}} \mathbf{E}_e \mathbf{r}_e L_e - \sum_{f\,\in\,\text{Faces}} \mathbf{F}_f \mathbf{r}_f \omega_f\right] \tag{2.7}$$

where $\mathbf{E}_e$ denotes a dyadic matrix of an edge, $\mathbf{F}_f$ the outer product of a face normal, and L_e and ω_f dimensionless factors defined as:

$$\mathbf{E}_e = \hat{\mathbf{n}}_f \left(\hat{\mathbf{n}}_e^f\right)^T + \hat{\mathbf{n}}_{f'} \left(\hat{\mathbf{n}}_e^{f'}\right)^T \tag{2.8}$$

$$\mathbf{F}_f = \hat{\mathbf{n}}_f \hat{\mathbf{n}}_f^T \tag{2.9}$$

$$L_e = \ln \frac{r_1^e + r_2^e + e_{12}}{r_1^e + r_2^e - e_{12}} \tag{2.10}$$

$$\omega_f = 2\arctan \frac{\mathbf{r}_1^f \cdot \left(\mathbf{r}_2^f \times \mathbf{r}_3^f\right)}{r_1^f r_2^f r_3^f + r_1^f (\mathbf{r}_2^f \cdot \mathbf{r}_3^f) + r_2^f (\mathbf{r}_3^f \cdot \mathbf{r}_1^f) + r_3^f (\mathbf{r}_1^f \cdot \mathbf{r}_2^f)} \tag{2.11}$$

being G the gravitational constant and $\mathbf{r}_i^f$, $i = 1,2,3$ the vertex vectors that compound each of the faces ordered counter-clockwise with respect to the face normal $\hat{\mathbf{n}}_f$. The two vertex associated to each edge are given by $\mathbf{r}_i^e$, $i = 1,2$ whereas e_{12} denotes the distance of the edge $|\,\mathbf{r}_1^e - \mathbf{r}_2^e\,|$. Finally, each of the edges is linked to two faces (f, f') and $\hat{\mathbf{n}}_e^f$ denotes the vector perpendicular to the edge and to $\hat{\mathbf{n}}_f$, pointing away from the face center. σ_{NEO} represents the density of the body.

The main drawback of the polyhedron model with respect to the spherical harmonic expansion is that it is computationally expensive. As a consequence, a typical approach followed is to use the polyhedron model within the circumscribing sphere and do the transition to the spherical harmonic field for larger radius (Scheeres, 2016).

The general form for the spherical harmonic potential for a gravity field is:

$$U(r,\delta,\lambda) = \frac{\mu_{\text{NEO}}}{r}\sum_{n=0}^{\infty}\sum_{m=0}^{n}\left(\frac{r_0}{r}\right)^n \hat{P}_{nm}(\sin\delta)\left[\hat{C}_{nm}\cos m\lambda + \hat{S}_{nm}\sin m\lambda\right] \tag{2.12}$$

where r_0 the reference radius that is taken as the maximum radius of the body, δ and λ are the latitude and longitude in the body-fixed frame, n is the degree and m is the order and $\hat{P}_{nm}$ are the fully normalized Legendre polynomials and associated functions. The normalized coefficients are related to the regular ones by (Kaula, 2013):

$$\hat{C}_{nm}, \hat{S}_{nm} = \sqrt{\frac{(n+m)!}{(2-\delta_m^0)(2n+1)(n-m)!}}\, C_{nm}, S_{nm} \tag{2.13}$$

where δ_m^0 is the Kronecker delta and equals 0 if $m \neq 0$ and equals 1 if $m = 0$. From previous studies (Scheeres, 2016), it has been found that the second degree and order gravity field accounts for the majority of the perturbations on the dynamical system and thus, it can be used for preliminary analysis.

Choosing the body-fixed coordinate frame to be aligned with the constant density principal axes, Equation (2.12) can then be simplified as:

$$U(r,\delta,\lambda) = \frac{\mu_{\text{NEO}}}{r}\left[1 + \left(\frac{r_0}{r}\right)^2\left\{C_{20}\left(1 - \frac{3}{2}\cos^2\delta\right) + 3C_{22}\cos^2\delta\cos(2\lambda)\right\}\right] \tag{2.14}$$

and assuming that the NEO can be approximated to an ellipsoid with constant density, C_{20} and C_{22} are obtained through (Scheeres, 2016):

$$C_{20} = \frac{1}{5r_0^2}\left(\gamma^2 - \frac{\alpha^2 + \beta^2}{2}\right) \tag{2.15}$$

$$C_{22} = \frac{1}{20r_0^2}\left(\alpha^2 - \beta^2\right) \tag{2.16}$$

α, β and γ are the ellipsoid axes as represented in Figure 2.2.

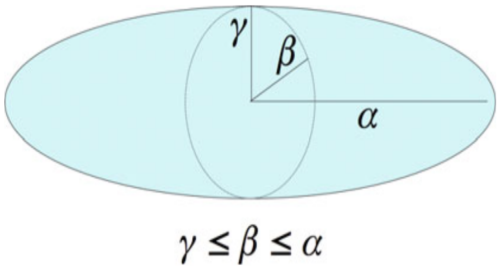

Figure 2.2: Tri-axial ellipsoid (Scheeres, 2016)

To assess the influence of the irregularities of the gravity field as a function of the distance to the NEO, both models have been compared with the point mass gravity model ($\frac{\mu_{NEO}}{r^3}\mathbf{r}$). The gravity field has been computed using a uniform point cloud distribution at different distances (Figure 2.3a) and the gravity field values have been normalized using the point mass gravity model, whose error is shown in Figure 2.3b.

Analysing the results, it can be seen that at distances of the order of hundreds of meters, the variations are up to 15% of the nominal value, which indicates that for accurate representations the constant density polyhedron or higher order spherical harmonics must be used. However, these effects decay with distance (quartically in the case of second degree and order spherical harmonic model) and at distances of thousands of meters the irregularities of the body represent the 2% of the nominal value, being thus a good approximation to assume the body as a point mass to reduce the computational cost.

Based on these results, for preliminary analysis, the constant density polyhedron model will be used to represent the gravity field for distances less than 1 km. However, for larger radial distances, a point mass model will be used for speeding up the computations.

When studying the performance of the translational motion, the E2ESS will be used. The high-fidelity simulator implements a spherical harmonic model of degree and order 10 to achieve accuracy and efficiency in terms of computational cost. The coefficients used can be found in Ziegler and Delchambre (2016). In that sense, the simulator is not prepared for landing manoeuvres, however, as our study focuses on the observer spacecraft, this is also not required.

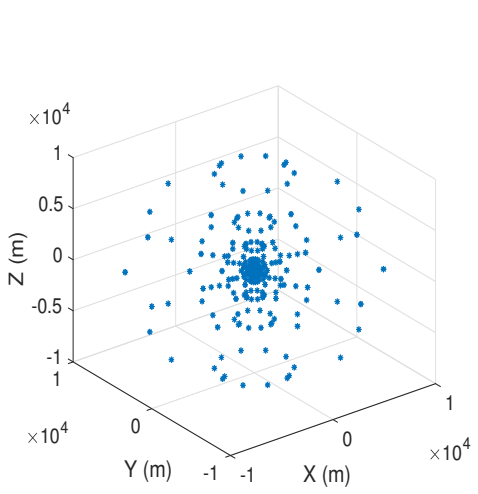

(a) Point cloud distribution in the neoB frame.

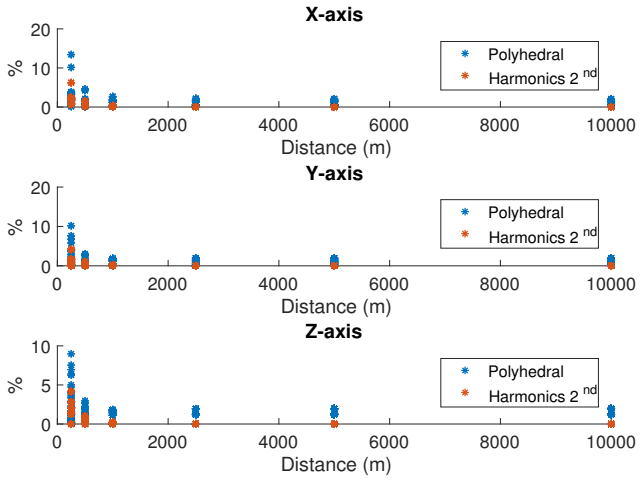

(b) Gravity field magnitude error

Figure 2.3: Polyhedral and spherical harmonics (2^{nd} order) vs point mass three-axis gravity field errors.

GRAVITY TORQUE

Due to the irregularities of the NEOs, analytic solutions for computing the gravity torque cannot be obtained as it is only valid for central gravity fields (Wie, 1998). To solve this problem, discretised models of the spacecraft are used and the resultant torque for N point masses can be computed as (Razgus et al., 2016):

$$\mathbf{t}_g = \sum_{i=1}^{N} \mathbf{r}_m^i \times m^i \mathbf{g}_m^i \tag{2.17}$$

where $\mathbf{r}_m$ represents the distance between a point mass m and the center of mass of the spacecraft. For this study, the spacecraft has been discretised into 33 point masses. The reason for using 33 point masses responds to a trade-off between the number of points and accuracy with respect to the matrix of inertia of the spacecraft (Appendix B). Figure 2.4 shows the point mass distribution where the discretised masses are located along the main components of the spacecraft: solar panels, central box and antenna (HGA) (Figure 1.1).

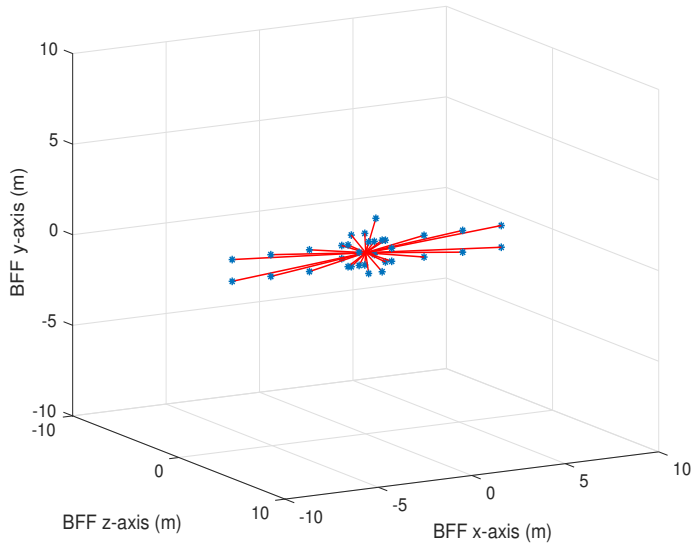

Figure 2.4: Spacecraft point-mass model with their axes in the BFF frame.

Due to the symmetry and span (~ 15 m) of the spacecraft, the strength of the gravity field and the fact that the spacecraft is pointing to the NEO, the gravity gradient torque due to the solar panels is almost negligible and the antenna represents the major contributor. The resultant torque at 5 km distance is of the order of $\sim 10^{-8}$ Nm whereas at 1 km distance the influence increases to $\sim 10^{-6}$ Nm.

2.2.2. SOLAR RADIATION PRESSURE

Considering the size and density of the asteroid and the asteroid distance from the Sun ($a \sim 1$ au), Solar Radiation Pressure (SRP) will be a major contributor to the dynamics of the spacecraft-NEO relative motion. Although a more complicated analysis exists, for a preliminary design it is common to use Equation (2.18) to express the net acceleration (Scheeres, 2016).

$$\mathbf{a}_{SRP} = -\frac{(1+\rho)\, P_0 A_{S/C}}{m_{S/C}} \frac{(\mathbf{d}_{NEO} - \mathbf{r})}{|\mathbf{d}_{NEO} - \mathbf{r}|^3} \tag{2.18}$$

where ρ is the average reflectance or albedo of the body (in this case the spacecraft), P_0 is a solar constant $\approx 1 \cdot 10^8$ kg km^3/s^2/m^2, $A_{S/C}$ is the spacecraft cross-sectional area, $m_{S/C}$ the spacecraft mass, $\mathbf{d}_{NEO}$ the Sun-NEO distance and $\mathbf{r}$ the NEO-spacecraft distance ($\mathbf{d}_{S/C} = \mathbf{d}_{NEO} - \mathbf{r}$). The mass to area ratio is often denoted as $B_{S/C}$ whereas the constant value $\beta_{S/C}$ refers to:

$$\beta_{S/C} = \frac{(1+\rho)\, P_0}{B_{S/C}} \tag{2.19}$$

To observe the NEO surface with an optical camera, it is important to locate the spacecraft close to the Sun-NEO line to have direct view of the illuminated side of the asteroid. Furthermore, to supply power, the solar panels will also be oriented to the Sun. Considering these two arguments, it is reasonable to assume a certain constant cross-sectional area. Note also that this case represents the worst-case scenario, as the acceleration reach its highest value and the spacecraft can end up more easily in the dark side of the NEO, loosing also the IP navigation. At 1 au, and considering the reflectivity to be equal to 0.3 and a cross-sectional area of 18.5 m^2 this acceleration is $\sim 2 \cdot 10^{-7}$ m/s^2.

SOLAR RADIATION PRESSURE TORQUE

For translational motion where the spacecraft can be modelled as a point mass with a certain cross-sectional area, Equation (2.18) represents a reasonable approximation considering an average surface reflectivity. However, when attitude dynamics are introduced, a more detailed model needs to be chosen, as not only the different surfaces, but also their location are important. A high-fidelity in-house tool has been used for this purpose. The software allows to model the spacecraft with the different surfaces and their properties, together with the degrees of freedom of the components. In this case, no degrees of freedom have been assumed for the nominal position and only major components have been represented for being the ones driving the motion (solar panels, high gain antenna and main structure). Figure 2.5 shows the simplified model together with the dimensions of the components expressed in millimetres.

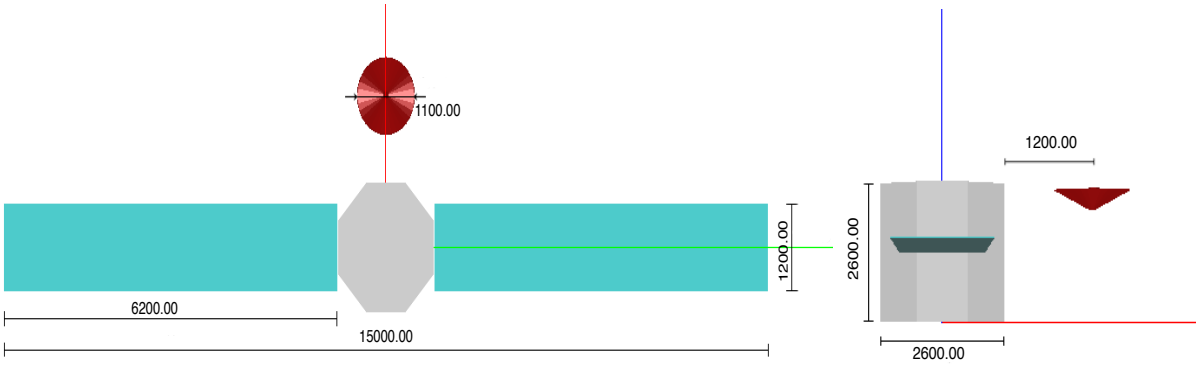

(a) X-Y view

(b) X-Z view

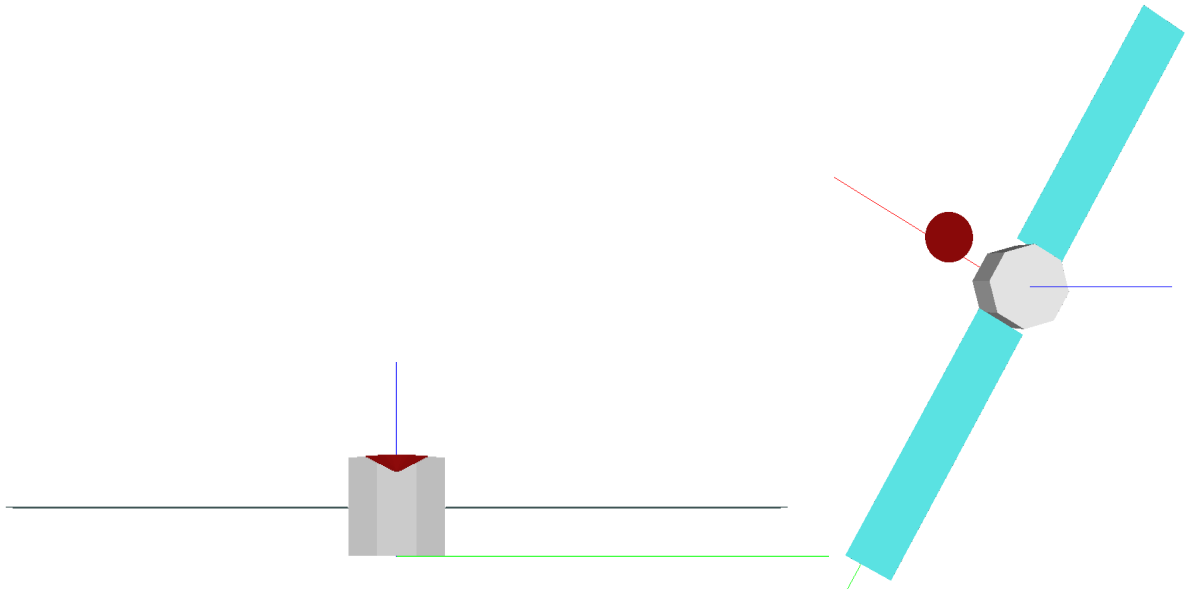

(c) Z-Y view

(d) 3D view

Figure 2.5: Simplified representation of the spacecraft in the MRF. X-axis denoted in red, Y-axis in green and Z-axis in blue.

Table 2.2: Spacecraft reflection coefficients according to the design specifications (Ziegler and Delchambre, 2016).

Material	Absorptivity	Specular reflection	Diffuse Reflection
Solar Array	0.79	0.00	0.21
MLI (body)	0.50	0.43	0.07
Antenna	0.30	0.70	0

The different forces acting on the surfaces of the spacecraft are given by Equation (2.20) (Vallado, 2001).

$$\begin{aligned}\mathbf{f}^i_{\text{SRP}} &= \left(\mathbf{f}^i_{\text{abs}} + \mathbf{f}^i_{\text{sp}} + \mathbf{f}^i_{\text{d}}\right) \\ &= -P_{\odot}\frac{1\text{au}^2}{d^2_{\text{S/C}}}A^i\cos\phi_{\text{inc}}\left[2\left(\frac{c^i_{\text{Rd}}}{3} + c^i_{\text{Rs}}\cos\phi_{\text{inc}}\right)\hat{\boldsymbol{n}}^i + \left(1 - c^i_{\text{Rs}}\right)\hat{\boldsymbol{s}}^i\right]\end{aligned} \tag{2.20}$$

and the net torque produced by each of the individual surfaces is:

$$\mathbf{t}_{\text{SRP}} = \sum_{i=1}^{N}\mathbf{r}^i_A \times \mathbf{f}^i_{\text{SRP}} \tag{2.21}$$

where $P_{\odot} = 4.56\ \mu\text{N/m}^2$, c_{Rs} is the specular reflection coefficient, c_{Rd} the diffusive reflection coefficient and c_{Ra} the absorption reflection coefficient of a subsurface A^i. $\hat{\boldsymbol{n}}^i$ and $\hat{\boldsymbol{s}}^i$ represent the normal vector of a subsurface and the Sun direction respectively. The reflection coefficients values are given in Table 2.2.

Due to the symmetry of the spacecraft the main component driving the SRP torque is the antenna. This component induces a nominal torque at 1 au of approximately 10^{-5} Nm in the negative Y-axis. As compared with Section 2.2.1, this represents the main torque driving the attitude dynamics of the spacecraft. This is because the resultant torque is ~ 1000 times greater than the nominal gravity torque at 5 km distance and it is not until 1 km distance where gravity torque becomes relevant. Thus, the only torque being modelled when orbiting at distances greater than 1 km is the one due to SRP.

2.2.3. THIRD-BODY GRAVITATIONAL EFFECTS AND OTHER PERTURBATIONS

When observing the asteroid, the spacecraft is not only orbiting this body, but also both rotate at the same time around the Sun. Furthermore, the Solar System is comprised by other planets that might affect the relative motion of the NEO-spacecraft system depending on their proximity. For this reason, it is important to quantify the relative effects induced due to third-bodies.

Figure 2.6 shows the different accelerations that affect both spacecraft and NEO motion. Observing the plots, it is possible to see that third body effects are acting on both spacecraft and NEO. Jupiter, the largest planet of the Solar System, produce an acceleration on both spacecraft and NEO of ~ 10^{-7} m/s^2, which is of the same order as the SRP acting on the spacecraft. However, when taking the difference the relative effect decays several orders of magnitude below the SRP. This makes that when considering the relative motion between them, these accelerations can be neglected. Only the relative acceleration induced by the gravity of the Sun is included as follows (Bellei et al., 2009):

$$\mathbf{a}_{Sun} = -\frac{\mu_{Sun}}{d^3_{S/C}}\mathbf{d}_{S/C} + \frac{\mu_{Sun}}{d^3_{\text{NEO}}}\mathbf{d}_{\text{NEO}} \tag{2.22}$$

where $\mathbf{d}_{\text{NEO}}$ and $\mathbf{d}_{S/C}$ are the Sun-NEO and Sun-spacecraft distance respectively. For the spacecraft, it is clear that the main acceleration that affects the relative motion is the one due to SRP followed by the gravitational effect of 2001 QC34. The reason for this is because of the high spacecraft area to mass ratio compared with the NEO one.

YARKOVSKY EFFECT

The Yarkovsky effect is a force acting on rotating bodies caused by the absorption of sunlight that it is re-emitted in terms of heat causing the body to drift (Wie, 1998). This effect is completely negligible for preliminary analysis as its magnitude is much smaller than the other accelerations (~ 10^4 less) (Figure 2.6). However, this effect must be included in rigorous dynamical models when propagating the trajectory of the NEO.

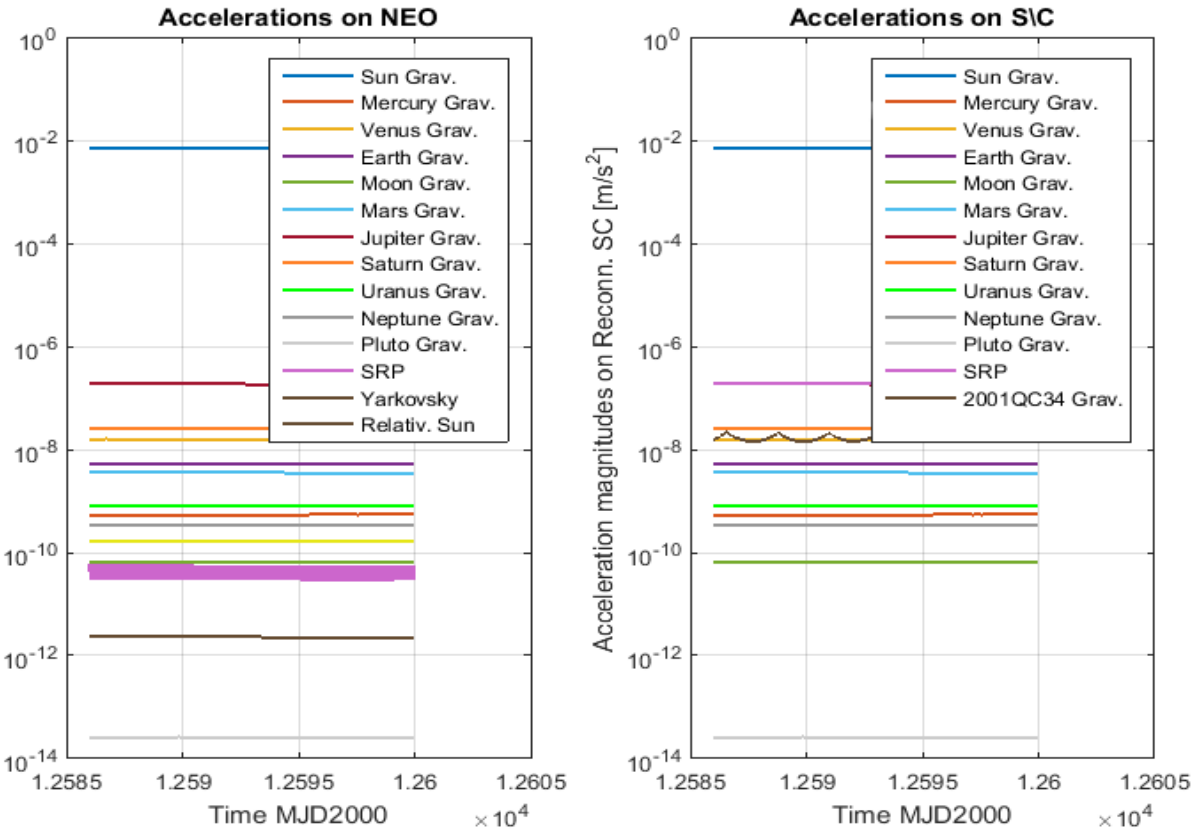

Figure 2.6: Accelerations acting on both S/C and NEO for the S/C located at 5 km distance from the minor body (Delchambre et al., 2017b).

OTHER EFFECTS

There are other effects that affect the NEO dynamics. One also related with the thermal radiation of the body is Yarkovsky–O'Keefe–Radzievskii–Paddack (YORP). YORP is a combined effect of the irregular shape of the asteroid and the absorption of sunlight and its re-emission as thermal radiation which causes the asteroid to spin up or down its rotational velocity. However, this effect is negligible for timescales of a space mission. As an example, for a 5 km radius asteroid the timescale of the variation in the rotational speed is of the order of 10^8 years (Rubincam, 2000).

Another potential perturbation could be electromagnetic forces but this effect would be extremely small. So far, no data is available about the presence of magnetic field around 2001 QC34. In the case of the Earth, this value is of the order of 10^{-10} m/s^2 (Wakker, 2015). This fact makes to automatically discard any possibility of inclusion of this effect.

2.3. EQUATIONS OF MOTION

In this section, the equations of motion for both translational and rotational motion are summarized.

2.3.1. TRANSLATIONAL MOTION

Considering the above mentioned perturbations, the Newtonian formulation representing the spacecraft relative motion with respect to the asteroid expressed in the inertial frame centered in the minor body (Section 2.1) is:

$$ {}^{\text{nci}}\ddot{\mathbf{r}}_{\text{s/c}} = {}^{\text{nci}}\mathbf{a}^{\text{g}}_{\text{s/c}} + {}^{\text{nci}}\mathbf{a}^{\text{SRP}}_{\text{s/c}} + {}^{\text{nci}}\mathbf{a}^{\text{Sun}}_{\text{s/c}} + {}^{\text{nci}}\mathbf{u}_{\text{s/c}} + {}^{\text{nci}}\boldsymbol{\epsilon}^{T}_{\text{s/c}} \tag{2.23} $$

where ${}^{\text{nci}}\mathbf{r}_{\text{s/c}}$ is the spacecraft position $[{}^{\text{nci}}x_{\text{s/c}}\ {}^{\text{nci}}y_{\text{s/c}}\ {}^{\text{nci}}z_{\text{s/c}}]^{\text{T}}$, ${}^{\text{nci}}\mathbf{u}_{\text{s/c}}$ is the thruster command acceleration and ${}^{\text{nci}}\boldsymbol{\epsilon}^{T}_{\text{s/c}}$ accounts for accelerations caused by thrust errors/misalignments.

As mentioned in Section 2.1, studying the motion of the spacecraft relative to both Sun and asteroid is very important for the operational conditions of the mission. The equations relating this motion are given

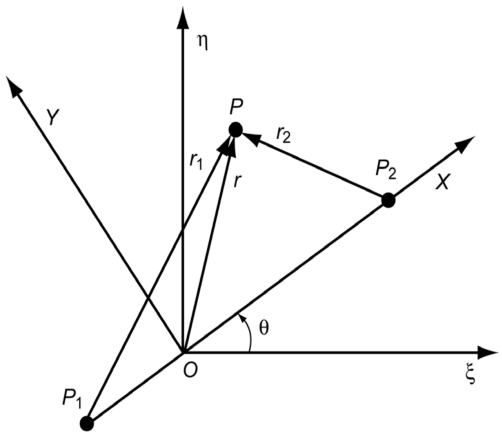

Figure 2.7: Inertial and rotating reference frames in the circular restricted three-body problem (Wakker, 2015).

in the context of the restricted three-body problem (Wakker, 2015), where the mass of two bodies (Sun-NEO) is much larger than the mass of the third (S/C) (and thus, the latter can be neglected) and the two massive objects move in circular orbits about the barycentre of the system. The situation is exemplified in Figure 2.7. Here, an inertial frame $\xi\eta\zeta$ is defined with its origin O at the barycentre of the two massive bodies P_1 (Sun) and P_2 (NEO), and with the ζ-axis perpendicular to the plane containing these bodies. Now, a second reference frame XYZ is defined with its origin also in the barycentre of the system, its X-axis coinciding with P_1P_2, XY-plane coinciding with $\xi\eta$ and Z-axis coinciding with ζ. This second frame rotates with a constant angular velocity $\omega = d\theta/dt$ along the Z-axis. With these two frame definitions, the velocity of the third body P (S/C) can be expressed as follows:

$$\dot{\mathbf{r}}_I = \dot{\mathbf{r}}_R + \boldsymbol{\omega}_R \times \mathbf{r}_R \tag{2.24}$$

where subscripts I and R refer to the inertial ($\xi\eta\zeta$) and rotating frame (XYZ) respectively. Deriving Equation (2.24) with respect to time, the acceleration is obtained like:

$$\ddot{\mathbf{r}}_I = \ddot{\mathbf{r}}_R + 2\boldsymbol{\omega}_R \times \mathbf{r}_R + \boldsymbol{\omega}_R \times (\boldsymbol{\omega}_R \times \mathbf{r}_R) \tag{2.25}$$

and now expressing the motion centered in P_2 (neoS) and relative to the spacecraft, the equations take the form given by (Vallado, 2001):

$${}^{\text{neoS}}\ddot{\mathbf{r}}_{\text{s/c}} = {}^{\text{neoS}}\ddot{\mathbf{r}}_{\text{s/c},I} - 2\boldsymbol{\omega}_R \times {}^{\text{neoS}}\mathbf{r}_{\text{s/c}} - \boldsymbol{\omega}_R \times \left(\boldsymbol{\omega}_R \times {}^{\text{neoS}}\mathbf{r}_{\text{s/c}}\right) \tag{2.26}$$

Equation (2.26) can be simplified considering that the NEO-S/C relative distance is very small compared with the Sun-NEO one and that μ_{NEO} is also very small compared with μ_{Sun}. Then, linearising the expression, the equations known as Clohessy-Wiltshire equations are obtained (Broschart and Scheeres, 2007):

$${}^{\text{neoS}}\ddot{x}_{\text{s/c}} - 2N\,{}^{\text{neoS}}\dot{y}_{\text{s/c}} - 3N^2\,{}^{\text{neoS}}x_{\text{s/c}} = {}^{\text{neoS}}a_x \tag{2.27}$$

$${}^{\text{neoS}}\ddot{y}_{\text{s/c}} + 2N\,{}^{\text{neoS}}\dot{x}_{\text{s/c}} = {}^{\text{neoS}}a_y \tag{2.28}$$

$${}^{\text{neoS}}\ddot{z}_{\text{s/c}} + N^2\,{}^{\text{neoS}}z_{\text{s/c}} = {}^{\text{neoS}}a_z \tag{2.29}$$

where N is the mean motion of the primary bodies ($N = \sqrt{\left(\mu_{\text{NEO}} + \mu_{\text{Sun}}\right)/d_{\text{NEO}}^3}$).

Closed form analytical solutions of the Clohessy-Wiltshire equations can be obtained when the right-hand-side terms are constant or zero. The resultant equations are the ones usually used to represent the relative motion between two satellites around the Earth. However, when applied to the spacecraft-asteroid relative motion, the solution is not valid. Sufficiently far away from the NEO, where the gravitational attraction is negligible, it might work with the inclusion of the constant effect of SRP, but in the vicinity of an asteroid, the dynamics are more complex and further effects need to be included. The theory assumes that both target and chaser have negligible mass and thus no gravitational effects are introduced. However, when

modelling the NEO-spacecraft relative motion, the acceleration exerted by the asteroid does become relevant and even the irregularities of the body need to be modelled for a correct representation. These effects together with SRP comprise the main perturbation of the system (Section 2.2). Another relevant aspect is that the period of motion of the spacecraft around the asteroid is of the same order of magnitude as the period of the asteroid around the Sun (~ 1 year). These long time scales make it impractical to use these techniques for the observation of the asteroid (Scheeres, 2014), where a typical duration of this phase is of the order of months.

The complexity of the motion obligates to study the dynamics in a numerical way, although some information can be extracted from Equations (2.27) to (2.29) and it will be explored in Section 3.1.1.

2.3.2. ROTATIONAL MOTION

Several authors provide the derivation of the equations for rigid body rotational dynamics (Markley and Crassidis, 2014; Wie, 1998). Here, derivations are skipped and the expressions are summarized (Bayard, 2010).

$$\mathbf{J}^{\mathrm{B}}\dot{\boldsymbol{\omega}} = {}^{\mathrm{B}}\boldsymbol{\tau} - {}^{\mathrm{B}}\boldsymbol{\omega} \times \mathbf{J}^{\mathrm{B}}\boldsymbol{\omega} + {}^{\mathrm{B}}\mathbf{d} \tag{2.30}$$

where $\mathbf{J}$ is the inertia matrix, ${}^{\mathrm{B}}\boldsymbol{\omega}$ the spacecraft angular velocity, ${}^{\mathrm{B}}\mathbf{d}$ the external torque acting on the spacecraft and ${}^{\mathrm{B}}\boldsymbol{\tau}$ the commanded torque.

As mentioned in Section 1.2.5, the spacecraft is 3-axis stabilised, controlled with four reaction wheels and to include the effects of the spinning wheels into the inertia of the system, Equation (2.30) needs to be slightly changed. The equations in its momentum rate form (Bayard, 2010) can be expressed as:

$$\mathbf{J}^{\mathrm{B}}\dot{\boldsymbol{\omega}} = {}^{\mathrm{B}}\boldsymbol{\tau} - {}^{\mathrm{B}}\boldsymbol{\omega} \times \left(\mathbf{J}^{\mathrm{B}}\boldsymbol{\omega} + {}^{\mathrm{B}}\mathbf{h}_{\omega}\right) + {}^{\mathrm{B}}\mathbf{d} \tag{2.31}$$

where ${}^{\mathrm{B}}\mathbf{h}_{\omega}$ is the angular momentum vector associated with the n reaction wheels and ${}^{\mathrm{B}}\boldsymbol{\tau} = -{}^{\mathrm{B}}\dot{\boldsymbol{h}}_{\boldsymbol{\omega}}$. The information about the reaction wheels is complemented in Section 4.1.3. When momentum dumping is performed, ${}^{\mathrm{B}}\boldsymbol{\tau}$ expands its formulation by including the torque corresponding to the attitude thrusters ${}^{\mathrm{B}}\boldsymbol{\tau}_{\mathrm{CHT}}$.

Regarding the attitude kinematics, quaternion notation has been used. A quaternion is a four-dimensional vector describing the rotation between two reference frames. A quaternion is formed by (Trawny and Roumeliotis, 2005):

$$\mathbf{q} = \begin{pmatrix} \mathbf{q}_{1:3} \\ q_4 \end{pmatrix} = \begin{pmatrix} q_1 \\ q_2 \\ q_3 \\ q_4 \end{pmatrix} \tag{2.32}$$

where $\mathbf{q}_{1:3}$ denotes the vector part describing the axis of rotation and q_4 a scalar part describing an angle of rotation along the mentioned axis. This four elements of the quaternion are constrained by $q_1^2 + q_2^2 + q_3^2 + q_4^2 = 1$.

To express the time derivative of a quaternion, consider now an infinitesimal increment of time Δt. The rate of change can be then computed as:

$${}^{L(t)}_{G}\dot{\mathbf{q}} = \lim_{\Delta t \to 0} \frac{1}{\Delta t}\left({}^{L(t+\Delta t)}_{G}\mathbf{q} - {}^{L(t)}_{G}\mathbf{q}\right) \tag{2.33}$$

where ${}^{L(t)}_{G}\mathbf{q}$ describes a rotation of the global frame G to the local frame $L(t)$. The quaternion increment ${}^{L(t+\Delta t)}_{G}\mathbf{q}$ can be expressed as a product of two quaternion:

$${}^{L(t+\Delta t)}_{G}\mathbf{q} = {}^{L(t+\Delta t)}_{L(t)}\mathbf{q} \otimes {}^{L(t)}_{G}\mathbf{q} \tag{2.34}$$

$[\mathbf{q}\otimes]$ being the quaternion product defined by:

$$[\mathbf{q}\otimes] = \begin{bmatrix} q_4\boldsymbol{I}_3 - [\mathbf{q}_{1:3}\times] & \mathbf{q}_{1:3} \\ -\mathbf{q}_{1:3}^T & q_4 \end{bmatrix} \tag{2.35}$$

where superscript T denotes the transpose vector. In the limit, when $\Delta t \to 0$, the small rotation ${}^{L(t+\Delta t)}_{L(t)}\mathbf{q}$ can be approximated via Taylor expansion by small angle rotation as:

$${}^{L(t+\Delta t)}_{L(t)}\mathbf{q} \approx \begin{pmatrix} \frac{1}{2}\delta\boldsymbol{\theta} \\ 1 \end{pmatrix} \tag{2.36}$$

where $\boldsymbol{\theta}$ has the direction of the axis of rotation and the magnitude of the angle of the rotation (Trawny and Roumeliotis, 2005). Dividing $\boldsymbol{\theta}$ by the time increment, the rotational velocity can be obtained as follows:

$$\boldsymbol{\omega} = \lim_{\Delta t \to 0} \frac{\delta \boldsymbol{\theta}}{\Delta t} \tag{2.37}$$

With this relationship, finally the rate of change is obtained as (Trawny and Roumeliotis, 2005):

$$\begin{aligned}
{}^{L(t)}_{G}\dot{\mathbf{q}} &= \lim_{\Delta t \to 0} \frac{1}{\Delta t} \left({}^{L(t+\Delta t)}_{G}\mathbf{q} - {}^{L(t)}_{G}\mathbf{q} \right) && (2.38)\\
&= \lim_{\Delta t \to 0} \frac{1}{\Delta t} \left({}^{L(t+\Delta t)}_{L(t)}\mathbf{q} \otimes {}^{L(t)}_{G}\mathbf{q} - \mathbf{q}_0 \otimes {}^{L(t)}_{G}\mathbf{q} \right) && (2.39)\\
&\approx \lim_{\Delta t \to 0} \frac{1}{\Delta t} \left(\begin{pmatrix} \frac{1}{2}\delta\boldsymbol{\theta} \\ 1 \end{pmatrix} - \begin{pmatrix} \mathbf{0} \\ 1 \end{pmatrix} \right) \otimes {}^{L(t)}_{G}\mathbf{q} && (2.40)\\
&= \frac{1}{2} \begin{pmatrix} \boldsymbol{\omega} \\ 0 \end{pmatrix} \otimes {}^{L(t)}_{G}\mathbf{q} && (2.41)
\end{aligned}$$

Finally, the attitude kinematics to express the relation between the BFF with respect to the nci frame, are obtained:

$${}^{\mathrm{B}}_{\mathrm{nci}}\dot{\mathbf{q}} = \frac{1}{2} \begin{pmatrix} {}^{\mathrm{B}}\boldsymbol{\omega} \\ 0 \end{pmatrix} \otimes {}^{\mathrm{B}}_{\mathrm{nci}}\mathbf{q} \tag{2.42}$$

A useful property that will also be used throughout this study is the quaternion conjugation or inverse expressed by:

$$\mathbf{q}^* \triangleq \mathbf{q}^{-1} \triangleq \begin{pmatrix} -\mathbf{q}_{1:3} \\ q_4 \end{pmatrix} \tag{2.43}$$

2.3.3. SUMMARY

Equations (2.23), (2.31) and (2.42) summarize the complete motion of the spacecraft around the NEO and these equations are the ones used for integrating the motion and performing the simulations. Coupling all the expressions, the state vector of the spacecraft can be expressed as follows:

$$\mathbf{x}_{\mathrm{s/c}} = \begin{pmatrix} {}^{\mathrm{nci}}\mathbf{v} \\ {}^{\mathrm{nci}}\mathbf{r} \\ {}^{\mathrm{B}}\dot{\boldsymbol{\omega}} \\ {}^{\mathrm{B}}_{\mathrm{nci}}\mathbf{q} \end{pmatrix} \tag{2.44}$$

3

TRANSLATIONAL GNC

In this chapter, a guidance and control strategy for asteroid observation is developed. It starts by motivating the orbit strategy, evaluating the different alternatives and concluding that near-inertial hovering is the one offering more advantages. Then focuses on the control strategies testing both classical approaches and new strategies. Due to the complexity of the motion the robustness of the translational motion needs to be tested in a numerical way, so a Monte Carlo campaign is carried out for this purpose. Finally, the baseline trajectory used for attitude dynamics is presented.

3.1. GUIDANCE

This section studies the different possibilities for asteroid observation missions (controlled and uncontrolled orbits) and elaborates a trade-off among them. From this information, a guidance law is defined, which will be tested in Section 3.4.

3.1.1. ORBIT DESIGN

Here the different orbit strategies that can potentially be used for observing 2001 QC34 are presented. First, the Sun-NEO-spacecraft system is analysed in an analytic way to have an idea on the system dynamics. Then, controlled (hovering orbits) and uncontrolled motion (Delchambre et al., 2017a) are analysed doing a trade-off between the different options. Hyperbolic arcs are discarded as they are often used for the characterization phase (Takahashi and Scheeres, 2011). This phase is carried out before the observation phase and it serves to determine the physical properties of the NEO and its environment. For this reason, at this stage, the physical properties of the asteroid are assumed to be known.

LAGRANGE LIBRATION POINTS

An important point when considering the potential options available in the vicinity of an asteroid is to obtain the libration points and in particular, L_1 and L_2. A priori, L_1 is an interesting point as it is located on the illuminated side of the Sun-NEO line and if located close enough to the asteroid, it can be used for observation reducing considerably the amount of propellant. On the contrary, L_2 is located on the dark side and no IP navigation is available in these conditions.

Depending on the distance between these points, a set of periodic orbits may exist that can potentially be used for the asteroid observation. However, in this study, this topic remains out the scope but the reader can refer to Scheeres (2016) or Feng et al. (2015) for different possibilities around these points.

The libration points L_1 and L_2 can be computed using the dimensionless expression Equation (3.1). This expression has been obtained from the restricted three-body problem defined in Section 2.3.1. Here, the asteroid is considered as a point mass that describes an elliptical orbit around the Sun. With this assumption, it is possible to replace the time variable t by the true anomaly f, removing thus the dependence with time. The true anomaly is also a more convenient variable to express the distance of the libration point as a function of the position of the NEO along an orbit revolution. SRP effects are included as well as the Sun's third body effects. The derivation can be found in Scheeres (2016).

$$
\begin{aligned}
x'' - 2y' &= \frac{1}{1+e_{\text{NEO}}\cos f}\left[-\frac{x}{r^3}+\beta+3x\right] \\
y'' + 2x' &= \frac{1}{1+e_{\text{NEO}}\cos f}\left[-\frac{y}{r^3}\right] \\
z'' + z &= \frac{1}{1+e_{\text{NEO}}\cos f}\left[-\frac{z}{r^3}\right]
\end{aligned} \tag{3.1}
$$

where β is a constant describing the relative acceleration of the SRP on the spacecraft and given by $\beta = \beta_{\text{NEO}} / \left(\mu_{\text{Sun}} \left(\mu_{\text{NEO}}/\mu_{\text{Sun}}\right)^{1/3}\right)$. Particularizing for $y = z = 0$ and setting x such as $-x/r^3 + \beta + 3x = 0$ the solution is numerically obtained. The solution x^* is then re-scaled with the time varying distance as:

$$
R^* = \frac{a_{\text{NEO}}\left(1-e_{\text{NEO}}^2\right)}{1+e_{\text{NEO}}\cos f}\left(\frac{\mu_{\text{NEO}}}{\mu_{\text{Sun}}}\right)^{1/3} x^* \tag{3.2}
$$

Plotting the solution in Figure 3.1 compared with the one without the inclusion of SRP, it can be observed that L_1 is considerably displaced due to this effect (Figure 3.1a). This is because the SRP pushes a certain body located in the Sun-NEO line in the direction towards the NEO, which is equivalent to assume that no SRP is acting but the NEO has a stronger gravity field. An orbiting distance of 1000 km is impracticable for observing an asteroid of these dimensions with certain accuracy. Thus, this point can be use for station keeping at some stages of the mission, but not for observation. Regarding L_2, apart from being in shadow conditions, the point is so close to the asteroid that the results might be not valid. The SRP may interfere with the surface of the NEO and a S/C located along the Sun-NEO line may not see these effects, resulting then into an intermediate solution between the SRP case and the one without. With these results, it is possible to conclude that these points cannot be used for the observation phase.

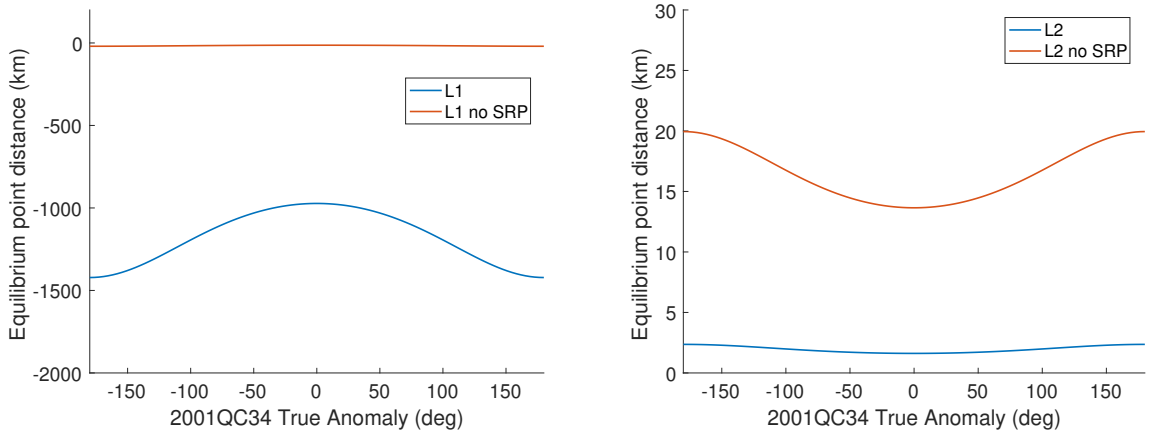

(a) Libration point L_1 with and without the effects of SRP.

(b) Libration point L_2 with and without the effects of SRP.

Figure 3.1: Equilibrium point distances to the NEO as a function of the true anomaly.

STABILITY ANALYSIS

As seen before, the libration points cannot be used for observing 2001 QC34. One of the different orbiting strategies available is to create an artificial libration point by means of thrusting to compensate the total amount of accelerations acting on the spacecraft. This concept is called hovering (Scheeres, 2016). With this technique, the spacecraft is able to stay in a relative fixed position with respect to the body of interest. It is possible to distinguish two different hovering strategies: near-inertial and body-fixed hovering. The former refers to stay in a fixed position relative to the Sun-NEO (typically close to the Sun-NEO line) whereas the latter focuses on the NEO. In this sense, near-inertial hovering allows to observe the asteroid from a global perspective while hovering in the body-fixed frame (Section 2.1) allows to focus on a particular area of interest.

To study the stability in the vicinity of the small-body can bring advantages when designing the orbit controller, apart from providing an overview of the dynamic system. The stability is studied under the dead-band control theory following the derivation presented in Broschart and Scheeres (2007).

Body-Fixed Frame

In this scenario, it is assumed that the spacecraft is close enough to the asteroid that can be considered as a two-body problem. Moreover, the small body rotates uniformly about its maximum moment of inertia and no SRP is included (Broschart and Scheeres, 2007). Note that at a distance of 150 m, the SRP represents less than 1% of the gravity pull. However, the gravity acceleration decreases rapidly and this approximation is no longer valid for distances superior than ~ 500 m (Figure 3.2). The equations of motion of a spacecraft in the body-fixed frame are (Broschart and Scheeres, 2007):

$$\begin{aligned} \ddot{x} - 2\omega\dot{y} &= \omega^2 x + \frac{\partial U}{\partial x} + u_x \\ \ddot{y} + 2\omega\dot{x} &= \omega^2 y + \frac{\partial U}{\partial y} + u_y \\ \ddot{z} &= \frac{\partial U}{\partial z} + u_z \end{aligned} \tag{3.3}$$

where ω is the small-body angular velocity that is assumed to be constant (Table A.1) and $\mathbf{u}$ has an open-loop component ($\mathbf{u}_{OL}$) that continuously thrust to create the equilibrium with respect to the nominal value and a thrust introduced by the dead-band control ($\mathbf{u}_{DB}$) to compensate the deviations from the reference position. The system (Equation (3.3)) can be expressed in a time-invariant way through the Jacobi constant J_{bf}. This is (Broschart and Scheeres, 2007):

$$J_{bf} = \frac{1}{2}|\mathbf{v}|^2 - \frac{1}{2}\omega^2(x^2+y^2) - U(\mathbf{r}) - \mathbf{u}_{OL}^T\mathbf{r} \tag{3.4}$$

and analysing the signs of the eigenvalues of the hessian matrix

$$\left.\frac{\partial^2 J_{bf}}{\partial \mathbf{r}^2}\right|_{(\mathbf{r}=\mathbf{r}_0,\mathbf{v}=\mathbf{0})} \tag{3.5}$$

the number of minimum directions that need to be controlled by the dead-band control are obtained. The results in Figure 3.3 show the different stability regions associated with the sign of the eigenvalues. The number of negative eigenvalues denote the number of directions that need to be controlled for body-fixed hovering. This directions are given by the eigenvectors associated to each of the eigenvalues. It can be seen that for near-equatorial areas $(+--)$ in general two directions need to be controlled and thus optical navigation providing with this information is recommended (Broschart and Scheeres, 2007). However, for landing manoeuvres the final approach is governed by only one direction, in this case the gravity direction $(++-)$, being

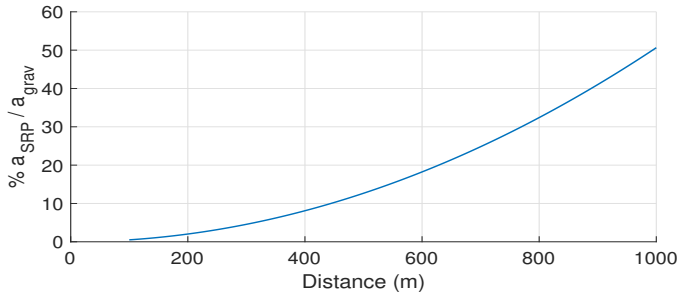

Figure 3.2: Acceleration due to SRP vs gravitational acceleration assuming the NEO as a point mass and expressed as a percentage.

possible to use only altimetry measurements. It is also important to notice the region $(+--)$ coloured in red, as that area may need special control treatment for landing.

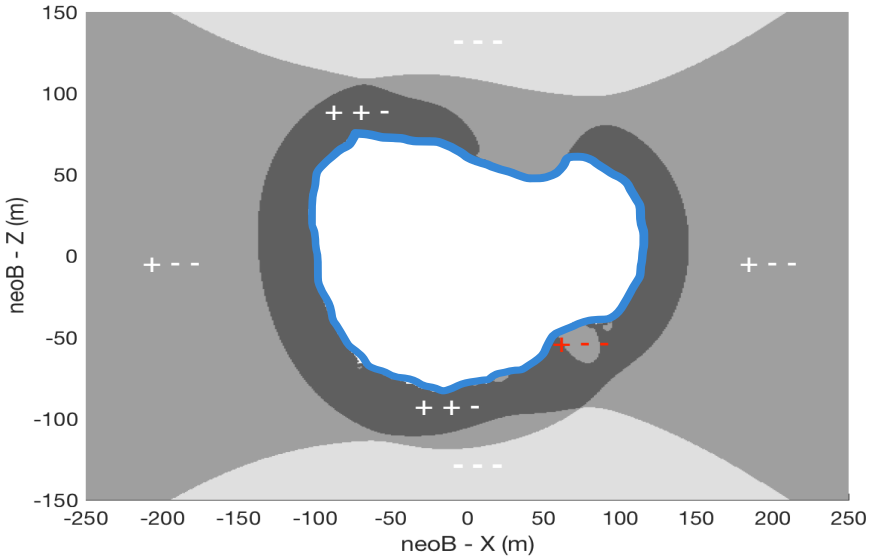

Figure 3.3: Hovering stability regions around asteroid 2001 QC34 in the neoB frame (Section 2.1).

From the point of view of the observer spacecraft, these results do not bring anything valuable to the system design. This is because the spacecraft is not going to do landing manoeuvres, and if performing body-fixed hovering, it is going to stay in a region governed by $(+--)$, needing in any case at least optical navigation information.

Hill Three-Body Problem

The motion described by the Sun-NEO-spacecraft is comprised under the restricted three-body problem (Section 2.3.1). However, in this case, the mass ratio between the NEO and the Sun is incredibly small $\mu_{\text{NEO}}/\left(\mu_{\text{NEO}}+\mu_{\text{Sun}}\right) \sim 10^{-21}$ justifying the approximation to the Hill three-body problem. The equations of motion for a spacecraft performing near-inertial hovering in this system are (Broschart and Scheeres, 2007):

$$\begin{aligned} \ddot{x}-2N\dot{y} &= 3N^2x-\mu_{\text{NEO}}\frac{x}{r^3}+\frac{\beta_{\text{S/C}}}{d_{\text{NEO}}^2}+u_x \\ \ddot{y}+2N\dot{x} &= -\mu_{\text{NEO}}\frac{y}{r^3}+u_y \\ \ddot{z} &= -N^2z-\mu_{\text{NEO}}\frac{z}{r^3}+u_z \end{aligned} \tag{3.6}$$

where N is the mean motion of the primary bodies given by $\sqrt{\left(\mu_{\text{NEO}}+\mu_{\text{Sun}}\right)/d_{\text{NEO}}^3}$. Note that in this formulation, SRP is included as a constant radial effect (x-direction), because the spacecraft-asteroid distance is assumed to be small compared with the Sun-asteroid one. The Jacobi constant is given by:

$$J_{\text{Hill}}=\frac{1}{2}\left|\mathbf{v}\right|^2-\frac{3}{2}N^2x^2+\frac{1}{2}N^2z^2-\frac{\mu_{\text{NEO}}}{r}+\frac{\beta_{S/C}x}{d_{\text{NEO}}^2}-\mathbf{u}_{OL}^T\mathbf{r} \tag{3.7}$$

The eigenvalues are computed in the same way as Equation (3.5). Note that the SRP has no effect in the sign of the eigenvalues as it becomes linear in the Jacobi constant. Physically, this means that dead-band surfaces will constraint the same degrees of freedom independently if SRP is considered or not. However, this acceleration does have an effect when obtaining the zero-velocity surfaces (Figure 3.5).

Analysing Figure 3.4 it can be concluded that hovering in the Hill frame is mainly dominated by $(++-)$ regions. When hovering close to the Sun-NEO line, the associated eigenvector to the negative eigenvalue is closely aligned with the gravity acceleration of the NEO. This fact goes in line with the zero-velocity surface (Figure 3.5). If no control is exerted on the spacecraft, this will evolve to areas with less energy (i.e, this is towards the asteroid causing a potential impact).

From the point of view of the control design, the surfaces that will have to be constrained to keep the spacecraft in a fix position will be in line with the a priori thoughts that someone can have. First, the distance to the spacecraft will have to be controlled. This is because the spacecraft cannot use the electric propulsion system (located in the opposite site of the optical cameras (Figure 1.1)) to continuously counteract the accelerations. Then, the in-plane motion will also have to be constrained to keep the spacecraft close to the Sun-NEO line and the out-of-plane motion will suffer from the same problem when perturbations in this direction are included. Finally, no upper boundary is required for the distance, this is because the SRP is exerting a constant acceleration in the positive radial direction (i.e, as a solar sail) bringing back the spacecraft close to the asteroid. However, for safety reasons this boundary will also have to be constrained so no thrusting errors bring the spacecraft too far away from the asteroid that the opNav is not able to work properly. Summarizing, for a real space mission, three-dimensional control of the spacecraft is desirable for safety reasons.

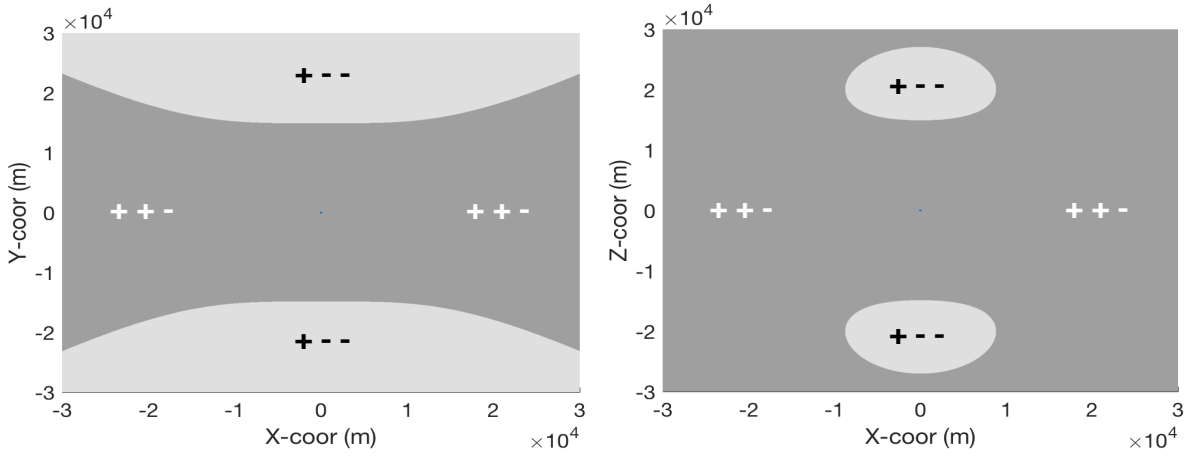

(a) Stability regions X-Y plane

(b) Stability regions X-Z plane

Figure 3.4: Hovering stability regions in the Hill frame around 2001 QC34.

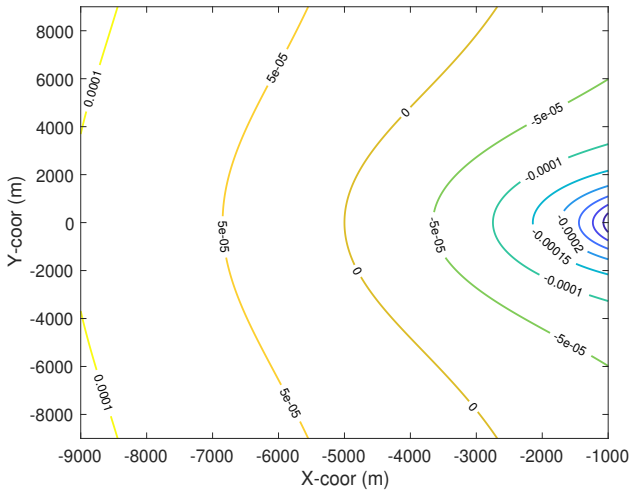

Figure 3.5: Zero-velocity surfaces in the Hill frame including the effects of SRP. Reference position located at 5 km distance from 2001 QC34.

MOTION IN A SOLAR DOMINATED REGIME

The motion in the vicinity of 2001 QC34 is mainly affected by the gravity of the small body and the SRP. As a example, at a distance of 5 km from the asteroid, the acceleration due to SRP is one order of magnitude bigger ($\sim 10^{-7}$ m/s^2) than the gravitational one ($\sim 10^{-8}$ m/s^2). This presents an environment where the motion of the spacecraft is dominated by this effect and thus, needs to be carefully considered. In this section, it is assumed that the small-body is modelled as a point mass.

Dankowicz (1994) first, and Scheeres and Marzari (2002) afterwards using a different approach, obtained an expression for the semi-major axis (a) that limits the stability of the orbit. The formula derived by the former provides a value for a that if exceeded, escape will generally occur. This value is given by:

$$a_{\text{Max}} = \frac{\sqrt{3}}{4}\sqrt{\frac{\mu_{\text{NEO}}}{\beta_{\text{S/C}}}}d_{\text{NEO}} \tag{3.8}$$

However, Scheeres and Marzari (2002) provide a more limiting formulation given by:

$$a_{\text{Min}} = \frac{1}{4}\sqrt{\frac{\mu_{\text{NEO}}}{\beta_{\text{S/C}}}}d_{\text{NEO}} \tag{3.9}$$

which ensures that below this value ($a < a_{\text{Min}}$) escape is prohibited. Note that one differs from the other by a factor of $\sqrt{3}$ and both are scaled with the Sun-NEO distance meaning that escape is more likely to occur in the perihelion (Scheeres, 2016). These values are for the baseline asteroid 2001 QC34: $a_{\text{Max}} \approx 690$ m and $a_{\text{Min}} \approx 395$ m at the perihelium (~ 0.9 au).

Furthermore, using averaged equations and making use of Milankovitch orbit elements (i.e, angular momentum and Laplace vectors), Richter and Keller (1995) developed an expression relating the angular momentum and eccentricity to SRP, obtaining a family of frozen orbits. However, Richter and Keller (1995) considered the motion of the asteroid around the Sun to be circular. Scheeres (2012) generalized the approach, expanding the theory to the elliptical motion around the Sun. From the expressions relating angular momentum and eccentricity to SRP, two special solutions are of interest: one corresponding to a circular orbit whose angular momentum is parallel to the rotation axis of the NEO around the Sun (i.e, contained in the NEO orbital plane) and one corresponding to a circular orbit whose angular momentum is perpendicular to the rotation axis of the NEO around the Sun (i.e, polar/terminator orbit). These two expressions can be found in Scheeres (2016). For the first case, the solution reduces to:

$$e(\psi) = 2\sin\Lambda\left|\sin\frac{\psi}{2}\right|\sqrt{1-\sin^2\Lambda\sin^2\frac{\psi}{2}} \tag{3.10}$$

and for the second case:

$$e(\psi) = \frac{1}{2}\sin(2\Lambda)\left(1-\cos\psi\right) \tag{3.11}$$

where ψ is the scaled true anomaly ($\psi = f/\cos\Lambda$) of the NEO with respect to the Sun and Λ is given by the expression:

$$\tan\Lambda = \frac{3\beta_{\text{S/C}}}{2}\sqrt{\frac{a_{\text{S/C}}}{\mu_{\text{NEO}}\mu_{\text{Sun}}a_{\text{NEO}}\left(1-e_{\text{NEO}}^2\right)}} \tag{3.12}$$

Particularizing this equation for our asteroid, a value for Λ of 88.2387° is obtained. The results for Equations (3.10) and (3.11) are shown in Figure 3.6.

In Figure 3.6, it is seen that variations in the SRP induce variations of the eccentricity, reaching a value of 1 in two occasions along one orbital revolution. However, it does not mean that the orbit is going to escape but it is likely to do it. For this reason, heliotropic orbits (Lantukh et al., 2015) are not recommended in this environment. On the contrary, in the polar orbit case (Figure 3.6), the effects of SRP tend to circularize the orbit as the perturbation increases (i.e., approximates to the perihelion), this being the reason why these orbits are preferred.

If an appropriate choice of the orbital elements is done ($e = \cos\Lambda$), a photo-gravitationally stable orbit (PGSO) or terminator plane frozen orbit can be defined (Figures 3.7 and 3.8). The line of nodes of this orbit

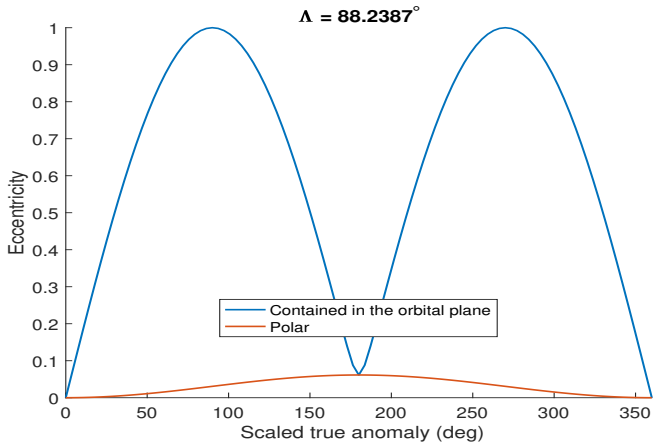

Figure 3.6: Eccentricity as a function of the scaled true anomaly for a circular orbit of semi-major axis 500 m.

rotates at the same rate as the asteroid around the Sun and the angular momentum vector is parallel to the Sun-NEO line. If this vector points towards the Sun, then the argument of periapsis ω must be chosen equal to $\pi/2$ and in contrast, $-\pi/2$ if pointing away from the Sun (Scheeres, 1999). In Figure 3.7 an orbit of these characteristics can be observed. The orbit has been propagated in the Hill Frame (i.e, neoS), which rotates with the same rate as the NEO does around the Sun. It is possible to see that the orbit remains stable, fact that can be better observed analysing their orbital elements (Figure 3.8). The values remain bounded during the integration time. In the case of the RAAN, the fact of being bounded close to the initial value ($-90°$) is a confirmation of the stated before, that spacecraft orbit rotates as the same rate as the NEO does around the Sun.

The reasons why terminator plane frozen orbits are discarded obey to physical limitations and safety reasons. The explanation can be found in Figure 3.9. Here, the FoV range is plotted as a function of the distance to the asteroid. The blue area limits the distance where escape is prohibited, the light green the stable distance bounded by the two approaches (a_{Max} and a_{Min}) and in yellow the region where escape will generally occur. The NAC and WAC FoV is also represented. Paying attention to the WAC, it is possible to see that up to $\sim$ 650 m distance from the asteroid the camera is not able to observe completely the body, which decreases the performance of the navigation system. Moreover, the margin is too narrow from the limit imposed in Equation (3.8) for ensuring stability.

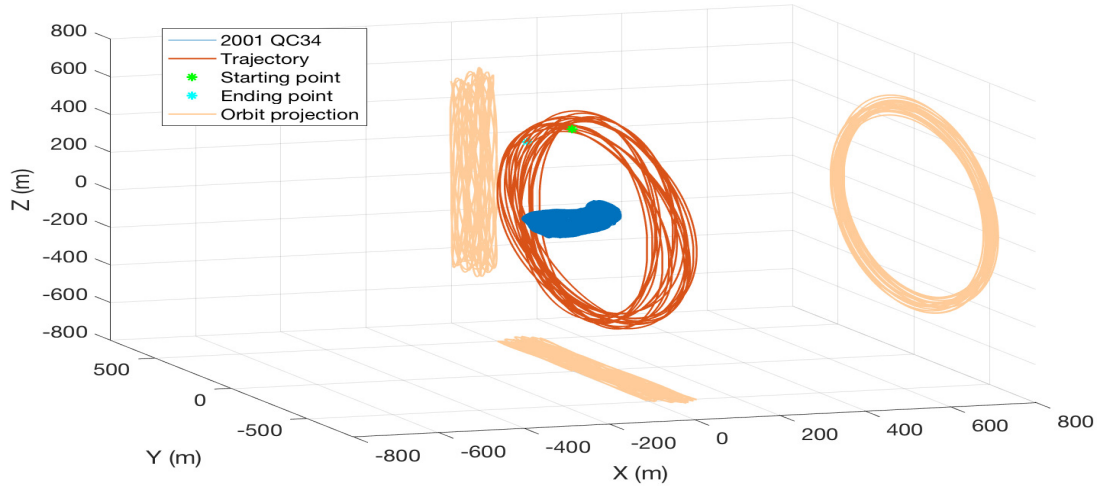

Figure 3.7: 28-days PGSO propagated in the Hill Frame (Section 2.1) using MATLAB ODE45 (default settings). Initial conditions: $[0, 0, 484.65]$ m and $[0, 0.0289, 0]$ m/s at a distance of 0.9 au where the solar activity is maximum.

For an autonomous navigation system, orbiting at a distance of ~ 500 m from the surface of the body elevates the risk of collision in case of any failure. However, increasing this distance is not an option as the orbit may become unstable. To exemplify this, the simulation is repeated with a polar orbit with a semi-major axis of 800 m. As it can be seen in Figure 3.10 the orbit becomes unstable. In fact, the difference in

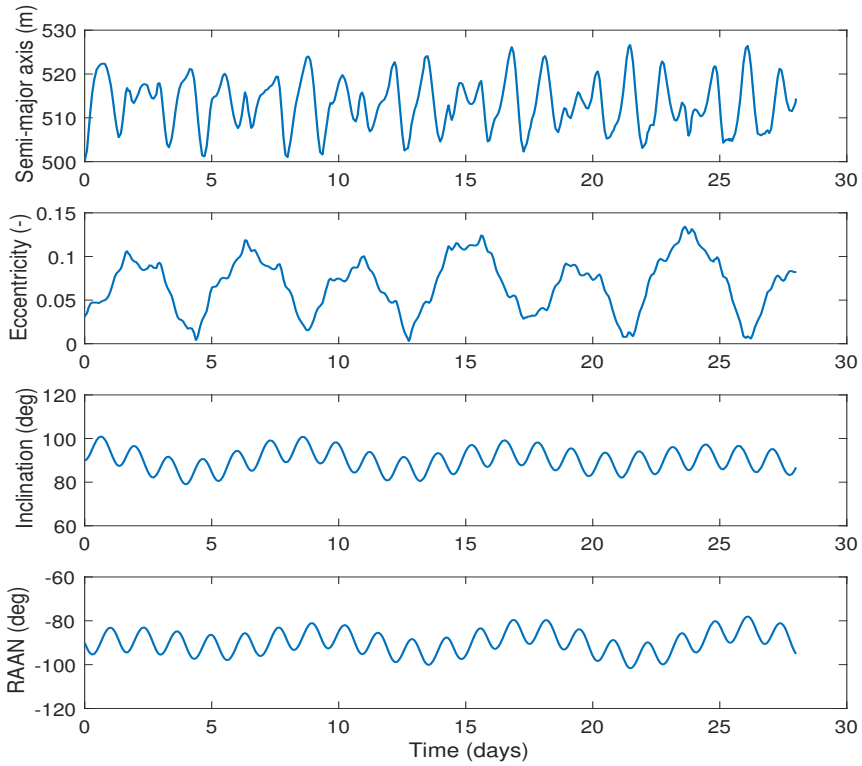

Figure 3.8: Evolution of the PGSO orbital elements propagated in the Hill Frame (Section 2.1).

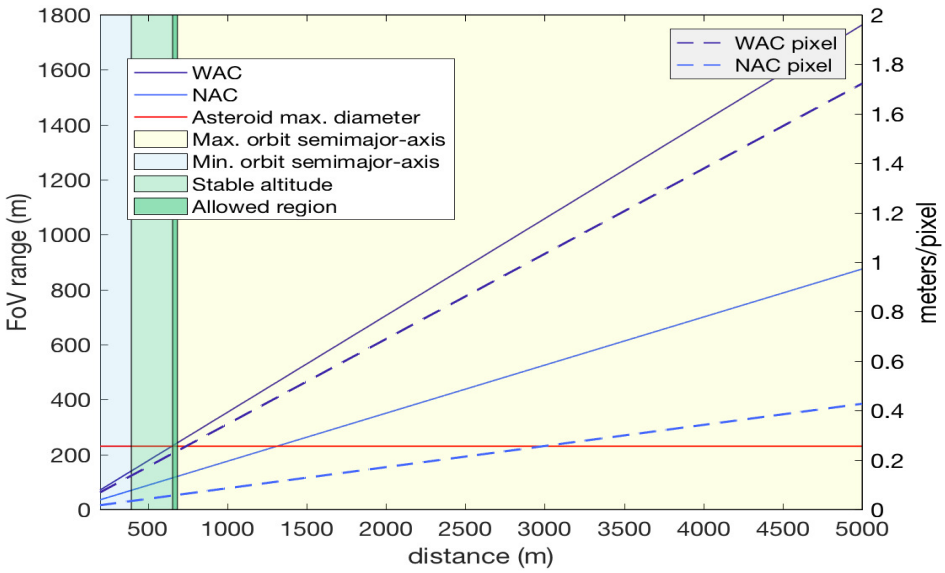

Figure 3.9: Field of View (FoV) range vs asteroid distance vs pixel resolution for NAC and WAC.

orbital velocity with the a = 500 m case is of the order of millimetres per second. Having in mind that the accuracy of the estimated velocity by the navigation system (Section 3.2) is of the same order, an orbit of these characteristics results impracticable with the current performance values.

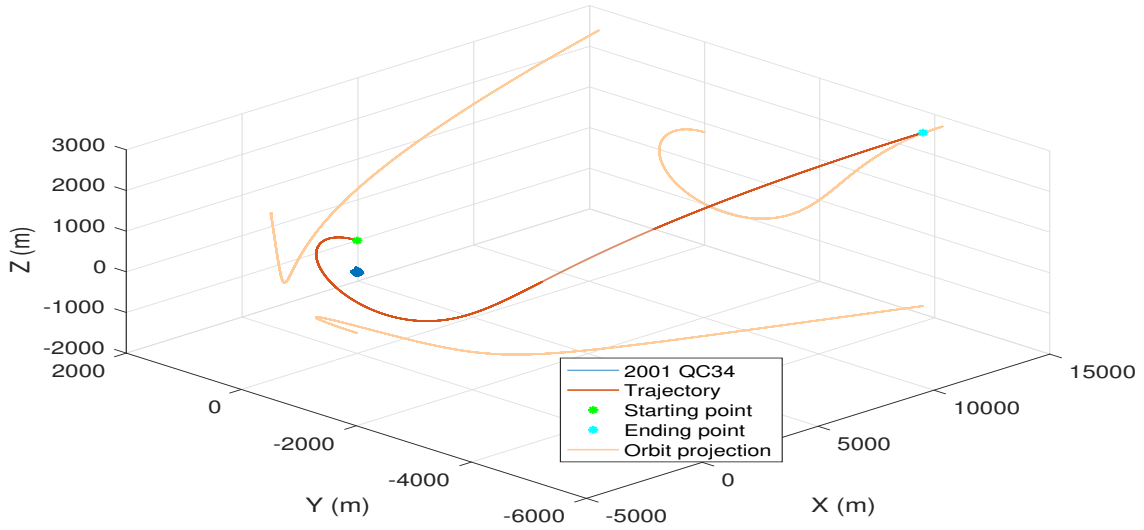

Figure 3.10: Unstable polar orbit propagated in the Hill Frame (Section 2.1) using MATLAB ODE45 (default settings). Initial conditions: [0,0,775.44] m and [0,0.0228,0] m/s at a distance of 0.9 au where the solar activity is maximum.

TRADE-OFF

Summarizing, in this section the potential options available for orbiting a NEO have been evaluated for 2001 QC34. First, it has been shown that the libration points cannot be used during the observation phase. L_1 is located to far away from the NEO while L_2 is located in the dark side, making impossible the use of opNav. Second, the stability around the practically forces to specify a three-dimensional control in every location in the close-vicinity of the NEO no matter the strategy followed, near-inertial or body fixed hovering. From the system design, no advantages can be drawn from these results. Finally, regarding uncontrolled orbits, heliotropic are not recommended as they are likely to escape, apart from the fact that a certain percentage of the orbit is in shadow conditions. In the case of terminator orbits, however, the situation is different. It is possible to orbit in a stable conditions but the required distance to the body is too small for the system specifications (FoV of the onboard cameras) and the margins in terms of ΔV from a stable orbit to an unstable one are too narrow. Note that inclined orbits have not been considered for being an intermediate solution between heliotropic and terminator orbits.

Based on these results, a trade-off considering type of orbit, stability, visibility of the asteroid, ΔV and safety reasons is presented in Section 3.1.1. Specially in terms of safety, hovering manoeuvres are preferred for asteroids with dimensions similar to 2001 QC34. Body-fixed hovering is only particularly attractive when landing manoeuvres are desired. Otherwise, near-inertial hovering outperforms for observation strategies. Heliotropic and terminator plane frozen orbits are discarded for not being safe for autonomous GNC systems based on IP.

Orbit	Stability	Visibility	ΔV	Safety	Other remarks
Heliotropic	Good for "large" asteroids (Eros ~17km diameter). Unstable for small (~1km diameter).	Certain % of shadow	-	No navigation in the shadow part. Too close to the asteroid in the periapsis	Potential resonance issues
Terminator plane frozen orbit	Unstable above ~ 800 m. Needs to be controlled.	Due to NEO shape 80-100% of the surface in the short term and 100% in long term	Depends on control system. SRP compensated.	Too close from the asteroid. WAC covers full body @ 650 m. Narrow velocity margins. Unfeasible control system for current specs (Appendix B).	-
Inertial hovering	Needs to be controlled to counteract all the forces.	Depends on the position. Along Sun-NEO line 80-100% of the surface in the short term and 100% in long term.	0.01 m/s/day @ 5km	If SRP not controlled either collision or shadow conditions	-
Body-fixed hovering	Needs to be controlled to counteract all the forces. Additional term: centrifugal forces	Specific area observation (50%)	0.1 m/s/day @ 500m + rotational forces	if SRP not controlled either collision or shadow conditions	Limited operational time (half NEO day). Needs to be combined with other methods

Table 3.1: Trade-off between the different orbit configurations potentially available for asteroid observation.

3.1.2. DEFINITION OF THE CONTROL BOX

From Section 3.1.1, it is derived that the best strategy for observing a NEO of these dimensions is the concept of near-inertial hovering. To implement this method, the guidance strategy used is based in the concept of control box. This strategy seeks to keep the spacecraft within certain boundaries with respect to a certain reference point. In this case, the reference point used for this study is located at 5 km distance from the asteroid in the visible side of the Sun-NEO line ($\mathbf{r}_{\text{ref}} = [-5000, 0, 0]^T$ m in the NEO rotating frame (Section 2.1)). This point has been selected based on several factors. First it allows to observe the asteroid with safe margins, as in case of failure the ground station has at least 1 day before crash. Second, the asteroid occupies 1/3 of the NAC FoV which provides margin for control. Finally, the irregularities of the NEO are negligible when designing the controllers (as seen in Figure 2.5), a fact that also has an advantage in the orbit determination algorithms (Harbulot, 2017).

The guidance strategy does not seek to locate the spacecraft in a certain relative position with respect to the asteroid because it would require to continuously counteract the relative acceleration. Electric propulsion is only available for the transfer orbit and the orbit maintenance has to be done using discrete controllers. Thus, the objective is to constraint the motion into a certain region while the amount of manoeuvres and propellant consumption is minimized. This also provides to the navigation system with long periods without any thrust which improves the accuracy of the estimated state.

In principle, having an idea of the minimum directions that need to be controlled provides with a better overview of the dynamics around the body (Section 3.1.1). However, for a real mission the three dimensions need to be controlled. Depending on how this is done, the performance of the GNC will vary. For that reason, diverse shapes and dimensions for the control box has been tested whose definitions are collected here. Although the integration of the dynamics is done in the inertial frame, for convenience the boundary limits are defined relative to the Sun-NEO system (neoS frame). This is due to the available sensors such as Sun sensors or the opNav that measures the relative state between the mentioned bodies.

BOUNDARY S1

The first boundary surface is short of a truncated cone delimited by three boundaries: lower, upper and lateral. Here, the lower boundary is referred to the lowest distance to the asteroid whereas upper refers to the largest one. The lateral boundary is a cone that constraints the motion given a specified angle with respect to the asteroid. Figure 3.11 shows a schematic view of the boundary control surface and mathematically, the limits can be described as:

- Lower boundary: $\sqrt{x^2 + y^2 + z^2} < d_{\text{ref}}(1 - S)$
- Upper boundary: $\sqrt{x^2 + y^2 + z^2} > d_{\text{ref}}(1 + S)$

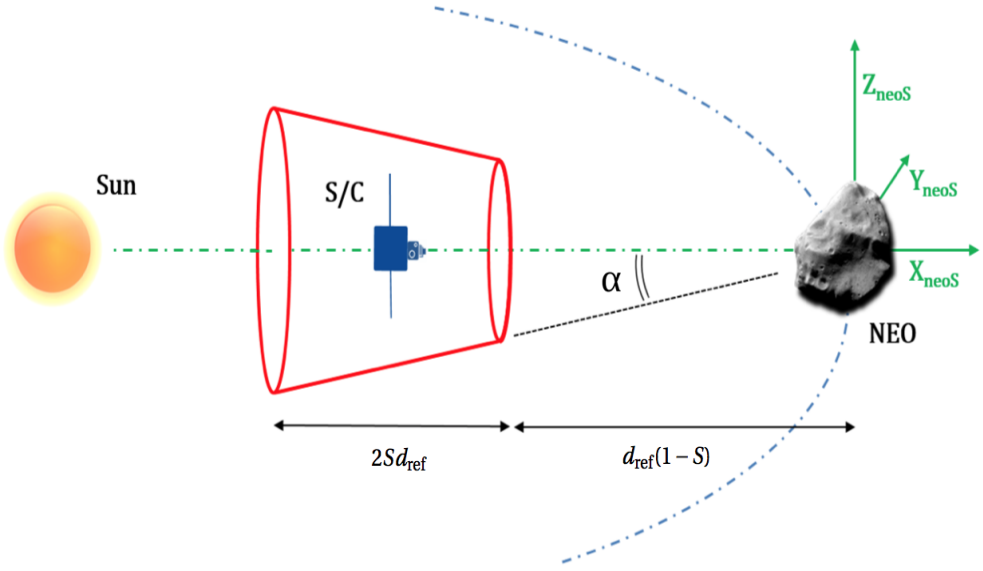

Figure 3.11: Schematic view of Boundary S1 (Harbulot, 2017).

- Lateral boundary: $\sqrt{y^2+z^2} > \sqrt{x^2}\tan\frac{\alpha}{2}$

where $[x,y,z] \triangleq [^{neoS}x_{S/C}, ^{neoS}y_{S/C}, ^{neoS}z_{S/C}]$ denote the relative position of the spacecraft with respect to the asteroid, $d_{ref} = 5000$ m and S the size of the control box as a percentage of the reference distance. Two sizes have been studied: small ($S = 0.1$) and large ($S = 0.15$). The cone opening angle α is obtained as:

$$\alpha = 2\arctan\frac{d_{ref}S/2}{d_{ref}(1+S)} \tag{3.13}$$

According to the performance requirements defined in Section 1.3, the size of the control box for NS-GNC-01 is defined as the minimum distance between the lower and upper boundary of the control box. This is for example for the case of $S = 0.1$, size $= 2Sd_{ref} = 2 \cdot 0.1 \cdot 5000 = 1000$ m.

BOUNDARY S2

For the second boundary, a sphere centered in the reference point r_{ref} with radius $r \in [500, 750]$ m has been defined. The values for the radius are also defined based on the parameter S. In this case, $S = 0.1 \rightarrow r = 500$ m and $S = 0.15 \rightarrow r = 750$ m. The boundaries are also denoted as small and large accordingly. Figure 3.12 shows a schematic view of the control box and mathematically, these boundaries can be described as Equation (3.14). According to the performance requirements defined in Section 1.3, the size of the control box for NS-GNC-01 is defined in this case as the diameter of the control box.

$$\sqrt{(x-x_{ref})^2+(y-y_{ref})^2+(z-z_{ref})^2} > d_{ref}\cdot S \tag{3.14}$$

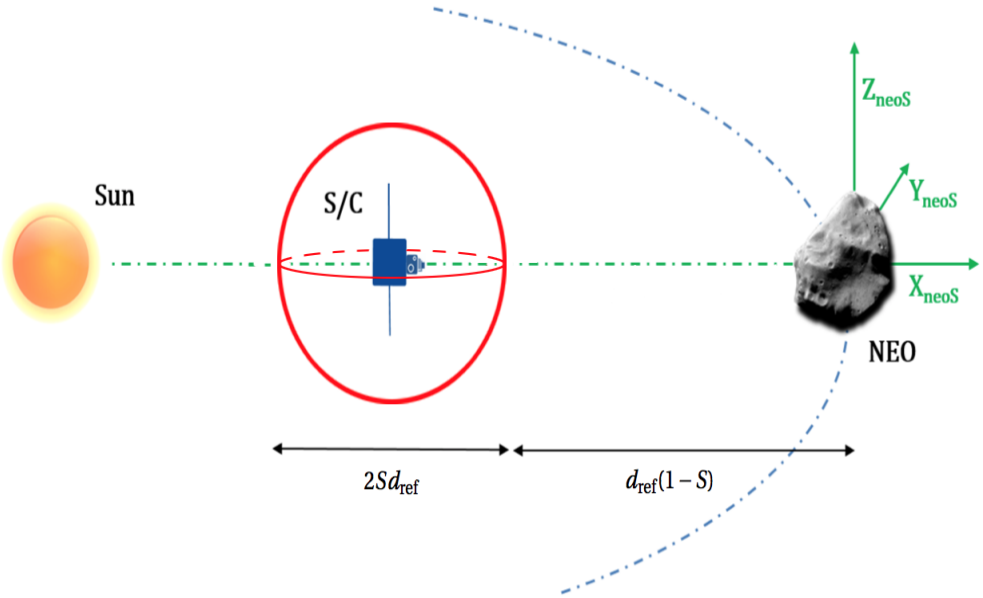

Figure 3.12: Schematic view of Boundary S2.

3.2. NAVIGATION

As mentioned in the introduction, the navigation was originally developed in the work developed by Delchambre et al. (2017b); Harbulot (2017) and Maurice and Delchambre (2016). Here an overview of the characteristics is given but for further information please refer to Delchambre et al. (2017b).

The navigation is based on IP from the images taken by one of the opNav cameras (NAC or WAC). The IP algorithm is based on landmark detection. First, during the characterization phase, images from the NEO are taken and stored for different illumination conditions. Then, different algorithms are used for feature detection (Maximally Stable Extremal Regions (MSER)), description (Speed-Up Robust Features (SURF)) and matching.

To compute the pose estimation, an Extended Kalman Filter (EKF) is implemented as algorithms such as direct least-squares (DLS) and pose from orthography and scaling with iterations (POSIT) are not accurate

enough to satisfy the mission requirements (Ziegler and Delchambre, 2016). The estimated relative state of the spacecraft (position + velocity) and the NEO attitude and angular velocity are obtained in the NEO inertial frame (nci) and ICRF respectively. For this estimation, the attitude of the spacecraft is assumed to be perfectly known from an on-board star-tracker. However, this assumption will be relaxed in Chapter 4. Besides the state

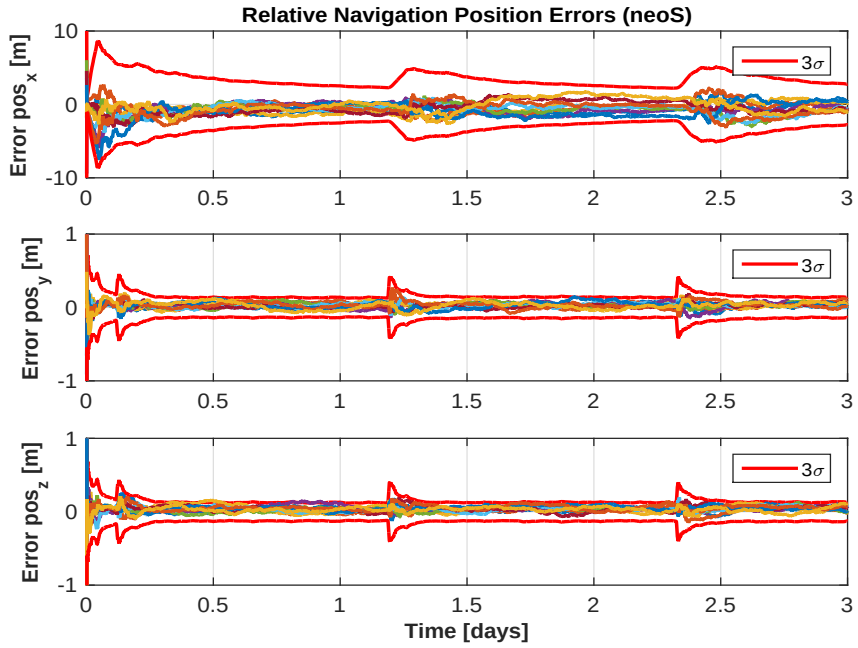

Figure 3.13: Relative navigation position errors expressed in the NEO rotating frame with an accuracy of (3σ). The different curves show the results for each of the Monte Carlo runs (Delchambre et al. (2017b)).

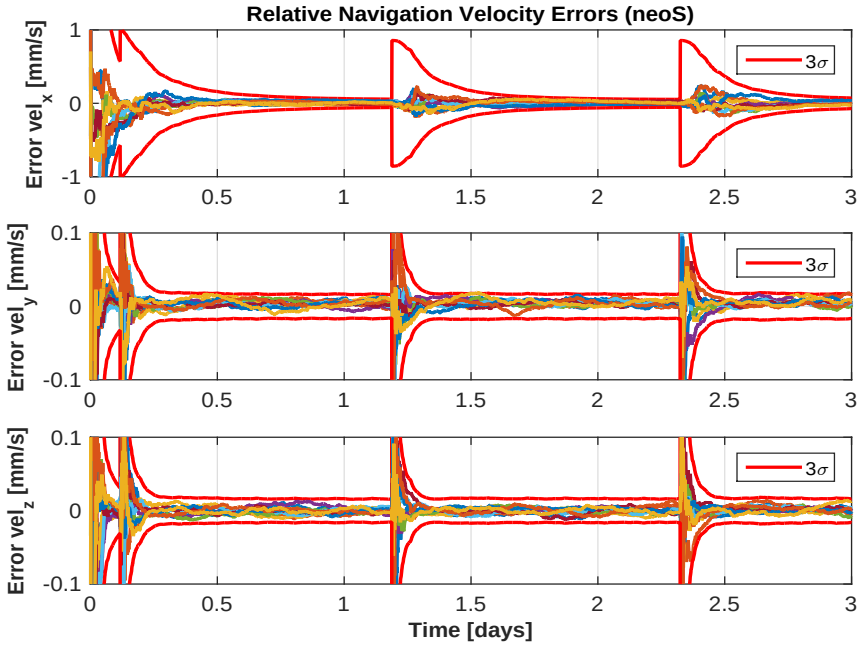

Figure 3.14: Relative navigation velocity errors expressed in the NEO rotating frame with an accuracy of (3σ). The different curves show the results for each of the Monte Carlo runs (Delchambre et al. (2017b)).

of both spacecraft and asteroid, the EKF also integrates the SRP estimation. This acceleration is modelled as described in Lenoir et al. (2011), where a concept of electrostatic accelerometer (MicroSTAR) is proposed to measure non-gravitational accelerations on-board a spacecraft suitable for exploration missions. With these results, SRP can be measured with an accuracy of 10^{-8} m/s^2 (1σ) and an estimation performance of $3 \cdot 10^{-9}$ m/s^2 (1σ). This result implies that the SRP is known which approximately 10% of error (remember that the nominal value is of the order of 10^{-7} m/s^2 (Section 2.2.2).

The navigation system is included in the E2ESS that will be used for the control performance studies around 2001 QC34. Here, the performance results of a Monte Carlo campaign for the navigation filter are shown (Figures 3.13 and 3.14). These results have been used for preliminary analysis, in which the errors due to position and velocity uncertainties have been included. Furthermore, the results contribute to exemplify the importance of reducing the number of manoeuvres as much as possible. At times equal to ~ 1.25 and ~ 2.25 days, it can be seen that the uncertainty of the navigation filter increases, this is precisely due to thrusting commands. In periods in which no manoeuvres are commanded, the performance of the filter is ~ 10 times superior.

3.3. CONTROL

As seen in Section 3.2, the main objective of the control system is to minimize the amount of thrusting manoeuvres to decrease the thrust errors and benefit the state estimation. As long as the position is within the control box fulfilling the performance requirements (Section 1.3), it is enough. Moreover, this must be achieved in a fully autonomous way (i.e. free from ground control).

Hayabusa mission was the first and the only one to implement near-inertial hovering for observing an asteroid (Itokawa) (Kominato et al., 2006). In this case dead-band control theory was implemented as mentioned in Broschart and Scheeres (2007). In Vetrisano and Cano, the authors test other potential control strategies for near-inertial hovering using asteroid Didymos as a baseline. In this publication, a continuous Lyapunov based control and a discrete linear quadratic regulator (LQR) are evaluated together with the mentioned dead-band control. However, the actuation frequency for the first two control strategies is of the order of minutes as opposed to the dead-band control that is of the order of hours. This fact is not compatible with the requirement NS-GNC-02, and thus, these approaches are discarded. In this context, two controllers are tested: one based on dead-band control using different strategies and a Lyapunov based control function that only works in a continuous way once the spacecraft is outside the specified boundaries.

3.3.1. DEAD-BAND CONTROL

In Section 4.5, dead-band control theory has been introduced doing a differentiation between the open-loop and the closed-loop components. As the spacecraft configuration does not allow to thrust continuously, the open-loop one is set to zero and consequently, all the accelerations need to be compensated by the closed-loop component. The dead-band control works under the principle that if a certain criterion defined by a function $f_{db}(\mathbf{r})$ is violated, and impulsive manoeuvre is performed to return to the allowed boundaries. In this case the dead-band function has been defined accordingly to the control boxes defined in Section 3.1.2 and the thrusting function is described as:

$$\mathbf{u}_{db} = \begin{cases} -u\,\hat{\mathbf{c}}(\mathbf{r}), & \text{if } f_{db}(\mathbf{r}) \geq \gamma \\ 0 & \text{otherwise} \end{cases} \tag{3.15}$$

where $\hat{\mathbf{c}}$ represents the unitary vector along the thrust is performed and γ a certain limit established. Four strategies have been studied, two classical strategies: reflection and inversion (Vetrisano and Cano); and two new ones. All these methods manipulate the incoming velocity in a certain way to obtain a resultant velocity that keeps the spacecraft within the limits. Typically, this manipulation is done in a directional way (i.e, changing the direction) but maintaining the incoming speed. To change also the modulus of the velocity, a concept called hysteresis can be applied. Hysteresis is equivalent to apply a ΔV command so that the resultant speed becomes some fraction of the incoming one. However, for autonomous control this is not recommended due to the fact that if always the incoming speed is multiplied by a factor, let's say 0.9, the spacecraft will be loosing energy at each command and will eventually end up on the dead-band boundary producing a continuous thrust (not feasible). A possible solution is to also develop a control strategy for the hysteresis value. This idea will be put in practice in one of the methods (Section 3.3.1). Finally, to denote the velocity before hitting the boundary wall and after, subscripts $-$ and $+$ have been used respectively.

REFLECTION

In this strategy, $\hat{\mathbf{c}}$ is the unitary vector perpendicular to the dead-band boundary f_{db}. This means that when the spacecraft hits a boundary limit, a ΔV manoeuvre is performed along $\hat{\mathbf{c}}$, reflecting the incoming velocity. Particularizing for the sphere case, a manoeuvre would be performed along the radial direction to obtain a reflected velocity with respect to the tangential direction. Mathematically, this is expressed as:

$$\mathbf{v}_+ = \mathbf{v}_- - 2(\mathbf{v}_-^T\hat{\mathbf{c}})\hat{\mathbf{c}} \tag{3.16}$$

INVERSION

In this strategy, $\hat{\mathbf{c}}$ is the unitary vector with opposite direction to the incoming velocity vector. This means that when the spacecraft hits the boundary wall the incoming velocity is literally inverted. Mathematically, this is:

$$\mathbf{v}_+ = -\mathbf{v}_- \tag{3.17}$$

CENTRAL REFLECTION

In this strategy, $\hat{\mathbf{c}}$ is the unitary vector that directs $\mathbf{v}_+$ towards the reference position $\mathbf{r}_{\text{ref}} = [-5000, 0, 0]^T$. For example, for the case of a sphere, the resultant velocity $\mathbf{v}_+$ will be always directed towards the center. For geometrical reasons (it is more natural), only the boundary S2 has been tested with this method.

$$\hat{\mathbf{c}} = \frac{-\hat{\mathbf{v}}_- + \hat{\mathbf{r}}_{\text{rel}}}{|\,-\hat{\mathbf{v}}_- + \hat{\mathbf{r}}_{\text{rel}}\,|} \tag{3.18}$$

$\mathbf{v}_+$ adopts the same format as Equation (3.16) and

$$\hat{\mathbf{r}}_{\text{rel}} = \frac{\mathbf{r}_{\text{ref}} - \mathbf{r}}{|\,\mathbf{r}_{\text{ref}} - \mathbf{r}\,|} \tag{3.19}$$

HYSTERESIS CONTROL

An alternative to reflect always the velocity to a certain direction is to use the lateral accelerations that appear from the centrifugal terms to our benefit (Equation (3.6)). Considering the neoS frame and a boundary limit that only constraints the distance to the NEO (e.g, lower boundary). If the spacecraft starts with zero relative velocity at a radial distance (negative x-axis) of 5 km, the spacecraft will experience a positive acceleration in the radial direction due to SRP (i.e, working as a solar sail) and gravity attraction of the NEO. Furthermore, the resultant positive velocity will provoke a negative acceleration in the y-axis due to the coupled motion. Assuming that no large deviations occur from the Sun-NEO line and that the SRP remains constant, if the velocity is reflected ideally when the lower boundary is hit, the spacecraft will return to the initial x-position but with a negative Δy position. This is due to the fact that during the way back, the x-velocity is negative and thus an acceleration equal to the one before but opposite sign is created which brings the velocity in the y-direction back to zero. From this fact, one can think that if we increase the reflected speed, the spacecraft will travel more time with negative x-velocity and thus more time inducing a positive lateral acceleration. If we are able to predict which velocity is needed so that the spacecraft returns to the initial position without any Δy, we could be able to draw a "drop" that keeps the spacecraft in a fix relative position. This is exemplified in Figure 3.15 where a "drop" is formed at ${}^{\text{neoS}}y_{\text{S/C}} = -10$ m.

In practice, this approach is very difficult to be implemented and no control law was found to generate the hysteresis values in an automated way. Also, this approach is too sensitive to navigation errors. To overcome this problem, lateral motion was allowed. This is, when the spacecraft moves with negative y-velocity, the resultant speed is incremented (hysteresis > 1) at each command so that the positive y-acceleration induced switches from negative to positive y-velocity. By contrary when the y-velocity is positive the resultant speed is decreased (hysteresis < 1) so that the negative y-acceleration induced switches from positive to negative y-velocity. Mathematically, this is represented as:

$$\mathbf{v}_+ = \begin{pmatrix} -h(y)\mathrm{v}_{x-} \\ \mathrm{v}_{y-} \\ -h_c\mathrm{v}_{z-} \end{pmatrix} \tag{3.20}$$

where the hysteresis h is:

$$h(y) = 1 - K_h\frac{y}{y_{\text{lim}}} \tag{3.21}$$

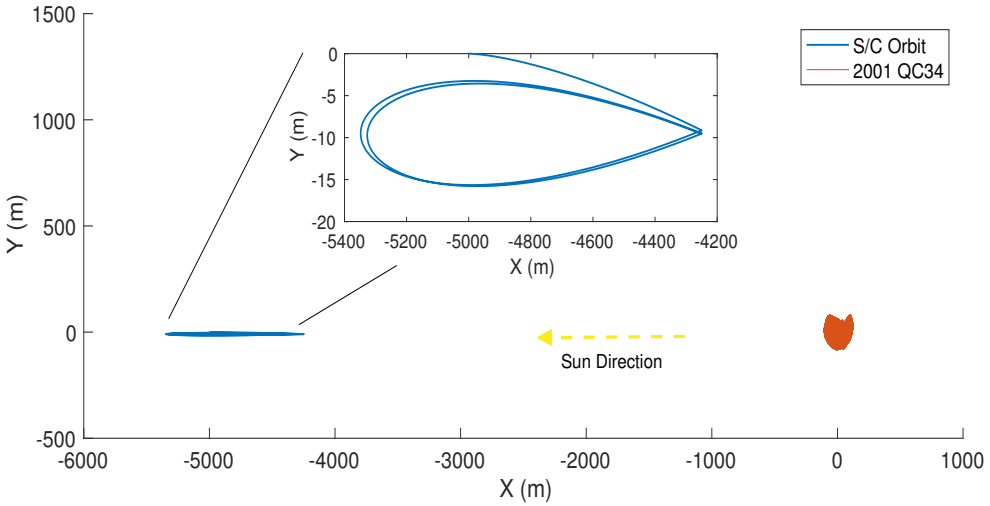

Figure 3.15: Orbit projection in the neoS frame using equations Equation (3.6) where the hysteresis values at each manoeuvre have been manually tuned to achieve the desired shape. No thrusting errors have been included.

K_h and y_{lim} being both constants, where $y_{\text{lim}} = 500$ m setting the boundary to ± 500 m (in case $K_h = 1$) and $K_h = 0.1$ tunes this boundary to provide flexibility to the system. As this method controls the y-direction by controlling x-direction, only a lower boundary has been defined $\sqrt{x^2+y^2+z^2} < d_{\text{ref}}(1-0.15)$ and thus this method is not studied within the previously defined control boxes (Section 3.1.2).

During this section, we have not talked about the motion in z-direction due to the fact that this motion is not coupled with the in-plane one (ideally). In general, it is desired that the spacecraft remains within the orbital plane, for that reason a constant hysteresis in the z-direction ($h_c = 0.9$) is applied so that the misalignment effects in this direction are corrected as much as possible. Figures 3.16 and 3.17 show the resultant trajectories in an ideal environment (i.e. no thrust errors, no desaturation manoeuvres) only with an initial arbitrary error in velocity and position according to the navigation performance system (Section 3.2). Actually, this fact is the responsible of the spacecraft to start with positive y-velocity (Figure 3.17). In Figure 3.16, it is possible to observed the set of "drops" mentioned before, whereas having a look at Figure 3.17, and particularly in the y-direction, it is possible to see that the motion is bounded between ± 40 m for a period of two months.

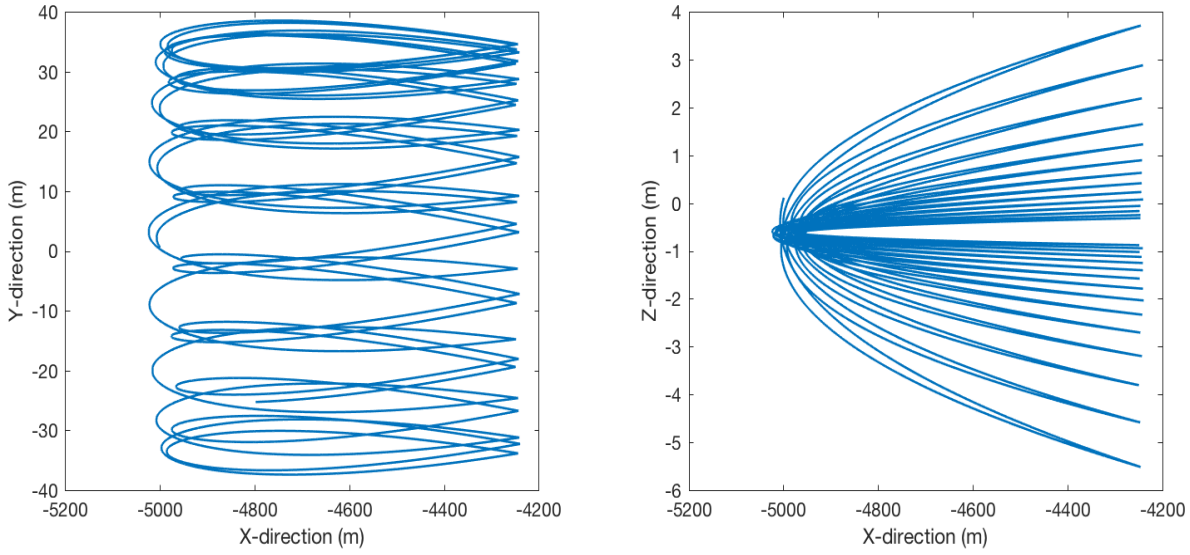

Figure 3.16: Orbit projection in the neoS frame during a 56 days period. Ideal trajectory obtained from Equation (3.6).

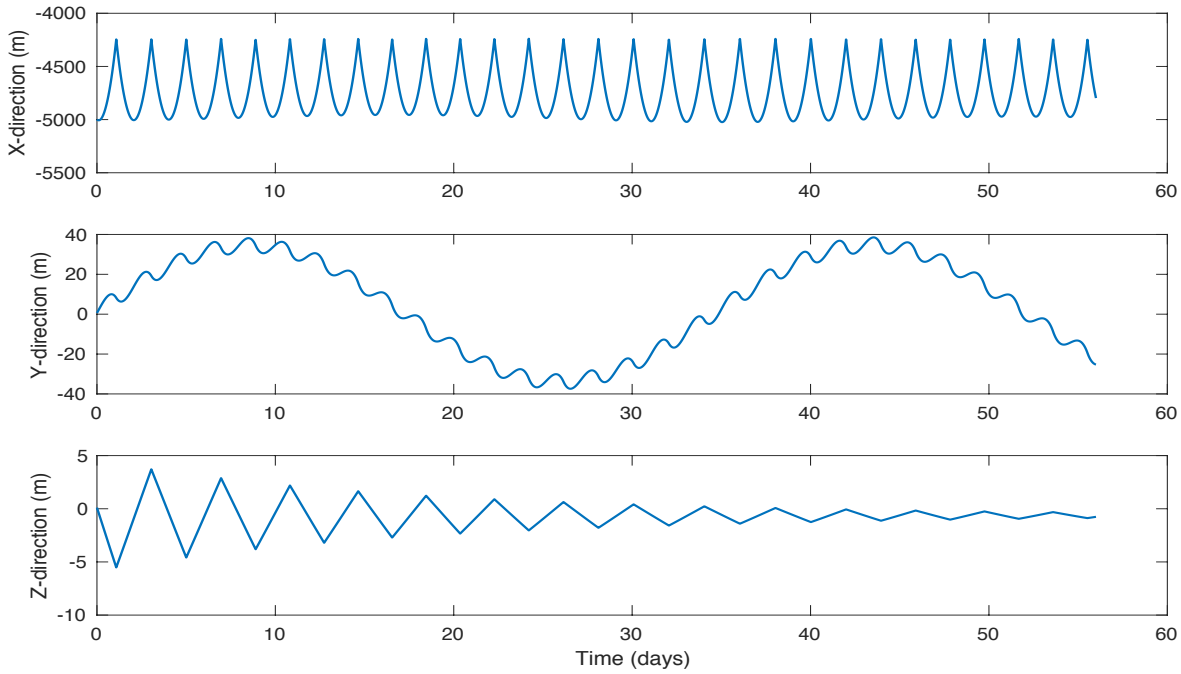

Figure 3.17: Time variation of the position in the neoS frame. Ideal trajectory obtained from Equation (3.6).

However, when relaxing the assumptions made and including thrusting errors, desaturation manoeuvres, irregularities of the NEO and other perturbations present in the E2ESS, the algorithm needs to be modified to make it more robust. To do this a new conditions were established so that the hysteresis value remains within a certain values and z-velocity deals with uncertainties.

$$(\mathrm{v}_{y-} < 0 \quad \&\& \quad y > 0) \quad || \quad (\mathrm{v}_{y-} > 0 \quad \&\& \quad y < 0) \quad \longrightarrow \quad h(y) = 1 \quad \text{otherwise} \quad h(y) = 1 - K_h \frac{y}{y_{\text{lim}}}$$

$$(\mathrm{v}_{z-} < 0 \quad \&\& \quad z > 0) \quad || \quad (\mathrm{v}_{z-} > 0 \quad \&\& \quad z < 0) \quad \longrightarrow \quad \mathrm{v}_{z+} = h_c \mathrm{v}_{z-} \quad \text{otherwise} \quad \mathrm{v}_{z+} = -h_c \mathrm{v}_{z-}$$

3.3.2. LYAPUNOV CONTROL FUNCTION

The second approach proposed is based on a Lyapunov control function. Having a Lyapunov candidate function of the form:

$$V = \frac{1}{2}\mathbf{v}^T\mathbf{v} + \frac{1}{2}K_p\left(\mathbf{r}-\mathbf{r}_{\text{ref}}\right)^T\left(\mathbf{r}-\mathbf{r}_{\text{ref}}\right) \tag{3.22}$$

it is possible to define a control such as:

$$\mathbf{u} = -\left(\frac{\partial U}{\partial \mathbf{r}} + \mathbf{a}_{SRP}\right) - K_p\left(\mathbf{r}-\mathbf{r}_{\text{ref}}\right) - K_v\mathbf{v} \tag{3.23}$$

that introduced in

$$\frac{dV}{dt} = \mathbf{v}^T\dot{\mathbf{v}} + K_p\left(\mathbf{r}-\mathbf{r}_{\text{ref}}\right)^T\mathbf{v} \tag{3.24}$$

$$= \mathbf{v}^T\left(\frac{\partial U}{\partial \mathbf{r}} + \mathbf{a}_{SRP} + \mathbf{u}\right) + K_p\left(\mathbf{r}-\mathbf{r}_{\text{ref}}\right)^T\mathbf{v} \tag{3.25}$$

$$= -K_v\mathbf{v}^T\mathbf{v} < 0 \tag{3.26}$$

ensures asymptotic stability.

As seen in Figure 2.5 the gravity field can be approximated to $-\frac{\mu_{\text{NEO}}}{r^3}\mathbf{r}$ with an error about $1-5\%$ of the actual value. Furthermore, the main acceleration is caused by SRP (Figure 2.6) which justifies even more

this assumption. The estimation of the SRP acceleration is provided by the navigation system as seen in Section 3.2.

In Vetrisano and Cano, a Lyapunov control based function was designed to control the spacecraft during near-inertial hovering. However, the controller was designed for continuous (low) thrust which cannot be applied for the current spacecraft configuration. Here, a different approach is taken using the Lyapunov function. Instead of controlling the spacecraft in a fixed position in a continuous way, the spacecraft is controlled in a continuous way (by the chemical thrusters) once this is outside the boundary walls. Then, the objective of this controller is to return the spacecraft to the control box with sufficiently large velocity that minimizes the manoeuvres performed. This presents several problems when tuning the gains. First, no reference position is available for studying the final state error. Second, almost no information can be derived from the overshooting in the boundaries as this error is not related with the number of manoeuvres. To visualize the latter effect, one can imagine an impulsive manoeuvre that crosses the entire control box within an order of magnitude of minutes instead of days (objective). If the navigation updates the state sufficiently fast, the overshooting can be of the order of meters or less. To overcome these issues the gains have been tuned formulating the problem as an optimization problem as follows:

$$\begin{aligned} \text{find:} \quad & 0 < K_p < 0.001 \\ & 0 < K_v < 1 \\ & x_{\text{ref}}(1+S) < x^*_{\text{ref}} < x_{\text{ref}} \\ \text{to minimize:} \quad & n \in \mathbb{N} \end{aligned} \tag{3.27}$$

where n is the total number of manoeuvres and x^*_{ref} is a target position along the Sun-NEO line. The reason for introducing this variable is the following. Imagine that a sphere with radius 500 m has been defined as a control box. Even if this sphere is centered in $\mathbf{r}_{\text{ref}}$, the final objective would be to place the spacecraft with zero velocity in the upper boundary ($[-5500, 0, 0]^T$) so that the SRP brings the spacecraft towards the lower boundary ($[-4500, 0, 0]^T$) with no propellant consumption (i.e, solar sail).

The boundary limits for K_p and K_v are defined with a simple preliminary analysis. If $\mathbf{r} - \mathbf{r}_{\text{ref}} \sim 10^3$ m and the ΔV order of magnitude is $10^{-1} - 10^{-2}$ m/s, K_p must be less than 10^{-3} s^{-2}. Same reasoning applies to K_v.

The optimization problem has been solved using open source optimization libraries developed by the ESA Advanced Concepts Team (ACT). These are Parallel Global Multiobjective Optimizer (PaGMO) and Python Parallel Global Multiobjective Optimizer (PyGMO) in its second version[1]. In particular the algorithm employed has been the Differential Evolution (DE) developed by (Storn and Price, 1997) using its recommended values for crossover and weighting factor. The initial population has been set to 200 individuals achieving convergence in $\approx 200 - 300$ iterations. The reason for setting the individual population to 200 individuals is due to the fact that at the first epoch, most of the individuals either perform very high impulsive manoeuvres or by contrary, many manoeuvres with low thrust propulsion. The results obtained were:

- $r = 500$ m : $K_p = 4.184 \cdot 10^{-7}$ s^{-2}; $K_d = 2.250 \cdot 10^{-2}$ s^{-1}; $x^*_{\text{ref}} = -5364.44$ m
- $r = 750$ m : $K_p = 2.828 \cdot 10^{-7}$ s^{-2}; $K_d = 1.995 \cdot 10^{-2}$ s^{-1}; $x^*_{\text{ref}} = -5574.14$ m

In both cases, K_d was slightly modified to compensate the errors caused by the estimation of $\mathbf{a}_{\text{SRP}}$, as this error was not included in the simplified problem optimized by the package. The final values are:

- $r = 500$ m : $K_p = 4.184 \cdot 10^{-7}$ s^{-2}; $K_d = 1.450 \cdot 10^{-2}$ s^{-1}; $x^*_{\text{ref}} = -5364.44$ m
- $r = 750$ m : $K_p = 2.828 \cdot 10^{-7}$ s^{-2}; $K_d = 1.495 \cdot 10^{-2}$ s^{-1}; $x^*_{\text{ref}} = -5574.14$ m

Note that with this method, the resultant $\mathbf{v}_+$ velocity is not just a manipulation of the incoming velocity and other factors are taken into account (relative position, SRP and gravity field).

3.4. RESULTS

In this section, performance analysis testing the different guidance and control strategies are presented. The parameters that are are going to be monitored to evaluate the performance are: overshooting in the boundaries, frequency of manoeuvres and amount of ΔV per day spent. These factors obey to the performance requirements specified in Section 1.3.

[1] PaGMO and PyGMO: https://esa.github.io/pagmo2/index.html. Accessed: 24-07-2017

3.4.1. MONTE CARLO SIMULATION

As the motion in the vicinity of the asteroid is too complex, the stability and robustness of the guidance and control strategies are tested in a numerical way through Monte Carlo simulations. In order to verify each of the requirements with 95% accuracy and confidence, the guideline specified in ECSS (2014) have been used. This guideline is shown in Figure 3.18. The confidence level is plotted as a function of the number of runs for the cases of no failure and a single failure. This means that if for example 58 simulation runs fulfil a specified requirement, that requirement is verified with a level of confidence and accuracy of 95%. If among the 58 runs, there is one run that does not fulfil the requirements, then a total of 92 runs with only that single failure need to be simulated to achieve the mentioned level of confidence and accuracy. Each of the simulations have been run for a period of 14 days.

NS-GNC-02 defines a lower boundary for minimum performance. However, it is also important to define an upper maximum boundary that can be achieved. Figure 3.19 defines this boundary. This number is obtained assuming that and impulse is performed in the lower boundary of the control box so that places the spacecraft in the upper boundary with zero velocity. Then the spacecraft would fall again into the lower

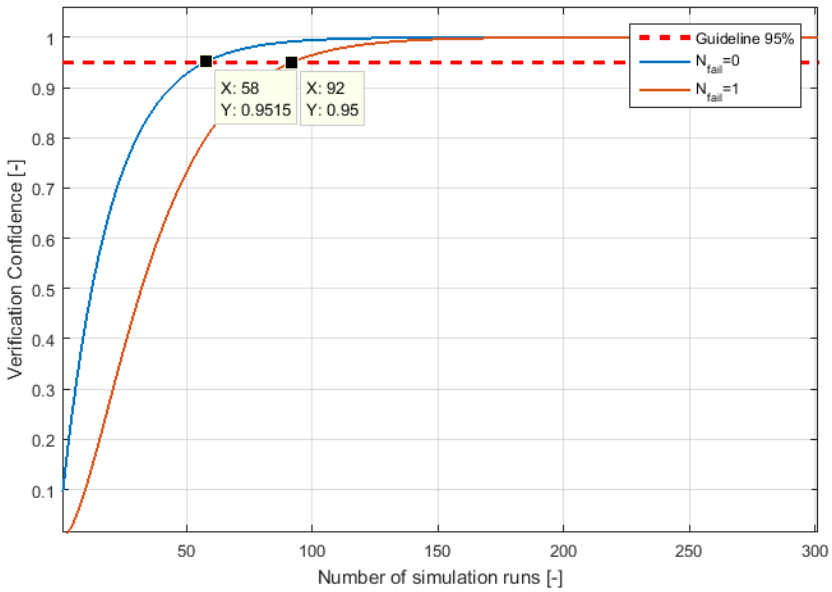

Figure 3.18: Simulation runs to verify a requirement at accuracy of 95% vs. verification confidence (ECSS, 2014)

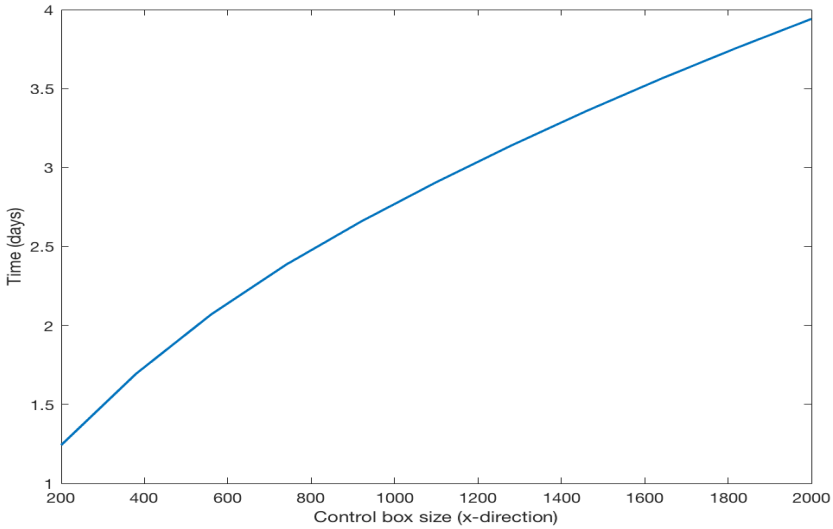

Figure 3.19: Minimum thrust frequency as a function of the control box size

boundary by the action of the accelerations. This number also assumes that no lateral acceleration appear or that they are compensated. This number is an ideal number that could be achieved via manual commanding. However, the purpose of our control system is to operate without ground support.

Each of the requirement tested has been organized using histograms for each of the performed runs to better visualize the trend. The boundary limits specified by the performance requirements are highlighted in red. Special cases have been treated in a separate way.

To include the accelerations caused by thrust errors/misalignments a noise in the commanded ΔV of 2 mm/s (3 σ) has been added. This is more or less 10% of a typical ΔV manoeuvre (a couple of cm/s). To account for the translational errors due to momentum dumping, Antreasian et al. (2016) has been taken as a reference, where a value of 0.5 mm/s is reported. Here a conservative approach has been chosen of 1 mm/s (3 σ).

3.4.2. REFLECTION

The first method tested is the reflection method. Analysing the results it can be seen that even though for large control boxes the performance remains within the limits defined, this is not the case specially for smaller control boxes (Figures 3.20 and 3.21). Looking at the number of commands per day (Figure 3.20), S1 and S2 small exceed the requirement limit in several runs. This behaviour is also seen in the amount of ΔV spent (Figure 3.21), as more manoeuvres denote an inefficient way to operate and thus, the consumption increases. In principle, one can think that increasing the control box the performance can be improved, but for sufficiently long times (28 days) this also happens for the large control boxes. The reason for this behaviour obeys two factors that have nothing to do with the size.

The first one is purely related with the geometry of the control box and the own definition of the reflection method. Observing Figure 3.22 (black pointed area) this effect is clearly observed. As the reflection of the velocity only changes the radial component, keeping the tangential speed and due to the shape of the control box. When the orbit is close to an edge, the spacecraft hits two walls in a relative short time. This effect can be reduced in frequency increasing the size of the control box, however at some point two almost consecutive manoeuvres will be carried out. This fact also explains why the small large control boxes have better performance.

The second reason for explaining the low performance of this method is a mix of geometrical factors

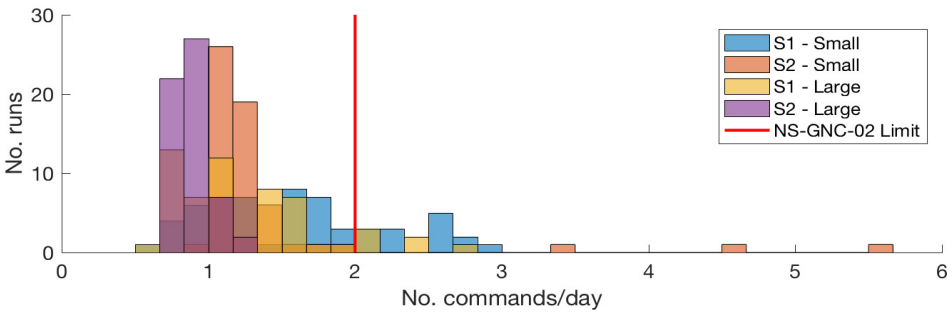

Figure 3.20: Number of manoeuvres performed per day for different control box shapes and sizes using reflection method.

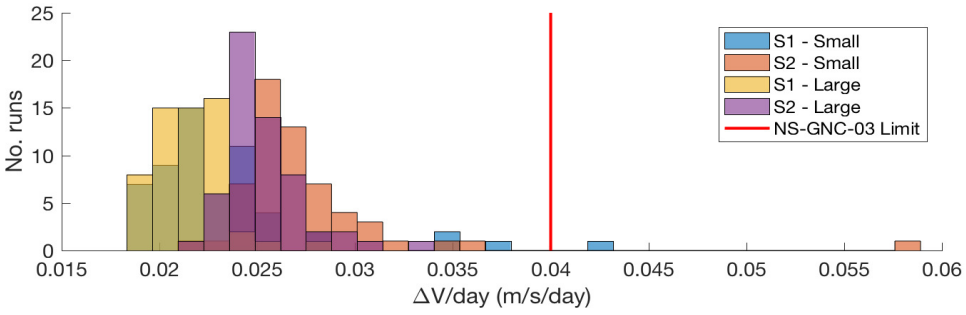

Figure 3.21: Total amount of ΔV per day for different control box shapes and sizes using reflection method.

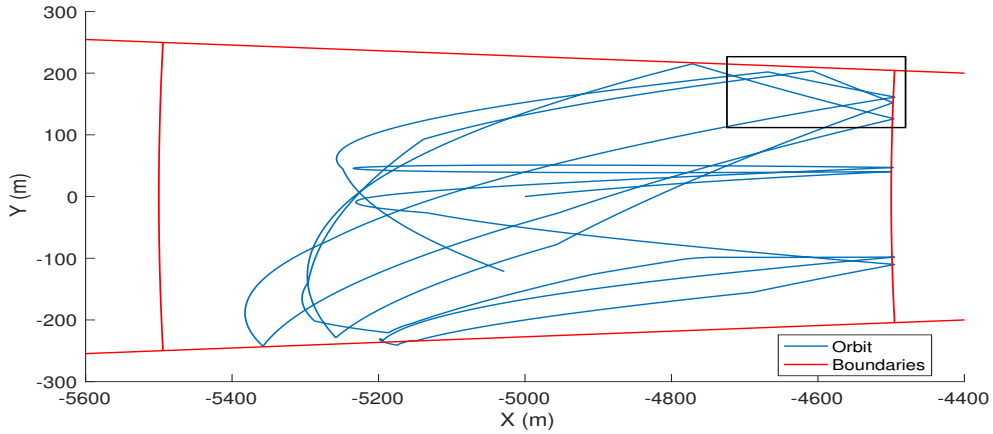

Figure 3.22: Orbit projection X-Y plane in the neoS frame for run no. 12 using reflection method and S1 small as a boundary box.

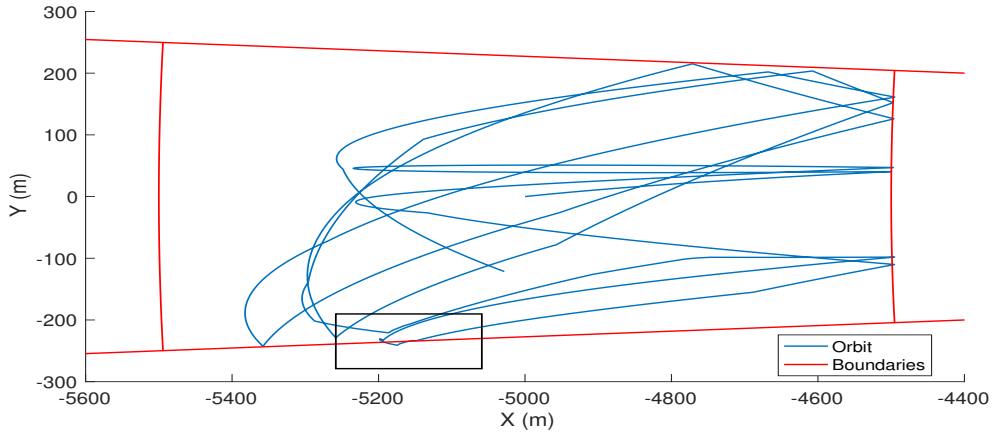

Figure 3.23: Orbit projection X-Y plane in the neoS frame for run no. 12 using reflection method and S1 small as a boundary box.

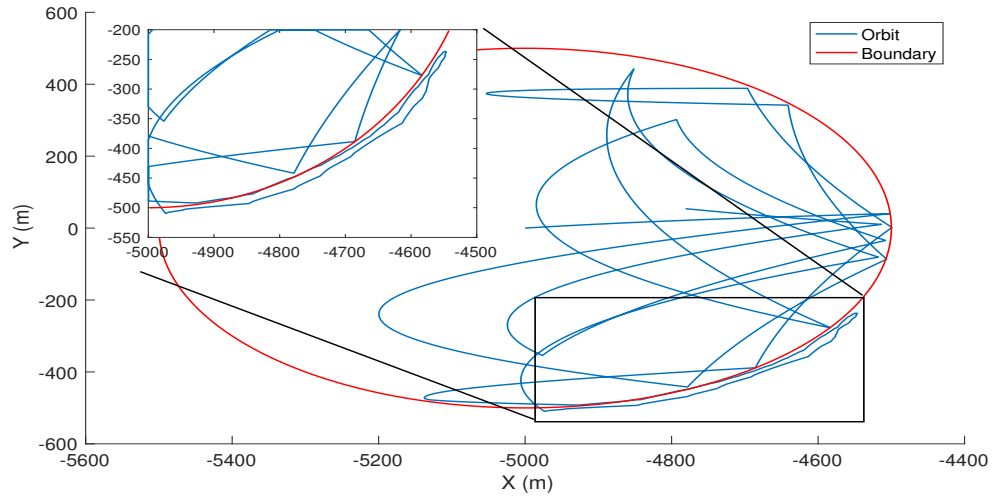

Figure 3.24: Orbit projection X-Y plane in the neoS frame for run no. 36 using reflection method and S2 small as a boundary box.

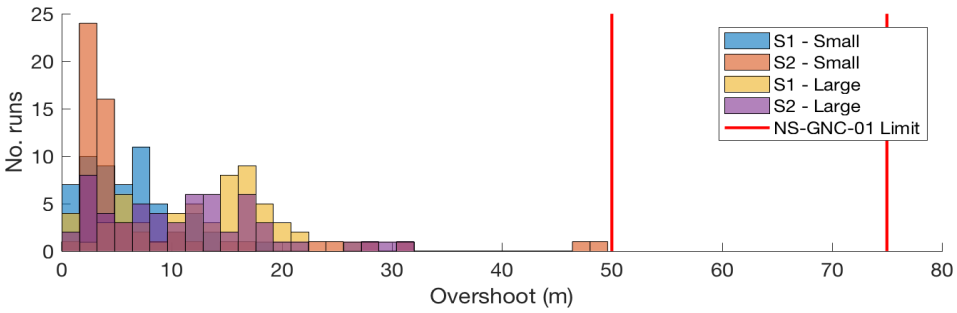

Figure 3.25: Boundary overshooting for different control box shapes and sizes using reflection method.

combined with the lateral accelerations that appear due to the centrifugal motion. This effect is seen in both Figures 3.23 and 3.24. First Figure 3.23 is analysed. In this case assume the case that after a bounce the spacecraft moves away from the asteroid until the combination of the SRP and gravity field of the NEO pushes again the spacecraft towards the asteroid. Now assume that the bounce has placed the spacecraft near the wall with a velocity vector almost tangential to the boundary limit. If the spacecraft is approximating to the NEO (moving in the x-direction) the induced lateral acceleration will be negative inducing also a negative velocity that will provoke that the spacecraft hits the wall. In this case, the incoming radial velocity is very small (so the resultant too) and the spacecraft will continue its motion along the positive x-direction hitting the wall again and again (black pointed area of Figure 3.23). This effect is better appreciated in Figure 3.24. Here in the zoomed area it is clearer than when the spacecraft hits the wall in an almost tangential direction the control method will tend to keep the spacecraft in the boundary limit increasing the number of commands.

Regarding the overshooting in the boundaries Figure 3.25, the results show that the updating rate of the navigation system (1/60 Hz) is enough for keeping the spacecraft within the performance requirements established.

3.4.3. INVERSION

The effect described in Section 3.4.2 is more evident in this case, causing the method to fail (Figures 3.26 to 3.28), and even diverge in all the cases for sufficiently long times (28 days). In Figure 3.26, it is possible to see that only S2 large stays within the number of commands limit, whereas the majority of the other evaluated cases achieve unfeasible values. However, it is not possible to conclude that this method works for large control boxes, as the mentioned result is fictitious. The reason for this is that to compute the results from Figure 3.26 the average of the total number of commands divided by the total number of days is taken. This method works well for short time periods (a couple of days) but the longer the time simulation the worse the results. Also, when the method has diverged, the number of commands is constrained by the navigation system limiting the amount of manoeuvres that can be commanded.

A more realistic perspective is found in Figures 3.27 and 3.28. Here, it is seen that the majority of runs for all the boundary surfaces are found beyond the established performance limits. This is because with sufficiently long times, the spacecraft gets stuck into the boundary. This fact provokes that first, the number of ΔV per manoeuvre is increased and second, the control box is exited because the navigation system is not able to update the state with the achieved velocities. To better visualize what is happening for the majority of runs, Figures 3.29 to 3.32 have been generated.

The reason for the low performance obeys to definition of the method itself. Inverting the incoming velocity causes the problem to get stuck near the boundaries at some point of the trajectory. This is specially common for the boundaries tested (S1 and S2) because both have lateral convex surfaces. In Figure 3.29, if a slice is taken in the selected area (black pointed area), Figure 3.30 is obtained. In this image, it can be seen that after some manoeuvres the trajectory hits the wall in a tangential way causing, due to the convexity, that the orbit gets stuck in a certain area. Note that in these simulations thrusting errors and misalignments are included, fact that explains why when the velocity is inverted, the spacecraft does not follow exactly the incoming path.

What occurs in Figures 3.31 and 3.32 is that once the spacecraft gets stuck in a really narrow region, the navigation system is not able to update the position with a rate (update rate 1/60 Hz) high enough to describe the motion of the spacecraft. This cause that at each manoeuvre, the spacecraft goes further and further beyond the limits. This oscillating behaviour is better observed in Figure 3.31, where the sudden changes in

the velocity in a short time period make that the spacecraft gains more and more velocity until at some point, the problem diverges, achieving the infeasible values showed in Figures 3.26 and 3.27.

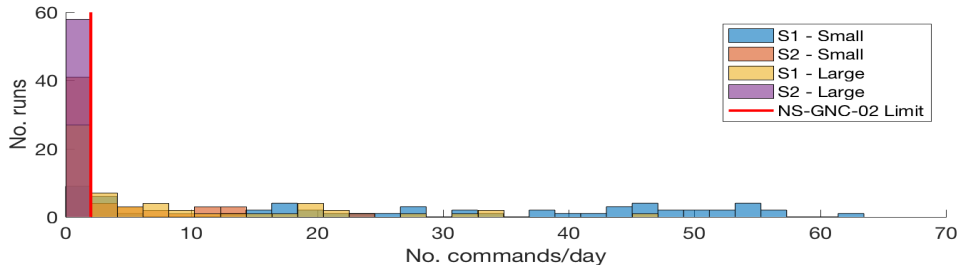

Figure 3.26: Number of manoeuvres performed per day for different control box shapes and sizes using inversion method.

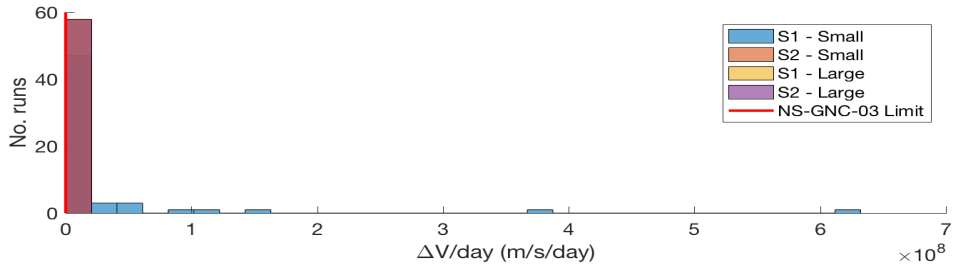

Figure 3.27: Total amount of ΔV per day for different control box shapes and sizes using inversion method.

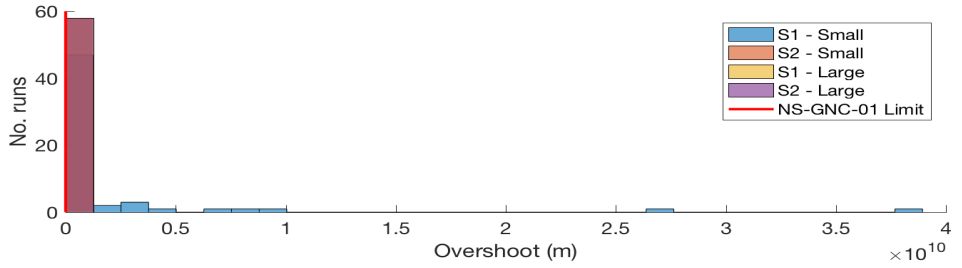

Figure 3.28: Boundary overshooting for different control box shapes and sizes using inversion method.

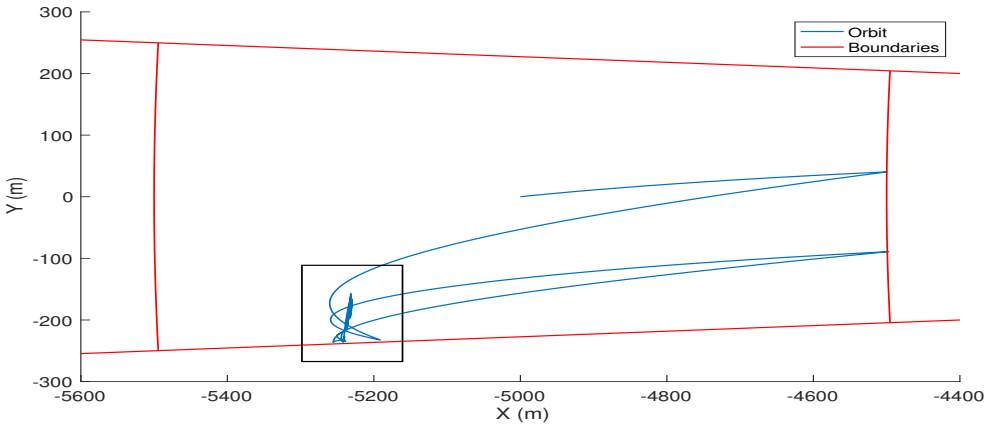

Figure 3.29: Orbit projection X-Y plane in the neoS frame for run no. 2 using inversion method and S1 small as a boundary box. 5 simulation days are shown.

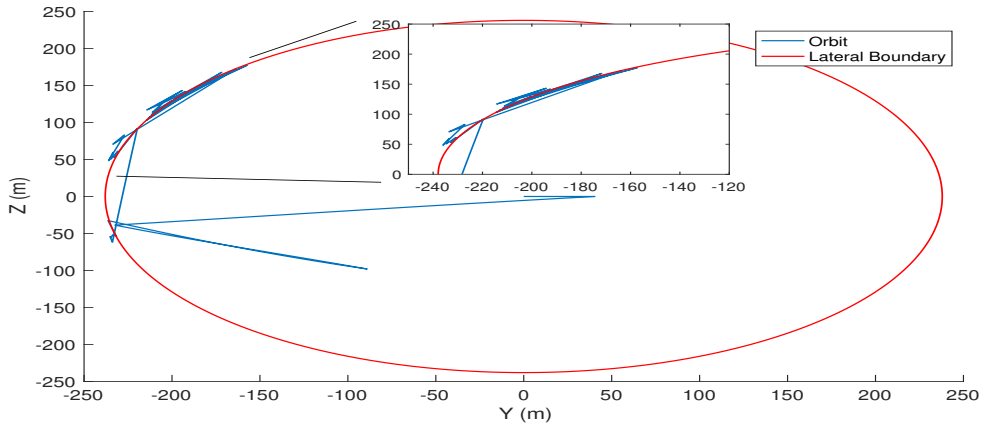

Figure 3.30: Cross-sectional plane located at $x = -5235$ m in the neoS frame for run no. 2 using inversion method and S1 small as a boundary box. 5 simulation days are shown.

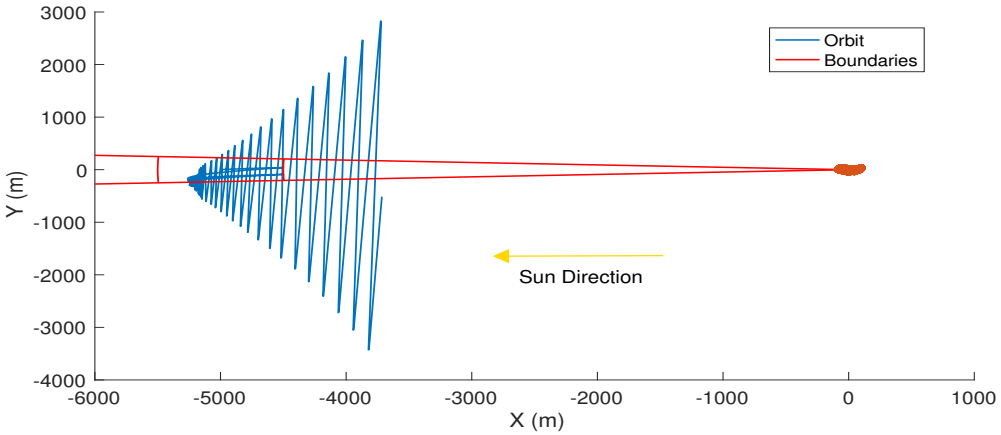

Figure 3.31: Orbit projection X-Y plane in the neoS frame for run no. 2 using inversion method and S1 small as a boundary box. 5 simulation days are shown.

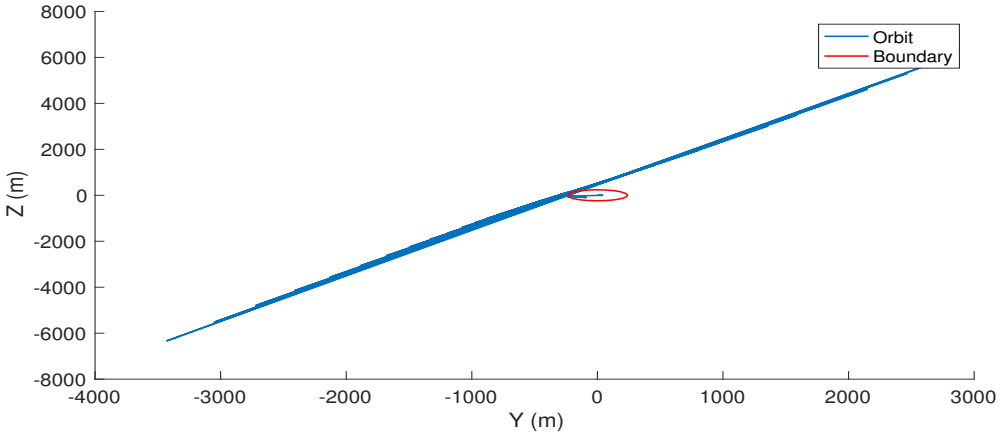

Figure 3.32: Cross-sectional plane located at $x = -5235$ m in the neoS frame for run no. 2 using inversion method and S1 small as a boundary box. 6 simulation days are shown.

3.4.4. CENTRAL REFLECTION

To overcome the mentioned problems, central reflection method makes that the resultant velocity ($\mathbf{v}_+$) is always directed towards the reference point. For this method, S1 has been abandoned for being S2 more natural geometrically speaking. This is due to the fact that the normal vector to the surface has the same direction as $\mathbf{v}_+$. Note that if S1 is used, to align $\mathbf{v}_+$ with the normal vector to the walls is not recommended, because the concavity of the lower boundary may push the spacecraft towards lateral boundaries. The reference point in this case, it is referred as the center of the sphere. The fact of always reflecting the velocity towards the center of the sphere provokes that the spacecraft does not get stuck near the boundaries achieving a performance within the specified limits (Figures 3.33 to 3.35) with wide margins. Figure 3.33 shows that for the small boundary case the average commands per day is around 1. This value is clearly improved by increasing the size of the control box, fact that also affects in terms of ΔV spent, improving also the amount of propellant Figure 3.34. The penalty in terms of overshooting Figure 3.35 is justified as they represent 1/3 of the maximum allowable value. This penalty is due to the fact that the larger the control box, the larger the velocities. If the update rate of the navigation system is kept constant, the spacecraft travels more distance before the system notices that it is outside the control box.

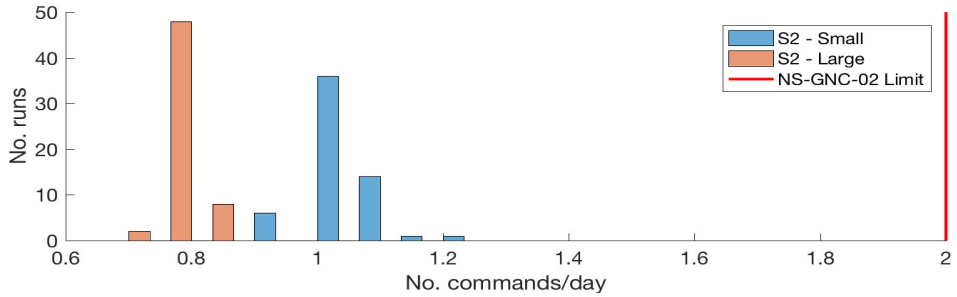

Figure 3.33: Number of manoeuvres performed per day for different control box sizes using central reflection method.

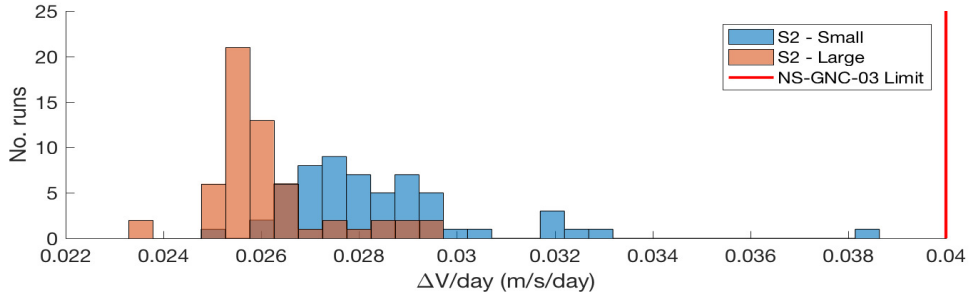

Figure 3.34: Total amount of ΔV per day for different control box sizes using central reflection method.

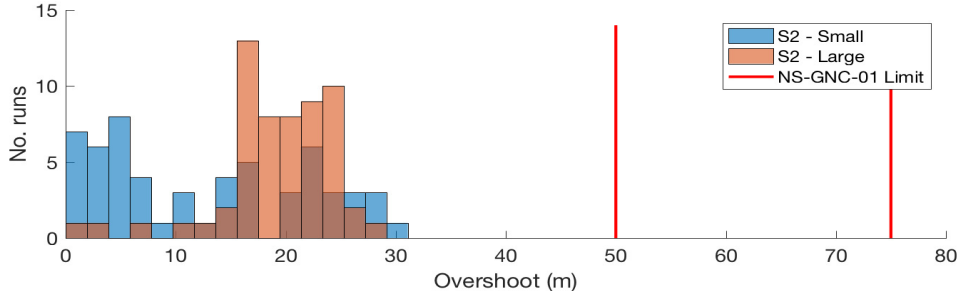

Figure 3.35: Boundary overshooting for different control box sizes using central reflection method.

3.4.5. HYSTERESIS CONTROL

For the characteristics of this method in which lateral motion is controlled by radial velocity changes, only a lower boundary is specified (same as the lower boundary for S1 large). Due to this, no overshooting is evaluated as it does not make sense to compare it with the previous results. However, this motion has found to be not yet feasible for the mission. Here, the reasons why are explained.

Figures 3.36 and 3.37 represent the best and worst case for a Monte Carlo simulation in which the criterion for deciding the level of success of the controller is the maximum displacement in the y-direction from the Sun-NEO line.

The reason for explaining the difference in performance between both cases can be found in Figure 3.38. Analysing the velocity in the y-direction it is seen that the resultant trajectory is highly influenced by the starting initial velocity (during the first instant the EKF does not have its optimum performance), desaturation commands (~ day 7) and errors in the commanded thrust magnitude plus misalignment errors. Specially the

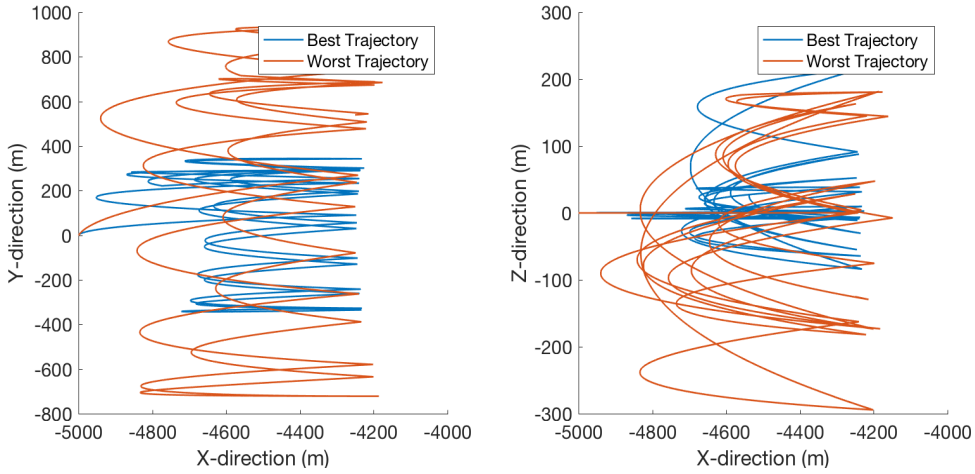

Figure 3.36: Orbit projection of the best and worst case of a 58-trajectory Monte Carlo run in the neoS frame during a 28 days period using the E2ESS.

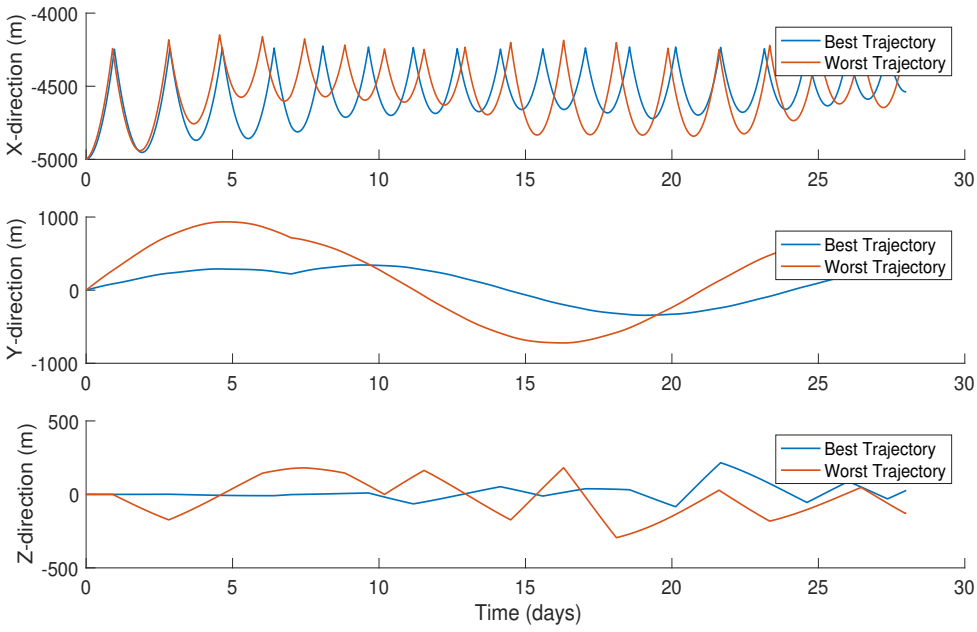

Figure 3.37: Time variation of the position of the best and worst case of a 58-trajectory Monte Carlo run in the neoS frame during a 28 days period using the E2ESS.

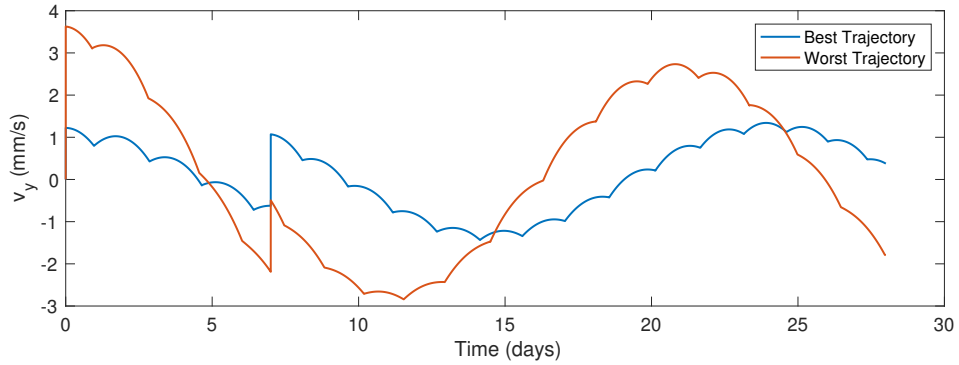

Figure 3.38: Y-velocity variation of the position of the best and worst case of a 58-trajectory Monte Carlo run in the neoS frame during a 28 days period using the E2ESS.

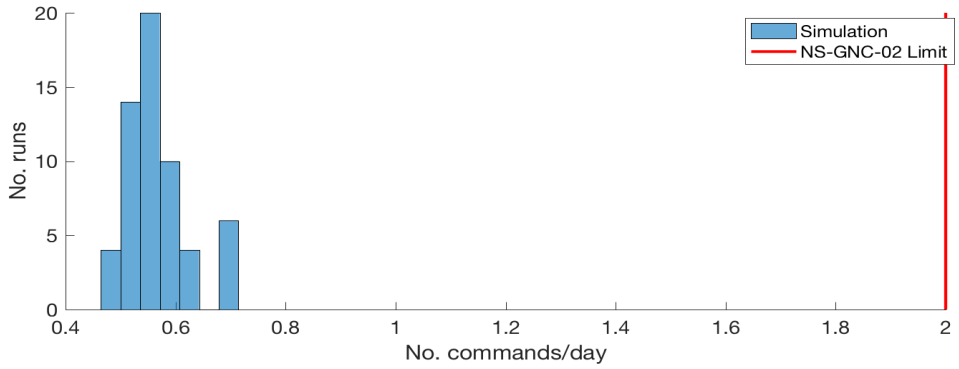

Figure 3.39: Number of manoeuvres performed per day using an hysteresis based control function.

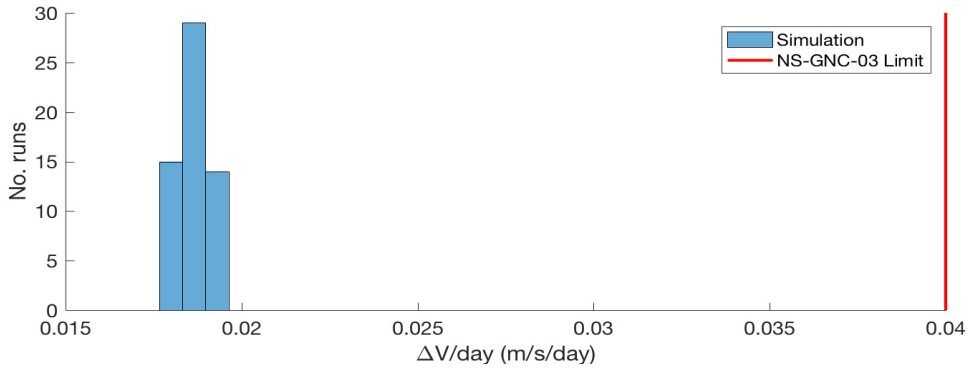

Figure 3.40: Total amount of ΔV per day using an hysteresis based control function.

first two sources of error are the ones that drive the motion of the orbit. Imaging the case that no desaturation command is executed and that the initial error is minimum (i.e. best case without desaturation command). Then the trend followed by the velocity and position in the y-direction would oscillate with period $\sim$ 28 days Figures 3.37 and 3.38 bounding the y-motion. The solution obtained would be close to the ideal case showed in Equation (3.6).

Even so, in Figures 3.39 and 3.40 it can be observed that this method is the best one in terms of no. of commands per day and ΔV spent, but with the current errors no bounded region can be ensured and for safety reasons this method is abandoned. The author recommends further research in missions where the mentioned effects can be minimized (e.g. using electric propulsion, uncoupling rotational and translational motion when the thrusters are fired for both desaturation of the wheels and commanded ΔV, reducing the uncertainties in the navigation system or locating the thrusters in a different disposition).

3.4.6. LYAPUNOV CONTROLLER

Finally, the results for the Lyapunov based controller are presented. Analysing the performance, it can be seen that this method outperforms the rest commanding about 0.6 manoeuvres per day (Figure 3.41), which means almost a manoeuvre per 2 days. It is important to highlight that the limit for a boundary box of this size was set to a manoeuvre per 3 days Figure 3.19. Observing Figures 3.42 and 3.43, it is possible to see that in terms of ΔV spent and overshooting, it is also the best method surpassing central reflection (Section 3.4.4). This is due to the fact that this method uses the full span of the control box, optimizing the commands. As the ΔV is optimize, no extra velocity is applied keeping the spacecraft with low velocities and thus, the navigation system can reduce the overshooting.

The advantages of this method over the previous ones has to do with its robustness. So far, the tested methods were highly dependent of the incoming velocity. This provokes that if for example by error a larger commanded thrust manoeuvre is performed, at the next manoeuvre the energy will be kept, decreasing the performance. However, in this method the resultant velocity is a combination of the action of the external accelerations and the position and velocity compared with their respective reference values. This fact provokes that if the same example is applied and the spacecraft incoming velocity is too high, the control strategy will reduce the velocity to adapt it to the desired one. For this reason, this method is used as a baseline method.

In this method, the box has not been tested, as it does not influence the direction of the commanded manoeuvre (i.e, no information about the normal vector of the boundary is required).

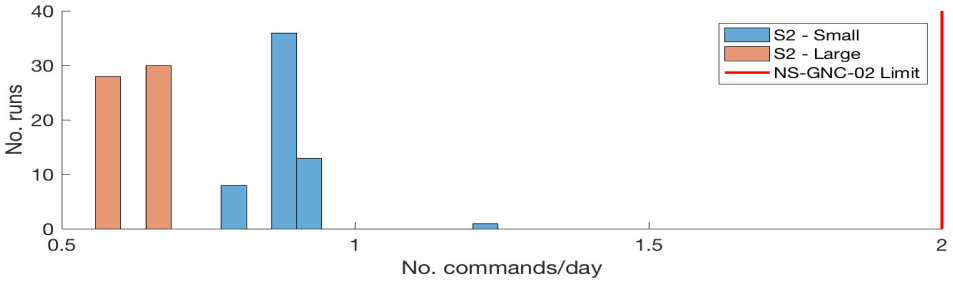

Figure 3.41: Number of manoeuvres performed per day for different control box sizes using a Lyapunov based control function.

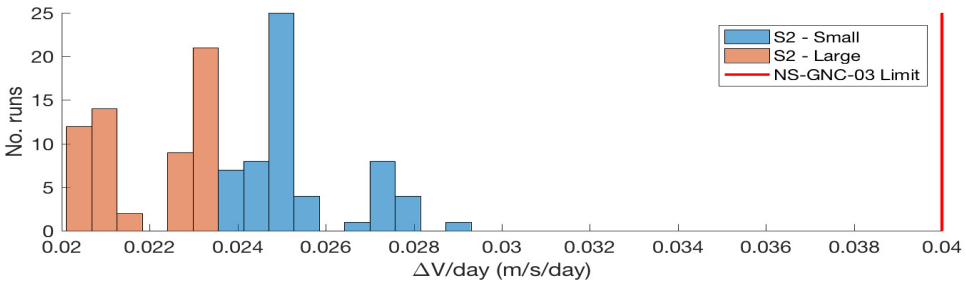

Figure 3.42: Total amount of ΔV per day for different control box sizes using a Lyapunov based control function.

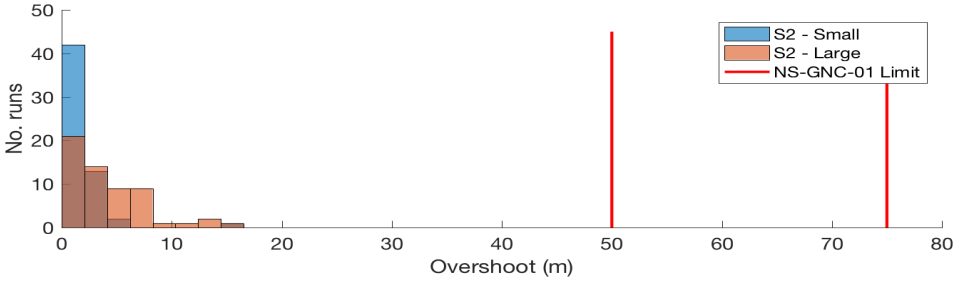

Figure 3.43: Boundary overshooting for different control box sizes using a Lyapunov based control function.

3.5. BASELINE TRAJECTORY

Based on the results achieved, a baseline trajectory that will be used for attitude design is defined. This trajectory is obtained using the Lyapunov control function as a control strategy and a sphere of 1500 m of diameter as a control box (S2 large). This method has outperformed in terms number of commands per day over the rest and it has also shown more robustness. In Figure 3.44, the three-dimensional trajectory together with their projections in the XY and XZ plane is shown. It can be seen that the controller thrust in a lateral way, using the complete span of the control box. Fact which is the responsible for achieving long periods of time without thrusting manoeuvres. The relevant performance values for the baseline orbit are shown in Table 3.2.

Table 3.2: Control performance values for the baseline orbit using a Lyapunov control strategy.

Baseline Trajectory	
Total no. manoeuvres	17
No. maneouvers per day	0.6
Maximum ΔV	0.0411 m/s
Minimum ΔV	0.0284 m/s
ΔV/day	0.0217 m/s

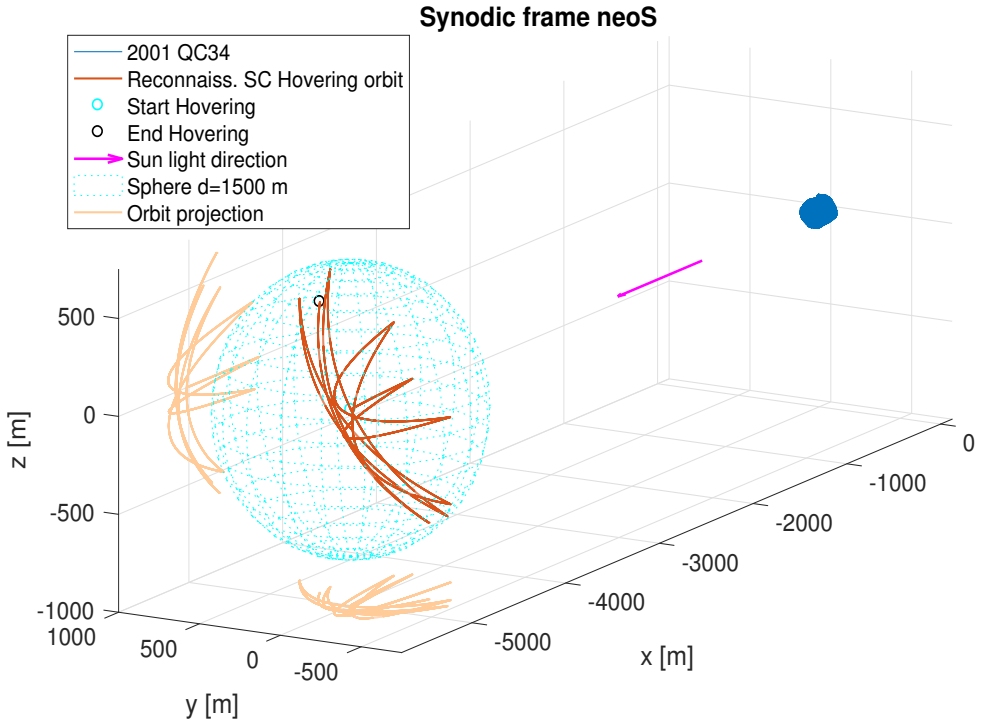

Figure 3.44: Baseline trajectory using Lyapunov control function for an sphere of 1500 m of diameter during 14 days in the neoS frame.

4

ROTATIONAL GNC

The objective of this chapter is to design a robust guidance, navigation and control algorithm for the rotational motion that ensures to limit the attitude performance below the boundary established by the performance requirement NS-GNC-04, while avoiding that the image is blurred (NS-GNC-05). Also the momentum dumping will be treated to see how sensitive is the translational GNC to these manoeuvres. Slew manoeuvres will not be treated as they are not required for the observation phase.

The chapter presents first the sensor and actuator models used for this study. It continues with the definition of the guidance law using the trajectory information obtained in Chapter 3. Then an attitude determination algorithm based on low-pass filtering is explained and the control strategy is defined. The chapter finalizes with the pointing performance results for both nominal pointing and momentum dumping.

4.1. SENSOR AND ACTUATOR MODELS

Sensors and actuators are a key point when developing an attitude control algorithm as they are the main restricting factors that affect the pointing performance. Commercial hardware is chosen to lower the cost of the mission and this section collects their characteristics. The reason why this specific hardware has been chosen for this purpose obeys mission specifications that can be found in Ziegler and Delchambre (2016). However, these are quite standard devices Chapter 1.

4.1.1. STAR TRACKER MODEL

A star tracker is an optical device that measures the position of the stars and it is able to estimate the attitude by comparing them with an on-board stored catalogue. Modern star trackers output directly quaternions in the J2000 frame. The measured quaternion can be obtained as the real quaternion modified by a noise quaternion (Trawny and Roumeliotis, 2005):

$$ {}^{\mathrm{L}}_{\mathrm{J}}\tilde{\mathbf{q}} = \delta\mathbf{q}^{-1} \otimes {}^{\mathrm{L}}_{\mathrm{J}}\mathbf{q} \tag{4.1} $$

where the noise quaternion $\delta\mathbf{q}$ is approximated via small-angle rotation vector as:

$$ \delta\mathbf{q} = \begin{pmatrix} \theta_x/2 \\ \theta_y/2 \\ \theta_z/2 \\ 1 \end{pmatrix} \tag{4.2} $$

In this case, it is interesting to obtain the measured quaternion $\tilde{\mathbf{q}}$ in the neoS frame to better visualize the attitude with respect to the Sun-NEO system. The sequence followed to do this will be: first the measured quaternion in the local frame (star tracker head frame) expressed in the J2000 is converted to the BF frame expressed also in the J2000 and second, the quaternion is transformed from the J2000 to the neoS frame. Mathematically this is seen as:

$$ {}^{\mathrm{BF}}_{\mathrm{neoS}}\tilde{\mathbf{q}} = \left({}^{\mathrm{BF}}_{\mathrm{L}}\tilde{\mathbf{q}} \otimes {}^{\mathrm{L}}_{\mathrm{J}}\tilde{\mathbf{q}}\right) \otimes {}^{\mathrm{J}}_{\mathrm{neoS}}\tilde{\mathbf{q}} \tag{4.3} $$

where the DCM transforming from J2000 to neoS comes directly from the NEO orbit determination obtained in the translational navigation and the DCM transforming from the local sensor frame to the BF frame is given in Appendix B.

Although, the spacecraft counts with three star tracker heads Appendix B, only an averaged one is used for the simulations (i.e, resultant of the three). This "averaged artificial" star tracker head assumes that a 4th head is located in the same origin as the other three, but the orientation of the camera is aligned with the BFF frame. This is boresight axis aligned with BFF z-axis, and off boresight axes aligned with BFF $x-y$ axes. Note that however, this represents the worst-case scenario, as it is possible to reduce the measurement errors with multiple star trackers (Bae et al., 2010). Due to the location of the star tracker heads, for the observation phase, no obstruction of the sensor field of view is produced. This is because all three are located in the spacecraft face that points to the NEO, so there is no Sun light blinding the sensor, and each of the heads points away from the NEO. Also the redundancy of the heads makes difficult to encounter a situation in which all three are obstructed.

Mathematically, Equation (4.3) can be reduced to:

$$\overset{\text{BF}}{\text{neoS}}\tilde{\mathbf{q}} = \overset{\text{BF}}{\text{J}}\tilde{\mathbf{q}} \otimes \overset{\text{J}}{\text{neoS}}\tilde{\mathbf{q}} \tag{4.4}$$

For simplicity the subscripts BF/neoS are dropped out as in general, if not stated the opposite, $\mathbf{q}$ denotes always the rotation from the BFF to the neoS.

The star tracker chose for this mission is the Rigel-L[1], which is the new generation of star trackers. The noise values for the different axis are given in Table 4.1. The resultant noise is a combination of a white noise plus a bias. After every significant quaternion operation, the quaternion has been normalized.

Table 4.1: Star tracker performance parameters[1]

Rigel-L Star Tracker	
Performance Properties	**Value and units**
Relative Accuracy	X/Y <3 arcsec (1σ) Z <25 arcsec (1σ)
Bias	X/Y/ <5 arcsec (1σ) Z <3.5 arcsec (1σ)
Maximum Rate	6 deg/s
Maximum Acceleration	2.5 deg/s^2
Update Rate	1 Hz to 16 Hz

4.1.2. THRUSTERS

The propulsion system of the spacecraft counts with a primary Electric Propulsion (EP) system in charge of the orbit transfer and a secondary Chemical Propulsion System (CMP) for orbit manoeuvres and attitude control. The CMP is formed by twelve 20N monopropellant hydrazine thruster [2] located according to Appendix B.

Table 4.2: Performance parameters CMP thruster[2]

Airbus DS Monopropellant CHT-20N	
Property	**Value and Units**
Thrust range vac	7.9 to 24.6N
I_{sp} range vac	222 to 230 s
Supply pressure range	5.5 to 24 bar
Minimum impulse bit range	0.238 to 0.685 Ns

[1] Surrey: Rigel-L Star Tracker https://www.sst-us.com/downloads/datasheets/rigel--star-tracker-datasheet_v112.pdf. Accessed: 22-09-2017

[2] Airbus DS: 20N Hydrazine Thruster http://www.space-propulsion.com/spacecraft-propulsion/hydrazine-thrusters/20n-hydrazine-thruster.html. Accessed: 22-09-2017

For an interplanetary mission a typical profile for the thrust range of the chemical propulsion varies as shown in Figure 4.1. This is due to depressurization of the propellant tanks that causes the thrust level to change during the mission. It is also possible to observe that the thrust level at arrival of 2001 QC34 is about 10N. However, attitude manoeuvres are commanded during the entire mission and thus all the thrust range needs to be studied.

The level of thrust during a space mission is usually not controllable due to the complexity of designing a valve to regulate it (Wie, 1998). Then the valves are either open or closed with no intermediate values. As a consequence, force/torque requirements do not match the direct command that could be applied for the thrusters. To model this behavior, the thrust model has been modeled using Pulse-Width Pulse-Frequency (PWPF) modulator whose scheme is shown in Figure 4.2. Mathematically, this can be expressed in the time domain also as (McClelland, 1994):

$$\left(M_c^{k+1} - M_2^k\right) K_m = M_1^k + \frac{M_1^{k+1} - M_1^k}{\Delta t} T_m \tag{4.5}$$

where Δt is the PWPF sampling time. Isolating the filter output M_1^{k+1} a useful relationship can be obtained.

$$M_1^{k+1} = \left(M_c^{k+1} - M_2^k\right) K_m \frac{\Delta t}{T_m} + M_1^k \left(1 - \frac{\Delta t}{T_m}\right) \tag{4.6}$$

From Equation (4.6) and assuming steady state value (i.e, $M_1^{k+1} = M_1^k$), it is possible to obtain a value for the filter output as a function of the input command as:

$$M_1 = M_c K_m \tag{4.7}$$

This expression means that if K_m is not set sufficiently large, M_1 is not going to reach the activation value, generating a hang-off error in the control. This can be a problem when K_m is tuned to work fine for a certain range level of commands but not for others.

The PWPF is composed by a first order lag filter followed by a Schmitt trigger. A Schmitt trigger allows values in the positive and negative range. However, the vernier design of the thrusters only allows thrust in one direction (along their local z-axis), for this reason the Schmitt trigger has been substituted by a simple relay. On the one hand, the relay controls the cut-in and cut-out values (U_{on} and U_{off}) to produce a command of value U_{out}. On the other hand, the filter gain K_m and time constant T_m control the sensitivity and frequency of the pulses respectively. The verification of the implementation has been done using Figure 5-26 of Holtkamp (2014) and the results are shown in Figure 4.3. In the studied case, the parameters have been optimized following the guidelines of Krovel (2005) to optimize with respect to thruster activity. This is K_m as low as possible and T_m as large as possible. The manually tuned values are shown in Table 4.3. Values within the range are obtained through linear interpolation.

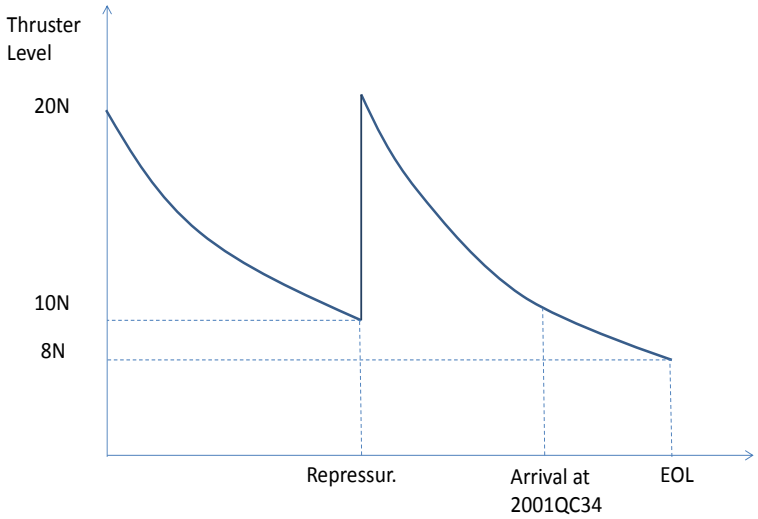

Figure 4.1: Thruster level as a function of time for CHT-20N.

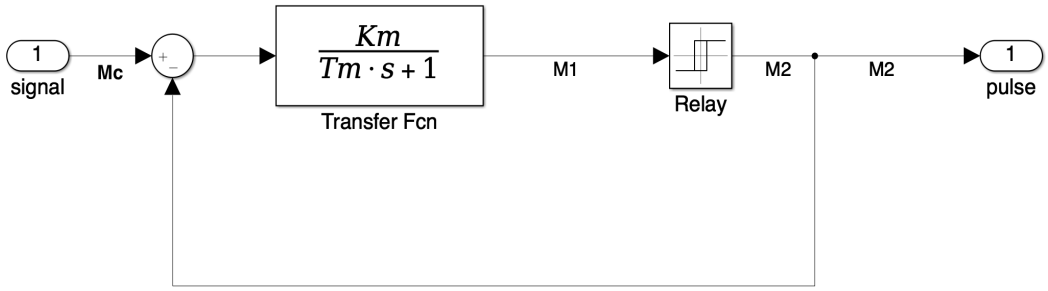

Figure 4.2: Pulse-Width Pulse-Frequency Modulator.

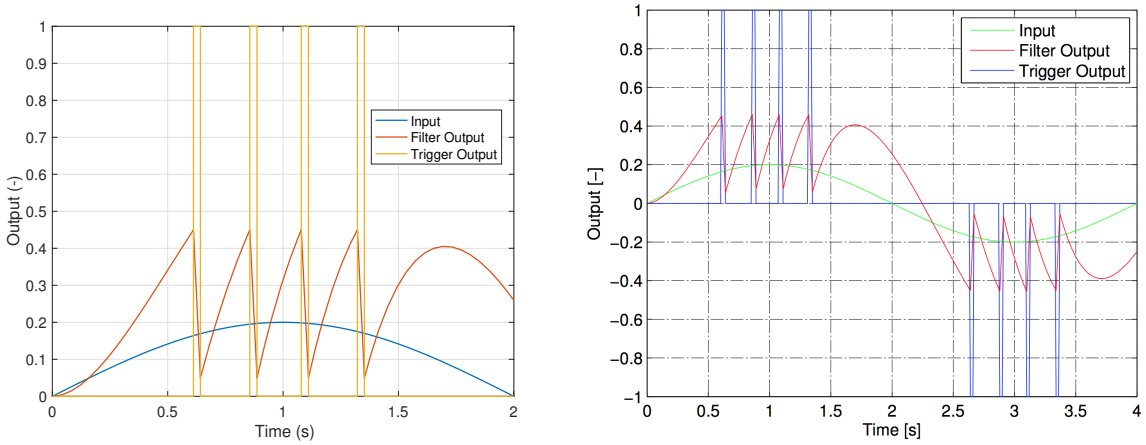

(a) Implemented PWPF modulator

(b) Figure 5-26 of Holtkamp (2014)

Figure 4.3: PWPF output comparison for a sine wave input of 0.2 amplitude.

Table 4.3: PWPF modulator parameter selection.

Parameter	Range - [24 , 7] N
K_m	[1.5 , 4.5]
T_m	[0.75 , 1.05]
U_{on}	[10.5 , 5,5]
U_{off}	[3 , 1]

Finally, the distribution matrixes relating torque and force with thrust activity are presented (Equation (4.8)). It is important to note that both rotational and translational motion are coupled. This means that although variations in velocity and angular velocity can be done independently, no torque-free force or force-free torque is allowed, which implies that translational and rotational manoeuvres need to be corrected by using the reaction wheels. This will generate significant implications for the thruster management function.

$$\begin{bmatrix} \mathbf{f} \\ \hdashline \mathbf{t} \end{bmatrix}_T = \begin{bmatrix} \mathbf{A}_f \\ \hdashline \mathbf{A}_t \end{bmatrix}_T \begin{bmatrix} CHT_1 \\ \vdots \\ CHT_{12} \end{bmatrix} \tag{4.8}$$

where

$$\mathbf{A}_f = -\left[\begin{array}{c:c:c} \mathbf{DCM}_{\text{CHT}_1} [0,0,1]^T & \cdots & \mathbf{DCM}_{\text{CHT}_{12}} [0,0,1]^T \end{array} \right] \tag{4.9}$$

and

$$\mathbf{A}_t = -\left[\ \mathbf{r}^1 \times \left(\mathbf{DCM}_{\mathrm{CHT}_1}\ [0,0,1]^T\right)\ \vdots\ \cdots\ \vdots\ \mathbf{r}^{12} \times \left(\mathbf{DCM}_{\mathrm{CHT}_{12}}\ [0,0,1]^T\right)\ \right] \tag{4.10}$$

The subscript T denotes thruster and the superscript T transpose. Now that a relationship exists between thruster activation and forces and torques, the problem that arises is how to select the correct thruster combination to perform a desired force-free torque. The responsible for this is thruster management function and typically the selection logic is based on a phase-plane system or a linear-programming (LP) technique.

The first technique consist in store all possible combinations of thrusters on board and design a switching curve to select the optimal ones. This approach it is often used for relatively simple schemes and the one used for Hayabusa mission (Kubota et al., 2006; Yamashita et al., 2001). This approach was also possible thanks to the distribution of thrusters, as both rotational and translational motion were independent.

The second technique by contrary, relies in special onboard software to solve the thruster selection problem. The thruster selection problem can be formulated as a LP optimization problem and be solved using an algorithm based on the simplex method, obtaining the corresponding firing times of each of the thrusters. One of the first examples of this use is the autopilot of the space shuttle (Bergmann et al., 1979). In Ankersen et al. (2005), the authors combine both approaches to optimize the process and precompute and store onboard a set of optimal combinations for nominal flight operations and develop a modification of the parametric simplex method to act for "off-nominal" real-time computations. This approach seeks to solve two typical problems that appear when using LP solvers: the number of iterations is unknown and thus the required computational time might be unpredictable and the solution becomes unstable when the input exceed the controllability envelope.

In this section, an alternative approach to the above mentioned algorithms that seeks to solve both problems is proposed. First, the proposed solution makes use of machine learning algorithms to do the torque distribution per thruster. This is a different approach with respect to the LP, as the solution is not the firing times per thruster, but the distributed torque per thruster. To do this, a Deep Neural Network (DNN) has been created using Keras [3] API with TensorFlow (Abadi *et al.*, 2015) as a backend. The fact of using a DNN automatically solves the problem related with computational time as the number of operations are always the same once the network is trained. Second, the PWPF modulator limits the output torque to adapt it to the physical constraints, which a priori solves the second problem related with instability due to controllability constraints. This problem is further discussed in this section.

The input consists of $[\hat{\boldsymbol{\tau}}, \hat{f}]$ where $\hat{\boldsymbol{\tau}}$ is the commanded normalized torque and $\hat{f}$ the thruster normalized force. The output is form by the resultant thrust distribution that ensures the commanded torque $[\boldsymbol{C\hat{H}T}]$. The value used for normalization has been 40 Nm for the torque and 24.6 N for the force. The architecture is shown in Figure 4.4, consisting of 4 input variables, 4 hidden layers of 48 neurons each and 12 output variables.

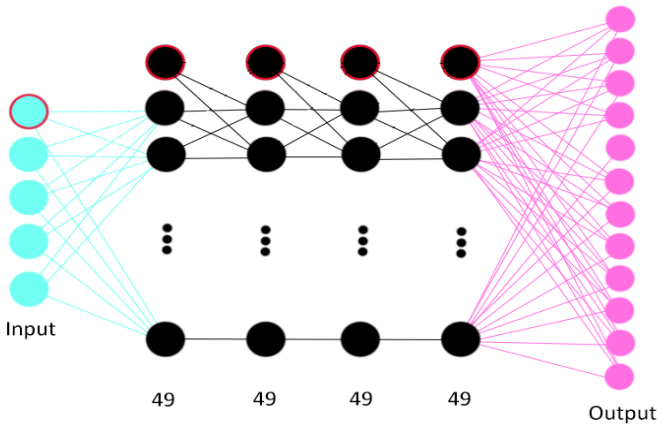

Figure 4.4: DNN architecture. Encircled red neurons represent the bias of the network.

[3] Keras: Chollet, François and others. 2015. Github: https://github.com/fchollet/keras

Rectified linear unit (ReLu) have been used for both hidden layers and output layer. This activation function is preferred over classical sigmoid as they do not saturate (avoiding the vanishing gradient problem) and they introduce sparsity in the representation which seems to be more beneficial that dense models (Glorot et al., 2011). Sensitivity analysis was done to select the number of hidden layers and number of neurons per layer, showing what many references point out (e.g. Sánchez-Sánchez and Izzo (2016)) that the deeper the network the better the model fits algorithms.

The training data has been generated using *MATLAB linprog* function that by default uses a dual-simplex optimization algorithm to solve the LP problem. A data set of 1.2 million pairs of input-output within the controllability envelope (Figures 4.5 and 4.6) for different thrust ranges has been generated for training the network. A clear conclusion from the observation of Figure 4.5 is that because of the current disposition of the thrusters, the torque along the BFF y-axis (T_y) is more limited than along the others. It is precisely along this axis where the main torque is actuating (SRP torque), however, this magnitude is very small. Figure 4.6 shows the 3D controllability envelope for illustration purposes.

Among the 1.2 million data set, 1 million has been used for training whereas the rest has been part of the validation data. The data set has been shuffled to improve the convergence. Adam (Kingma and Ba, 2014) with a batch size of 32 is used for training the network as it is the one recommended to try first by many authors due to its overall performance (Ruder, 2016). The batch size is chosen according to Keskar et al. (2016) that points out that when using stochastic gradient descent or one of its variants like Adam a larger batch degrades the quality of the model. The convergence history is shown in Figure 4.7, mean squared error has been used for computing the loss at each epoch. The obtained mean squared error for the validation data is 0.000760514, which is almost equal to the one obtained in the training set Figure 4.7, confirming that the network has been able to learn the algorithm.

A example of the predicted value vs *linprog* algorithm can be found in Figures 4.8 and 4.9. In these plots, it is possible to observe that the predicted value is very close to the obtained through *linprog* algorithm for

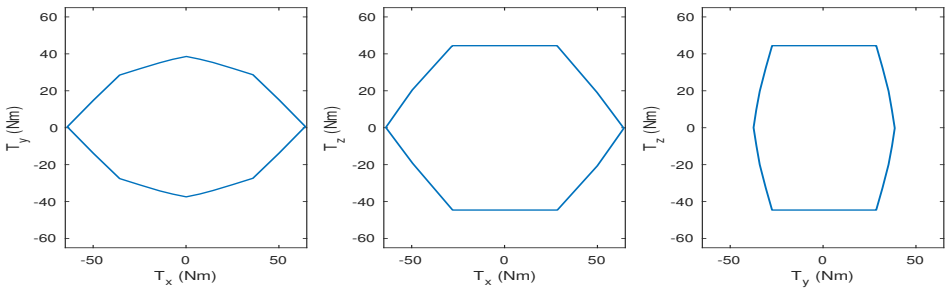

Figure 4.5: Projections of the torque controllability envelope for a thrust level of 20N.

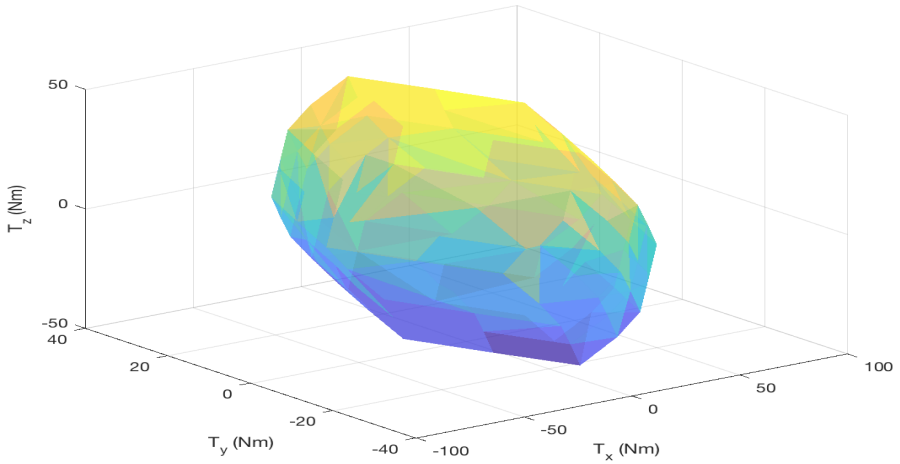

Figure 4.6: Torque controllability envelope for a thrust level of 20N.

each of the thrust levels Figure 4.8 (except thruster no. 10 that the margin is wider). However, when the thrust levels are converted to the resultant force and torque the results become more accurate being almost identical Figure 4.9.

The network is also able to predict accurately new data outside the training set if the allowable force range is increased accordingly. For example for a commanded set torque within the range:

$$\boldsymbol{\tau} = [-60, -40] \cup [60, 40] \tag{4.11}$$

MATLAB linprog is not able to provide a solution until the upper boundary is set to 70 N. Introducing this value into the DNN a mean error value of $[2.57, 1.32, 3.72]\%$ is obtained for $[\tau_x, \tau_y, \tau_z]$, showing that the network has been able to learn the algorithm behind it.

However, this method also suffers from the problem described in Ankersen et al. (2005) for LP algorithms, that when a infeasible input is commanded (outside the controllability envelope), the algorithm returns a solution in the opposite direction as the desired one. A simple solution to this problem could be to train the NN with a data set generated without setting any upper boundary in the *linprog* algorithm (i.e ub = $+\infty$). In this case, the network would be able to output a correct solution in the desired direction no matter if the input is feasible or not. After, the solution is passed through the PWPF modulator to adapt it to the physical constraints.

In our case, the resolution obtained is more than enough as the unloaded torque remains within the controllability envelope. Only in the case when the thrust level is below ~ 10 the *linprog* algorithm is not able to output a feasible solution but the DNN is robust enough to output solutions in the same direction as desired.

The main advantage of the DNN with respect to *MATLAB linprog* is the improvement in computational time, being about ~ 120 times faster the former. As a comparison for 1000 simulations, *MATLAB linprog* takes an average of 9.8 ms per case whereas the DNN 0.08 ms. Furthermore, it is very easy to implement it

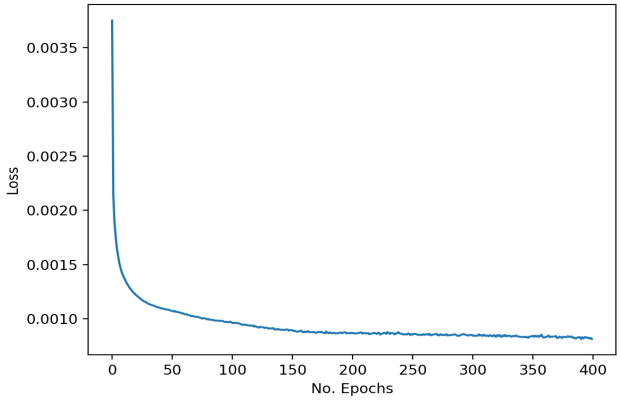

Figure 4.7: DNN convergence history.

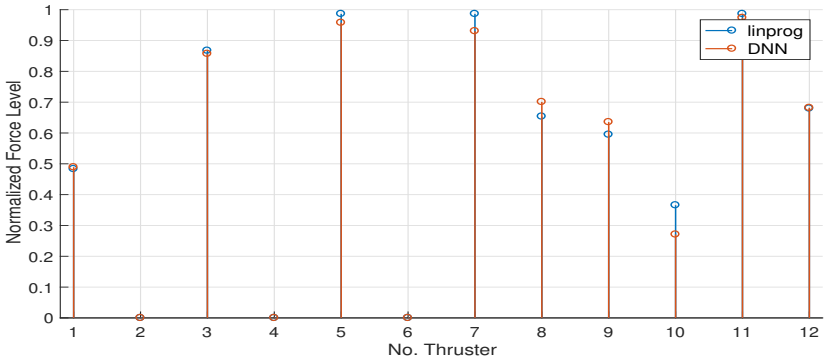

Figure 4.8: Thruster level comparison example between the DNN and *linprog* algorithm.

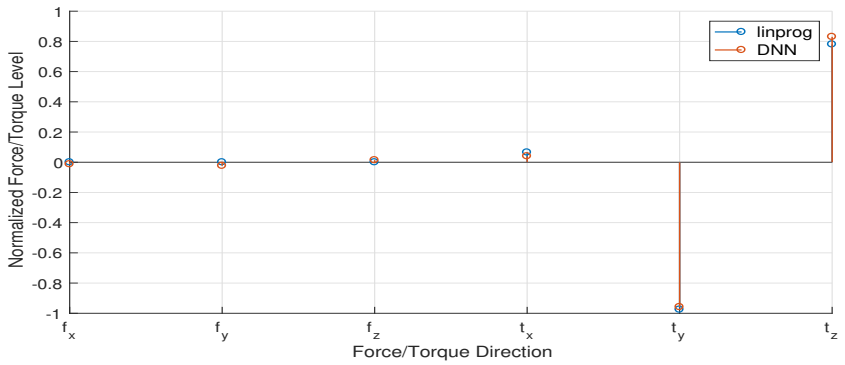

Figure 4.9: Resultant force and torque comparison example between the DNN and *linprog* algorithm.

onboard as the ReLu is nothing but a saturation function and only the matrices with weights and bias need to be previously stored. The only problem arises due to the PWPF modulator and the hang-off error associated, that can cause large errors if the gains are not properly tuned.

Finally, the translational thruster activity also plays a major role in the attitude response due to two reasons. First, the motion is coupled so the wheels need to correct the attitude at each manoeuvre. Second, usually the desired commanded thrust differs from the actual one in terms of magnitude. This is if a commanded thrust is applied of 20 N the real response of the system will be an oscillating value around the commanded one. To deal with these uncertainties, a random white noise of 2 Nm is introduced into the system for a period of 1 s, which is more or less the amount of time needed to command a ΔV of a couple cm/s.

4.1.3. REACTION WHEELS

The reaction wheels performance parameters and physical properties are summarized in Figures 4.10 and 4.11, for complete information refer to the website [4]. A redundant configuration forming a pyramid shape is used for controlling the attitude of the spacecraft. Information about is location can be found in Appendix B.

Table 4.4: Reaction Wheels performance parameters[4]

Rockwell-Collins RSI 12	
Performance Properties	**Value and units**
Angular Momentum at Nominal Speed	12 Nms
Operational Speed Range	± 6000 rpm
Speed Limiter	<7500 rpm
Motor Torque at Nominal Speed	75 mNm
Loss Torque (max)	<20 mNm

The nominal initial speed of the wheels has been chosen aligned with the BFF x-axis (Equation (4.12)). The motivation for this, resides in the fact that although the hovering arcs are usually symmetric, the mean motion of the spacecraft around the Sun makes that the spacecraft attitude rotates also on average the same magnitude. This rotation is done around the x-axis and the speeds have been chosen so that they get always load avoiding zero-crossings. However, as it will be discussed in the results, this is not the optimal choice. The capabilities for the motor torque have been assumed to be constant during all the operation range, this implies a maximum supplied motor torque equal to 75 mNm.

[4] RSI 12 Momentum and Reaction Wheels https://www.rockwellcollins.com/Products_and_Services/Defense/Platforms/Space/RSI_12_Momentum_and_Reaction_Wheels.aspx. Accessed: 22-09-2017

Table 4.5: Reaction Wheels physical specs[4].

Rockwell-Collins RSI 12	
Dimensions	**Value and units**
Diameter	12 Nms
Height	± 6000 rpm
Mass	<7500 rpm

$$\boldsymbol{\omega}_0 = [-325, -325, 325, 325] \quad \text{rad/s} \tag{4.12}$$

As mentioned in Section 2.3.2, the momentum torque that the spacecraft experiences due to the reaction wheels is opposed to the variation in angular momentum of the wheels $\boldsymbol{\tau} = -\dot{\boldsymbol{h}}_{\boldsymbol{\omega}}$. The wheel momentum vector is written as (Bayard, 2010):

$$\mathbf{h}_\omega = \sum_{i=1}^{N} \mathbf{a}_i I_{si} \omega_{si} = \mathbf{A}\mathbf{I}_s \boldsymbol{\omega}_s \tag{4.13}$$

where $\mathbf{a}_i$ are unit vectors along each reaction wheel spin axis, $\mathbf{A}$ the distribution matrix, I_{si} the scalar reaction wheel inertia, ω_{si} the scalar angular velocity of the wheel and N the total number of wheels. To obtain the variation in angular momentum over time, the rate of change of the angular velocity is taken which gives:

$$\boldsymbol{\tau} = -\dot{\boldsymbol{h}}_{\boldsymbol{\omega}} = -\mathbf{A}\mathbf{I}_s \dot{\boldsymbol{\omega}}_s \tag{4.14}$$

The distribution of the torque along the individual wheels is done through the pseudoinverse method (Markley and Crassidis, 2014). Denoting $\mathbf{A}_\omega = \mathbf{A}\mathbf{I}_s$, the pseudoinverse is defined as:

$$\mathbf{A}_\omega^+ = \mathbf{A}_\omega^T \left(\mathbf{A}_\omega \mathbf{A}_\omega^T\right)^{-1} \tag{4.15}$$

then

$$\dot{\boldsymbol{\omega}}_s = -\mathbf{A}_\omega^+ \boldsymbol{\tau} \tag{4.16}$$

The reaction wheels are typically assembled in a housing containing the rotation flywheel suspended on bearings and being controlled by an internal brushless DC motor (Bayard, 2010). This causes several disturbances to appear that have to be taken into account for reduce the pointing error. In this study, only disturbances generated by bearing friction are considered. This includes viscous and Coulomb friction whose expressions are given here and showed in Figure 4.10.

Coulomb friction (Bayard (2010)):

$$\mathbf{t}^C = -C^C \text{sign}(\boldsymbol{\omega}_s) \tag{4.17}$$

Viscous friction:

$$\mathbf{t}^V = -C^V \text{sign}(\boldsymbol{\omega}_s) \boldsymbol{\omega}_s^{2/3} \tag{4.18}$$

where $C^C = 0.005$ N m and $C^V = 0.0002$ N m rad$^{2/3}$ s$^{-2/3}$. The coefficients together with Equation (4.18) have been obtained fitting experimental data (Delchambre, 2017b).

The line-of-sight pointing error due to this two disturbances is given by (Bayard, 2010):

$$\mathbf{e}_{\text{friction}} = (\mathbf{J} k_q)^{-1} \left(\mathbf{t}^C + \mathbf{t}^V\right) \tag{4.19}$$

where k_q is the proportional gain.

The friction torque induced by the reaction wheels it is known to be sensitive to external factors (temperature), non-symmetric for positive and negative velocities and different for each of the wheels. To reduce the last two effects, the supplier recommends to speed up the wheels during a certain amount of hours prior lunch in both directions. Even so, some asymmetries and uncertainties with respect to the real model persist. To overcome these problems for precise pointing, it is recommended to design a local PI controller based on tachometer feedback in each of the wheels instead of direct feedforward (Bayard, 2010). For this research, a velocity feedback considering a perfect observer has been implemented. However, this model only considers

the small delay that appears until the current angular velocity reach its commanded one (Figure 4.12). Figure 4.12 shows this effect comparing the commanded angular velocity with the current angular velocity using a local PI and the current angular velocity without using a local PI. This limitation was due to lack of time and also due to the fact that the complete simulation slows down until a point in which simulation times of a couple of days are not feasible with the desired integration time. Figure 4.11 show this model, however for a more accurate representation please refer to Cocci (2016); Carrara and Kuga (2013).

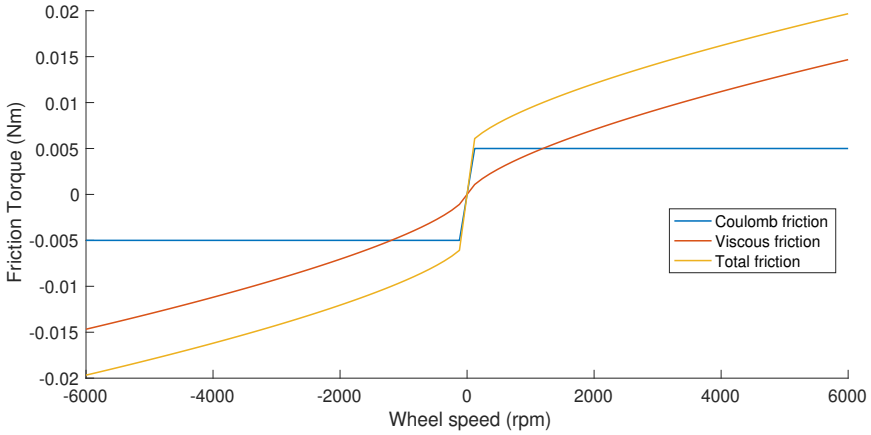

Figure 4.10: Disturbances generated by viscous and Coulomb friction in a single wheel as a function of the angular velocity.

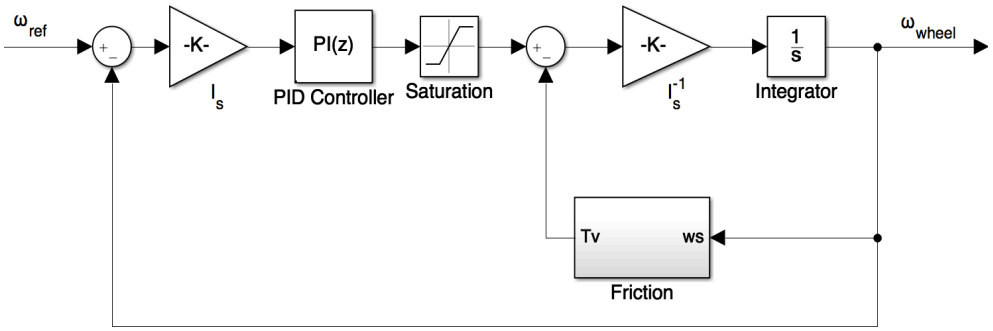

Figure 4.11: Local PI velocity feedback assuming perfect observer.

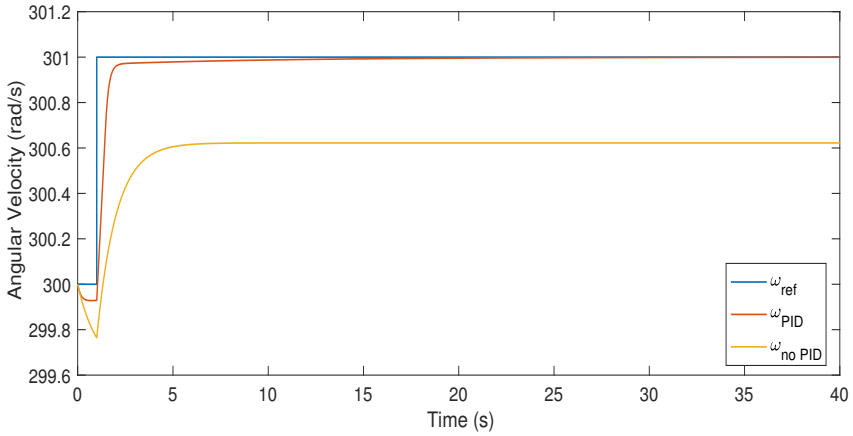

Figure 4.12: Angular velocity response to a commanded one.

REACTION WHEELS UNLOADING

As mentioned in Section 4.1.2, the CHT-20N thrusters are used for momentum unloading. The main challenge to do this reside in the fact that both translational and rotational motion are coupled, and thus the activation of the thrusters have to follow a certain sequence.

The method followed to unload the wheels has been to wait until the four of them become saturated and then command a torque in the opposite direction of the angular momentum vector of the wheels. This is:

$$\boldsymbol{\tau}_{\text{unload}} = K_{\text{unload}} \left(\mathbf{h}_{\omega,\text{ref}} - \mathbf{h}_{\omega} \right) \tag{4.20}$$

where K_{unload} is an interpolated value between 0.85 and 0.2 s^{-1} for CHT thrust levels of 24 N and 7 N respectively, that have been obtained through manual tuning. Note that this case represents the most critical one, as it is the time in which more momentum needs to be unloaded and thus, more disturbances in the translational motion are introduced.

When the unloading manoeuvre is commanded, $\mathbf{h}_{\omega}$ starts decreasing and thus $\boldsymbol{\tau}_{\text{unload}}$ does it too. This makes that at some point the distributed thruster force M_c due to the unloaded torque $\boldsymbol{\tau}_{\text{unload}}$ does not reach the activation of the thruster and thus a hang-off error appears due to the PWPF modulator. In Figure 4.13, this effect is seen with the final achieved angular speed of the wheels which is far from the reference value established. Analysing thruster number 7 (Figure 4.14), which is in this case involved in the unloading, it is seen that after two manoeuvres, the steady-state value after the filter (M_1) does not reach U_{on}. Mathematically, this value is given by the following expression as seen before.

$$M_1 = M_c K_m \tag{4.21}$$

where M_c is the distributed force in a particular thruster from the desired total torque $\boldsymbol{\tau}_{\text{unload}}$. To overcome this problem, if $\mathbf{h}_{\omega}$ is updated at every iteration, then K_{unload} has to be increased proportionally.

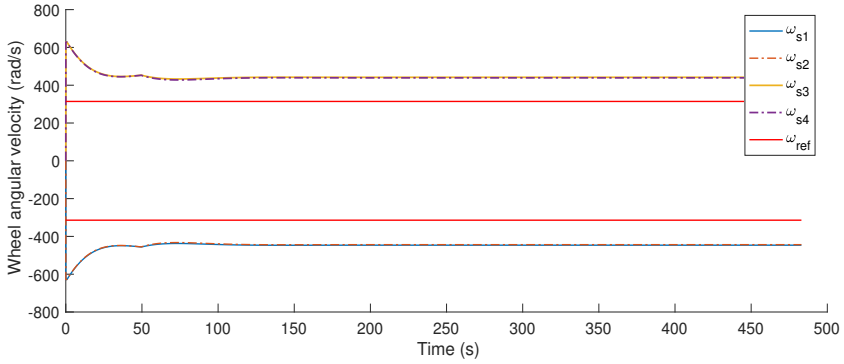

Figure 4.13: Evolution of the angular velocity of the reaction wheels during a momentum dumping manoeuvre assuming perfect behaviour (i.e, no torque limit and no friction torque) with variable $\boldsymbol{\tau}_{\text{unload}}$.

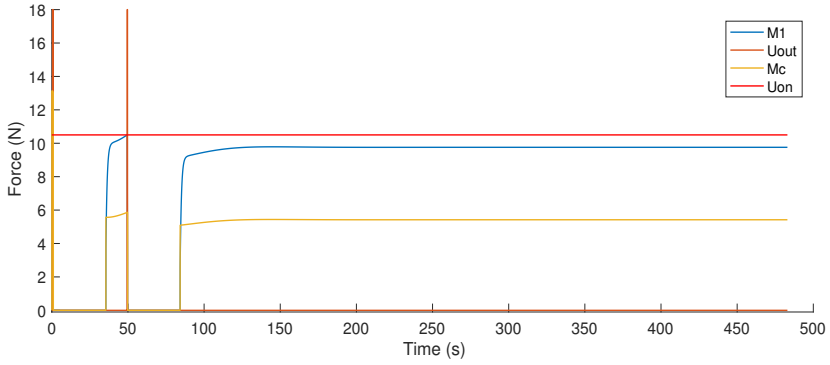

Figure 4.14: PWPF modulator corresponding to thruster CHT-7 for a momentum dumping manoeuvre with variable $\boldsymbol{\tau}_{\text{unload}}$ for $K_m = 1.8$, $T_m = 0.85$, $U_{\text{out}} = 18$, $U_{\text{on}} = 10.5$ and $U_{\text{off}} = 3$.

Another potential solution and the one adopted is to fix the value for $\boldsymbol{\tau}_{\text{unload}}$ (i.e. $\mathbf{h}_\omega$ fixed), when the unloading is commanded. Analysing Figure 4.15, it is seen that M_c remains constant during the thrusting activation, without decreasing its value at each command. This makes that the pulse duration of the thruster is always the same (i.e, the same torque is applied at each command). With this strategy, the algorithm stops once the reference velocity has been reached Figure 4.16, and in this way it is ensured that the wheel speed is at least below the margin established. For the analysis in Figures 4.13 to 4.16, perfect behaviour of the wheels (i.e, no torque limit and no friction torque) has been assumed, and a thruster level of 18 N. Note that in this ideal scenario, the gains of the PWPF modulator have not been chosen as explained before, because that choice was done based on the real scenario.

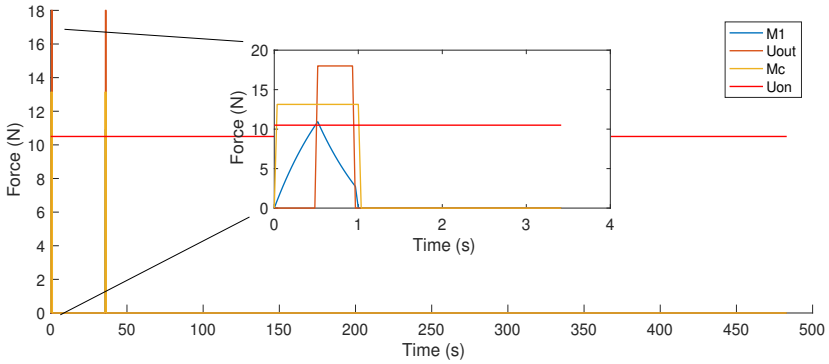

Figure 4.15: PWPF modulator corresponding to thruster CHT-7 for a momentum dumping manoeuvre for a fixed $\boldsymbol{\tau}_{\text{unload}}$ for $K_m = 1.8$, $T_m = 0.85$, $U_{\text{out}} = 18$, $U_{\text{on}} = 10.5$ and $U_{\text{off}} = 3$.

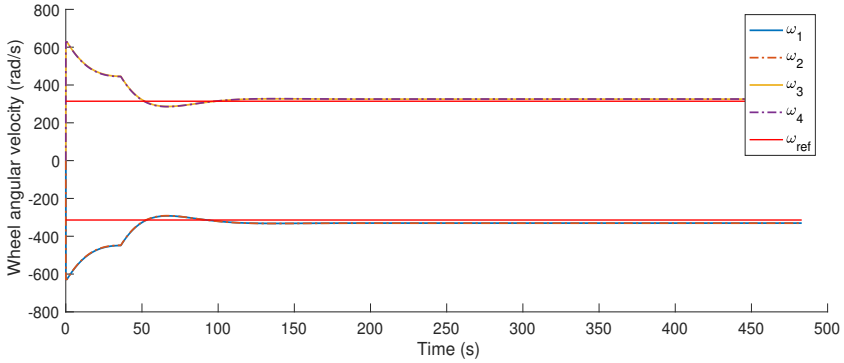

Figure 4.16: Evolution of the angular velocity of the reaction wheels during a momentum dumping manoeuvre assuming perfect behaviour (i.e, no torque limit and no friction torque) for a fixed $\boldsymbol{\tau}_{\text{unload}}$.

4.2. GUIDANCE

The purpose of the mission is to observe the asteroid as accurate as possible, so that the monocamera is able to obtain the absolute state of the spacecraft. For that, the spacecraft shall be able to point directly to the asteroid with a zero-relative angular velocity. The neoS has been used as a reference frame, as it provides information about the two main bodies (Sun and NEO).

To achieve the desired attitude, a guidance law is designed as follows:

- The information coming from the translational EKF (Section 3.2) is obtained with an update rate of 60 s, which provides information about the position of the spacecraft.
- The BFF z-axis ($\hat{z}_{\text{ref}}$), which coincides with the camera LoS, is aligned with the unitary vector from the spacecraft center of mass to the asteroid center of mass.
- The BFF y-axis ($\hat{y}_{\text{ref}}$) is aligned with the resultant unitary vector obtained from the cross product between the BFF z-axis and the estimated angular momentum of the NEO orbit ($\hat{\boldsymbol{h}}_{\text{NEO}}$).

- The BFF x-axis ($\hat{x}_{\text{ref}}$) completes the right hand system.

A DCM containing this information is assembled and converted to the reference quaternion $\hat{\mathbf{q}}_{\text{ref}}$. The reference angular velocity ($\boldsymbol{\omega}_{\text{ref}}$) is set to zero. The following Simulink scheme shows the implementation:

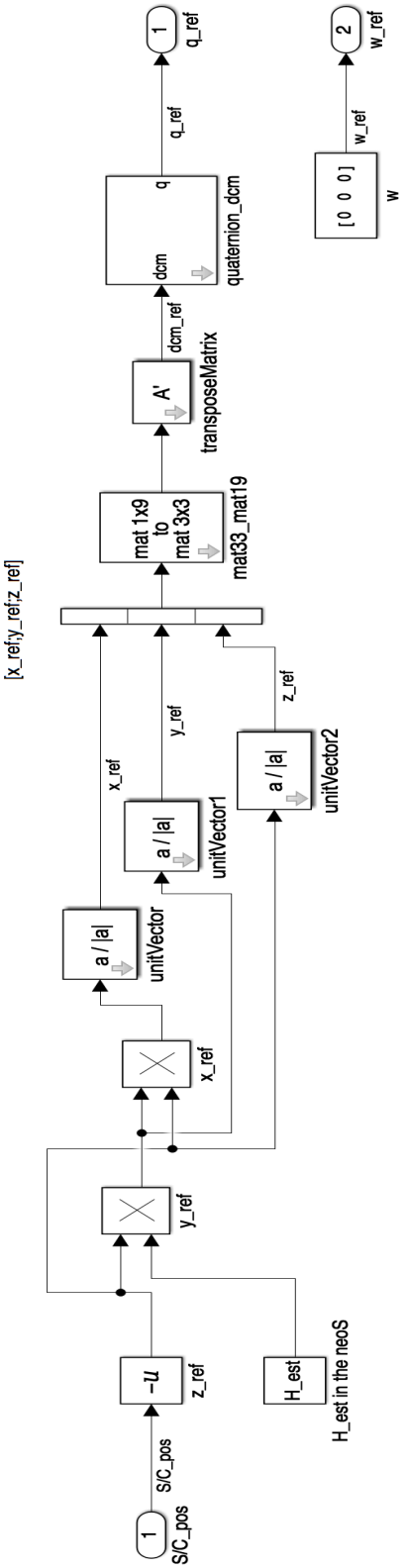

Figure 4.17: Simulink guidance scheme.

4.3. NAVIGATION

The objective of the navigation system is to be able to estimate the attitude and angular velocity with enough accuracy so that the spacecraft can achieve the desired pointing performance with the only use of star tracker information. To estimate rotational state of the spacecraft with gyroless information two approaches can be followed (Bar-Itzhack, 2001). The first one is to compute the derivative numerically from the measured quaternion and then filter the noise introduced when doing this mathematical operation to obtain the filtered angular velocity. The noise introduced into the system can be filtered either using a low pass filter or an adapted Kalman Filter (KF) Bar-Itzhack et al. (2006). Figure 4.18 shows schematically this procedure. The second approach is to estimate the angular velocity directly from the kinematics equation without any differentiation (Oshman and Markley, 1999).

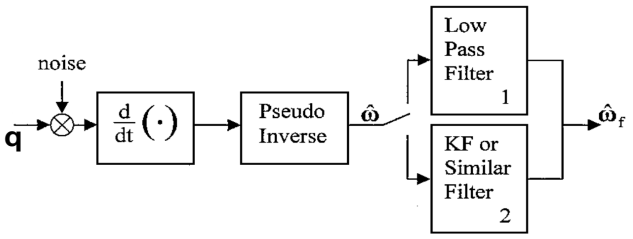

Figure 4.18: Block-diagramrepresentation of the derivative approach (Bar-Itzhack (2001)).

However, when using a KF, the dynamics of the spacecraft needs to be modeled. This can be done either including the full dynamics (Equation (2.31)) or approximating the angular velocity to a Markov first order model (Bar-Itzhack et al., 2006). A Markov model is a stochastic model that models random processes based only on the current information (not previous events). This property makes that if the update rate of the information is high enough, good performance can be achieved with this model. This approach can also be used to model instead of directly the angular velocity, the bias of it (Challa, 2017). This is:

$$\dot{\boldsymbol{\omega}} = -\frac{\boldsymbol{\omega}}{\tau} + \boldsymbol{\eta}_\omega \qquad \text{or} \qquad \dot{\boldsymbol{b}} = -\frac{\boldsymbol{b}}{\tau} + \boldsymbol{\eta}_b \tag{4.22}$$

where τ is a time constant, $\boldsymbol{\eta}_\omega$ and $\boldsymbol{\eta}_b$ are zero-mean white noise. When the bias $\boldsymbol{b}$ is used instead of directly the angular velocity, the angular velocity is computed as:

$$\boldsymbol{\omega} = \boldsymbol{\omega}_{\text{true}} + \boldsymbol{b} + \boldsymbol{\eta}_\omega \tag{4.23}$$

Furthermore, the commanded control $\mathbf{u}$ can also be included into the filter to increase the performance (Azor et al., 2001).

The approach followed in this thesis is the derivative approach with the inclusion of a low pass filter to attenuate the noise. The pseudo-linear Kalman Filter (PSELIKA) introduced in Bar-Itzhack et al. (2006) was tested without offering significant improvement and it was less robust when modifying the frequency sample of the star tracker. For that reason, it was discarded.

To obtain the angular velocity from the measured quaternion the numerical approach described in Trawny and Roumeliotis (2005) is followed:

$$\hat{\boldsymbol{\omega}} = \lim_{\Delta t \to 0} \frac{\delta\boldsymbol{\theta}}{\Delta t} \tag{4.24}$$

where

$$\delta\boldsymbol{\theta} = 2\hat{\mathbf{q}}^{-1}_{t+\Delta t} \otimes \hat{\mathbf{q}}_t \tag{4.25}$$

When performing the derivative, the noise contained in $\delta\boldsymbol{\theta}$ is also propagated. To obtain how the noise is propagated, the central limit theorem is used (Fab Labs Central). If two random variables x_1 and x_2 are added, the probability distribution of the sum y is given by the convolution of the two variables as:

$$P(y) \triangleq P_1(x) * P_2(x) = \int_{-\infty}^{\infty} P_1(x) P_2(y-x)\, dx \tag{4.26}$$

In this case, when doing $\delta\boldsymbol{\theta}$, the noises $\boldsymbol{\gamma}_{\theta 1}$ and $\boldsymbol{\gamma}_{\theta 2}$ are subtracted, being thus the probability distribution of $P_{\gamma_{\theta 1}-\gamma_{\theta 2}}(\eta)$, the convolution of $\boldsymbol{\gamma}_{\theta 2}$ and $-\boldsymbol{\gamma}_{\theta 1}$:

$$P_{\gamma_{\theta 1}-\gamma_{\theta 2}}(\gamma) = \int_{-\infty}^{\infty} \Gamma(-\gamma')\Gamma(\gamma-\gamma')d\gamma' \tag{4.27}$$

If the noise is distributed as a Gaussian noise with standard deviation σ, then:

$$\Gamma(\gamma) = \frac{1}{\sqrt{2\pi}\sigma}\exp\left(\frac{-\gamma^2}{2\sigma^2}\right) \tag{4.28}$$

and doing the integral, the probability has the form:

$$P_{\gamma_{\theta 1}-\gamma_{\theta 2}}(\gamma) = \frac{1}{\sqrt{2\pi}\left(\sqrt{2}\sigma\right)}\exp\left(\frac{-\gamma^2}{2\left(\sqrt{2}\sigma\right)^2}\right) \tag{4.29}$$

which is a Gaussian distribution with standard deviation $\sqrt{2}\sigma$. Dividing this value by Δt, the noise is propagated as $\sqrt{2}\sigma/\Delta t$. This means that for example a noise with a standard deviation of 25 arcseconds and sample frequency of 16 Hz in the BFF z-axis is propagated to an angular velocity in the same axis with a standard deviation noise of $25\sqrt{2}$ arcseconds $/(1/16)$. This analytic result is very useful for validation purposes.

It is important to note that for the mentioned sampled frequency, the amplitude of the noise is amplified by a factor of ~ 20 ($16\sqrt{2}$), being thus necessary to filter the signal to improve the performance. The selected low pass filter for doing this has been a Butterworth 1st order discrete filter with a frequency bandwidth (B_w) of 0.02 Hz for a data sampled with a 16 Hz rate. The Butterworth type filter has been selected for being designed to have as flat a frequency response as possible in the passband. This physically means that the estimated angular velocity signal will only be modified from the cut-off frequency onwards. The reasoning for choosing the bandwidth value is that it is desired to filter as much high-frequency as possible being able to still track the changes in the guidance quaternion. The settling time of the filter ($4/B_w$) is ~ 30 s which is half of the updating rate of the reference quaternion. The following figure shows the effects of applying the filter to the numerically computed angular velocity. It is clear comparing the estimated angular velocity $\hat{\boldsymbol{\omega}}$ and the one after the filter is applied $\hat{\boldsymbol{\omega}}_f$ that the noise decays for frequencies higher than 0.02 Hz, reaching a noise values similar to the estimated quaternion.

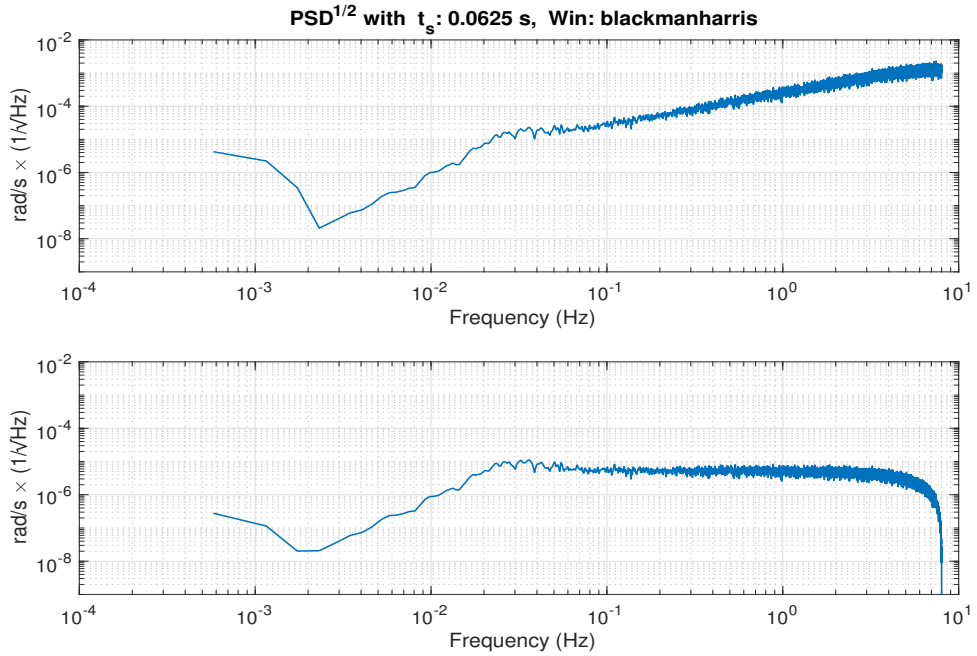

Figure 4.19: Standard root PSD comparison between $\hat{\boldsymbol{\omega}}$ and $\hat{\boldsymbol{\omega}}_f$ along the BFF z-axis ($\sigma = 25$ arcseconds).

4.4. CONTROL

The objective of the control algorithm is to be robust to the uncertainties that the system will face for an interplanetary mission. Although there are more complicated algorithms such as H-infinity (H_∞) control, the typical first approach is to start by Proportional-Derivative (PD) due to its simplicity. A PD with only feedforward compensation of the gyroscopic terms has been chosen for this study. The fact of not including an integrator will provoke that the spacecraft will only be able to track asymptotically a step command which represents a loss of capabilities with respect the PID which is also able to track asymptotically a ramp. However, the inclusion of an integrator introduces problems when large manoeuvres are performed or when the reaction wheels become saturated due to integrator windup (Bayard, 2010). The PD controller in the body-fixed frame has the following form:

$$\boldsymbol{\tau} = \hat{\boldsymbol{\omega}} \times (\mathbf{J}\hat{\boldsymbol{\omega}} + \mathbf{h}_\omega) - \mathbf{K}_q \mathbf{q}_{\text{error}} - \mathbf{K}_\omega \boldsymbol{\omega}_{\text{error}} \tag{4.30}$$

where $\mathbf{q}_{\text{error}} = \boldsymbol{\omega}_{\text{ref}}^{-1} \otimes \hat{\mathbf{q}}$ and $\boldsymbol{\omega}_{\text{error}} = \boldsymbol{\omega}_{\text{ref}} - \hat{\boldsymbol{\omega}}$. For stability the gains are chosen to be $\mathbf{K}_q = \mathbf{J}k_q$ and $\mathbf{K}_\omega = \mathbf{J}k_\omega$. The selection of the gains will be done in Section 4.5 so that the system remains stable.

Finally, instead of denoting the inertia matrix by $\mathbf{J}$ a more correct way would be to express it like $\hat{\boldsymbol{J}}$. The difference between the real inertia $\mathbf{J}$ and the inertia model $\hat{\mathbf{J}}$ resides in the fact that $\hat{\mathbf{J}}$ is kept constant with value found in Appendix B, whereas $\mathbf{J}$ changes during time due to sloshing, position of the solar panels, etc. To model this, at each simulation the inertia matrix used for propagation is randomly modified varying its diagonal elements a 10% and a 20% the cross-diagonal ones. The inclusion of this effect into the simulation introduces a bias equal to $J^{-1}\left(\hat{\boldsymbol{\omega}} \times \hat{\boldsymbol{J}}\hat{\boldsymbol{\omega}} - \boldsymbol{\omega} \times \mathbf{J}\boldsymbol{\omega}\right)$. As the angular velocities are very small during hovering, this bias is negligible compared with other sources of error that will be studied in Section 4.6.

4.5. STABILITY ANALYSIS

A simplified scheme of a SISO closed-loop system is shown in Figure 4.20. The scheme includes a plant or dynamics (P), a controller (K), the sensors are included through measurement noise (m) and the system is affected by external disturbances (d). This is a linear analysis, and thus, it is only valid for small angle representations.

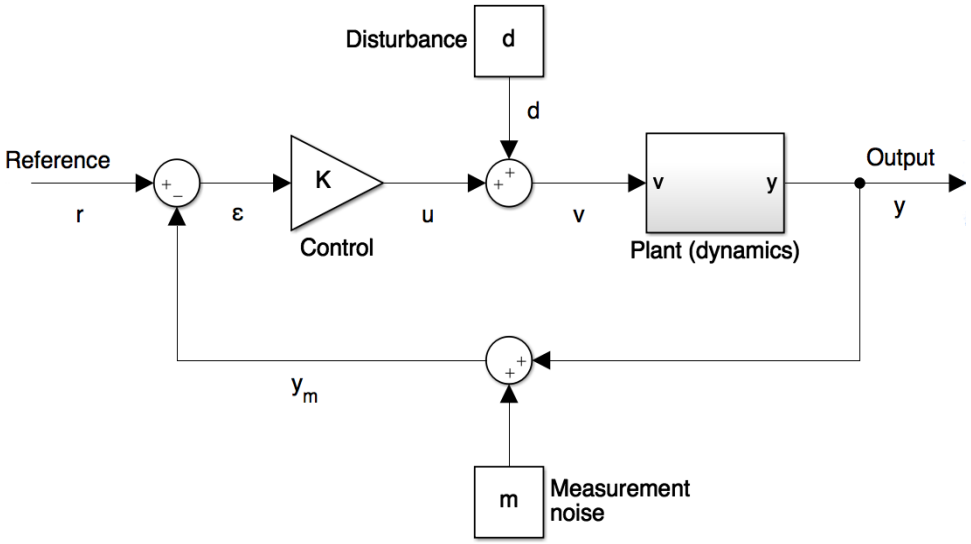

Figure 4.20: Simplified closed-loop block diagram for a controlled system

From this scheme, a couple of useful relationships for determining the bandwidth of our controller can be derived. Starting by setting up the following relationships:

$$Y(s) = P(s)(K(s)\epsilon(s) + D(s)) \tag{4.31}$$

$$\epsilon(s) = R(s) - Y_m(s) \tag{4.32}$$
$$Y_m(s) = Y(s) + M(s) \tag{4.33}$$

and rearranging the terms

$$Y(s) = P(s)(K(s)(R(s) - Y(s) - M(s)) + D(s)) \tag{4.34}$$
$$Y(s) + P(s)K(s)Y(s) = P(s)K(s)R(s) - P(s)K(s)M(s) + P(s)D(s) \tag{4.35}$$
$$(1 + P(s)K(s))^{-1}Y(s) = P(s)K(s)R(s) - P(s)K(s)M(s) + P(s)D(s) \tag{4.36}$$

finally we arrive to

$$Y(s) = T(s)R(s) - T(s)M(s) + S(s)P(s)D(s) \tag{4.37}$$

where $S(s) = (1 + P(s)K(s))^{-1}$ denotes the sensitivity function and $T(s) = (1 + P(s)K(s))^{-1}P(s)K(s)$ the complementary sensitivity. Note that the latter name is due to the following relationship:

$$S(s) + T(s) = I \tag{4.38}$$

Defining the performance error as the difference between the actual state and the desired state (ECSS, 2014):

$$\epsilon_p = Y(s) - R(s) = -S(s)R(s) - T(s)M(s) + S(s)P(s)D(s) \tag{4.39}$$

Substituting Equation (4.30) into Equation (2.30), assuming perfect knowledge of the variables, taking small angle approximation and assuming that no external disturbances are acting into the system, the system can be reduced to:

$$\dot{\boldsymbol{\omega}} = \mathbf{J}^{-1}\boldsymbol{\tau} \tag{4.40}$$

and taking the Laplace transform, the plant is expressed as:

$$P(s) = \frac{1}{s^2} \tag{4.41}$$

whereas the controller K has the form:

$$K(s) = k_p + sk_d \tag{4.42}$$

Note that k_p+k_d are equivalent to k_q and k_ω, the notation here is changed to differentiate between proportional and derivative term. With this information the expression relating the performance error with the external disturbances is:

$$\epsilon_p^d = \frac{1}{s^2 + k_d s + k_p} D(s) \tag{4.43}$$

When no feedforward term in the angular rate is commanded, the performance error due to the command slightly changes its expression with respect to Equation (4.39) (Bayard, 2010):

$$\epsilon_p^{\text{ref}} = -\frac{(s + k_d)s}{s^2 + k_d s + k_p} R(s) \tag{4.44}$$

Finally, the expression for the performance error as a function of the measurement noise is also given:

$$\epsilon_p^m = -\frac{k_d s + k_p}{s^2 + k_d s + k_p} M(s) \tag{4.45}$$

Observing Equation (4.39), one can think to design the sensitivity matrix $S(s)$ so that it has good reference tracking while high-frequency noise is attenuated. Based on the sensitivity function, the natural frequency f_0 (Hz) from the desired closed-loop bandwidth B_w (Hz) and damping ratio ξ is obtained as follows (Delchambre, 2017a):

$$f_0 = \frac{B_w}{\sqrt{-1 + 2\xi^2 + \sqrt{2}\sqrt{1 - 2\xi^2 + 2\xi^4}}} \tag{4.46}$$

Note that for a damping ratio of $1/\sqrt{2}$, $f_0 = B_w$. From the natural frequency, k_p and k_d are calculated as:

$$k_p = \omega_n^2 \qquad k_d = 2\xi\omega_n \qquad \text{where} \qquad \omega_n = 2\pi f_0 \tag{4.47}$$

To test the robustness of the system, the system in open-loop has to be studied. Figure 4.21 shows a simplified schematic for an open-loop system, which is equivalent in the Laplace domain to:

$$\frac{y(s)}{r(s)} = \exp^{-\tau s} K(s)D(s) \tag{4.48}$$

The robustness of a system is given by the stability margins, which indicate how much the system can deviate from the expected behaviour. To obtain the stability margins, first a grid search is done for a bandwidth values of 0.01 and 0.1 Hz, for different signal delays. These margins are collected in Tables 4.6 and 4.7.

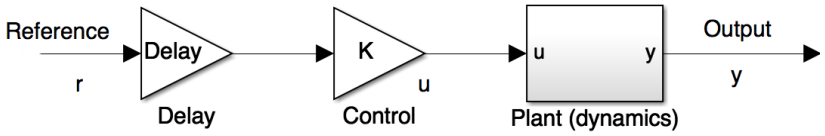

Figure 4.21: Simplified open-loop block diagram for a controlled system

Table 4.6: Stability margins with $B_w = 0.01$ Hz and $\xi = 0.7071$

Delay (s)	**Gain Margin** (dB)	**Frequency** (rad/s)	**Phase Margin** (deg)	**Delay Margin** (s)	**Frequency** (rad/s)	**Stable**
0	∞	-	65.5	11.7	0.0976	Yes
1	24.8	1.540	59.9	10.7	0.0976	Yes
2	18.6	0.756	54.3	9.7	0.0976	Yes

Table 4.7: Stability margins with $B_w = 0.1$ Hz and $\xi = 0.7071$

Delay (s)	**Gain Margin** (dB)	**Frequency** (rad/s)	**Phase Margin** (deg)	**Delay Margin** (s)	**Frequency** (rad/s)	**Stable**
0	∞	-	65.5	1.17	0.976	Yes
1	2.23	1.22	9.59	0.17	0.976	Yes
2	12.7	3.87	-46.3	-0.83	0.976	No

ECSS (2014) establishes that classical values for gain and phase margin are 6 dB and 30° respectively. Looking at Tables 4.6 and 4.7, it is possible to observe that the lower the bandwidth, the more robust the system. However, the controller shall be able to track the guidance commands that the translational navigation is sending every 60 s to the rotational control system. This imposes a lower boundary of 0.0106 Hz. Nevertheless, a bandwidth value of 0.02 Hz is defined to allow a certain margin so that the system is able to track the guidance command in ~ 30 s. With the bandwidth value selected, the values for the proportional and derivative term are:

$$k_p = 0.0158 \qquad k_d = 0.1777 \tag{4.49}$$

The stability margins for this configuration are shown in Table 4.8. It is possible to see that even for delays of the order of a couple of seconds (normally it is not the case), the gain and phase margins remain within the allowed values. Figure 4.22 show the closed-loop transfer functions relating the performance error with the different disturbance sources. It is possible to observe that the closed-loop signal is modified at the established bandwidth frequency (0.02 Hz). The results showed in this plot will also be used for the next section.

Table 4.8: Nominal stability margins- $B_w = 0.02$ Hz and $\xi = 0.7071$

Delay (s)	**Gain Margin** (dB)	**Frequency** (rad/s)	**Phase Margin** (deg)	**Delay Margin** (s)	**Frequency** (rad/s)	**Stable**
0	∞	-	65.5	5.86	0.195	Yes
1	18.6	1.51	54.3	4.86	0.195	Yes
2	12.1	0.72	43.2	3.86	0.195	Yes

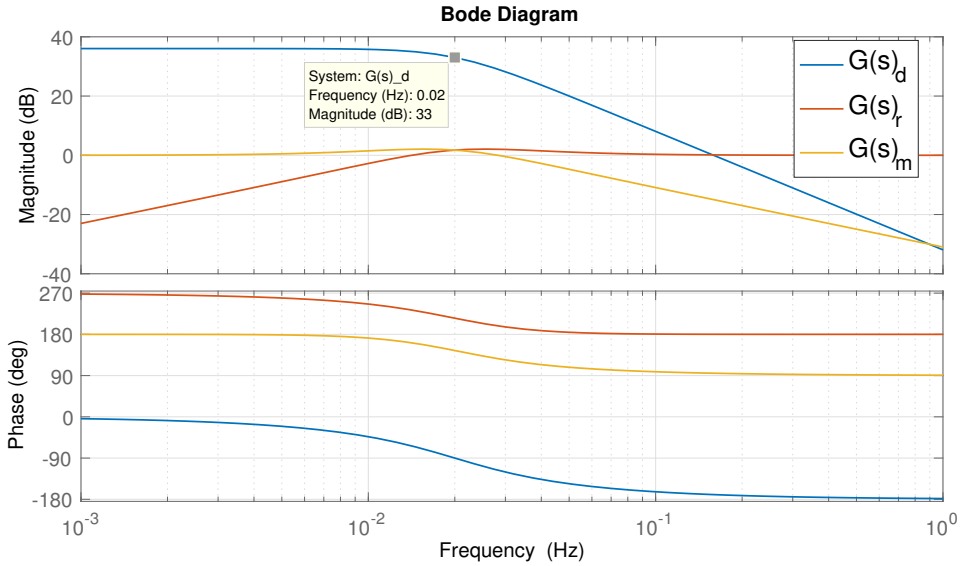

Figure 4.22: Bode diagrams of the closed-loop transfer functions relating the performance error with the different disturbance sources.

Although the above derivations are useful for obtaining basic properties of the controller, such as the bandwidth, they are not enough to ensure the stability of the system due to the assumptions made in the process. Thus, as stated in ECSS (2014) the only way to determine if a system is stable or not is by analyzing the eigenvalues of its state matrix: *"A continuous LTI system is stable if and only if all of the eigenvalues of its state matrix have strictly negative real parts"*.

The non-linear model in the body-fixed frame is given by Section 2.3.2:

$$\frac{d}{dt}\begin{pmatrix}\omega\\ \boldsymbol{q}_{1:3}\\ q_4\end{pmatrix}=\begin{pmatrix}\mathbf{J}^{-1}\left(-\boldsymbol{\omega}\times(\mathbf{J}\boldsymbol{\omega}+\mathbf{h}_\omega)+\boldsymbol{\tau}+\mathbf{d}\right)\\ -\frac{1}{2}[\boldsymbol{\omega}\times]\boldsymbol{q}_{1:3}+\frac{1}{2}q_4\mathbf{I}_3\boldsymbol{\omega}\\ -\frac{1}{2}\boldsymbol{\omega}^T\boldsymbol{q}_{1:3}\end{pmatrix} \tag{4.50}$$

If $\boldsymbol{\tau}$ is split in two components, $\boldsymbol{\tau}=\boldsymbol{\tau}_g+\boldsymbol{\tau}_c$, where the first term denotes the gyroscopic term and the second the associated to the PD, the equations simplify and the system takes the form:

$$\frac{d}{dt}\begin{pmatrix}\boldsymbol{\omega}\\ \boldsymbol{q}_{1:3}\\ q_4\end{pmatrix}=\begin{pmatrix}\mathbf{J}^{-1}\left(\boldsymbol{\tau}_c+\mathbf{d}\right)\\ -\frac{1}{2}[\boldsymbol{\omega}\times]\boldsymbol{q}_{1:3}+\frac{1}{2}q_4\mathbf{I}_3\boldsymbol{\omega}\\ -\frac{1}{2}\boldsymbol{\omega}^T\boldsymbol{q}_{1:3}\end{pmatrix}=\mathbf{f} \tag{4.51}$$

and linearising the non-linear dynamics with respect to an arbitrary operation point, the system becomes (Blanke and Larsen (2010)):

$$\frac{d}{dt}\begin{pmatrix}\boldsymbol{\omega}\\ \boldsymbol{q}_{1:3}\end{pmatrix}=\begin{pmatrix}\mathbf{J}^{-1}\left(\boldsymbol{\tau}_c+\mathbf{d}\right)\\ \frac{1}{2}\mathbf{I}_{3\times3}\boldsymbol{\omega}\end{pmatrix}=\mathbf{f} \tag{4.52}$$

Given a state-space system of the form:

$$\dot{\boldsymbol{x}}=\mathbf{A}\mathbf{x}+\mathbf{B}_c\mathbf{u}+\mathbf{B}_d\mathbf{d} \tag{4.53}$$

$$\mathbf{y} = \mathbf{C}\mathbf{x} \tag{4.54}$$

where

$$A_{ij} = \frac{\partial f_i}{\partial x_j}; \qquad B_{ij} = \frac{\partial f_i}{\partial u_j}; \tag{4.55}$$

$\mathbf{A}$, $\mathbf{B}_c$ and $\mathbf{B}_d$ are obtained as:

$$\mathbf{A} = \begin{pmatrix} \mathbf{0}_{3\times3} & \mathbf{0}_{3\times3} \\ \frac{1}{2}\mathbf{I}_{3\times3} & \mathbf{0}_{3\times3} \end{pmatrix} \qquad \mathbf{B}_c = \begin{pmatrix} \mathbf{J}^{-1} \\ \mathbf{0}_{3\times3} \end{pmatrix} \qquad \mathbf{B}_d = \begin{pmatrix} \mathbf{J}^{-1} \\ \mathbf{0}_{3\times3} \end{pmatrix} \tag{4.56}$$

Introducing the control law of the form $\mathbf{u} = \boldsymbol{\tau}_c = [\mathbf{K}_d, \mathbf{K}_p][\delta\mathbf{q}_{1:3}, \Delta\boldsymbol{\omega}]^T$ into the system the final closed feedback loop is given by:

$$y(s) = \mathbf{C}\left(s\mathbf{I}_{6\times6} - \mathbf{A}_{\text{cl}}\right)^{-1}\mathbf{B}_{\text{cl}}\, y_r(s) \tag{4.57}$$

with the state matrix in closed-loop being:

$$\mathbf{A}_{\text{cl}} = (\mathbf{A} - \mathbf{B}_c\mathbf{K}\mathbf{C}) \tag{4.58}$$

where $\mathbf{K} = [\mathbf{K}_d, \mathbf{K}_p]$ and $\mathbf{C} = \mathbf{I}_{6\times6}$. The eigenvalues of $\mathbf{A}_{\text{cl}}$ are then computed obtaining:

$$\begin{aligned} &-0.0889 \\ &-0.0889 \\ &-0.0889 + 2.2127\cdot10^{-9}\, i \\ &-0.0889 - 2.2127\cdot10^{-9}\, i \\ &-0.0889 + 1.1427\cdot10^{-9}\, i \\ &-0.0889 - 1.1427\cdot10^{-9}\, i \end{aligned}$$

Looking at the results, it is possible to see that the real part of all the eigenvalues is strictly negative and thus the stability of the system is ensured. Furthermore, the fact that the real part of all the eigenvalues has the same value, it is due to the way the controller has been designed. This is because one component of the controller $\boldsymbol{\tau}_g$ nullifies the gyroscopic term whereas in the other $\boldsymbol{\tau}_c$, the gains have been selected proportional to the inertia tensor, which implies that all the axes are controlled in the same way. Note that here perfect knowledge of the variables have been assumed.

4.6. POINTING PERFORMANCE

In Equation (4.39) the analytic expression for the performance error as a function of the disturbances, reference commands and measurement noise was obtained. The instantaneous value of the performance error at any given time is defined as the APE (ECSS, 2014).

In this section, the APE is analysed. First, an analytic approach is followed to estimate the boundary limits for the APE. Second, Monte Carlo simulations are run to validate the performance of the system. In these simulations all the different contributors to the attitude pointing mentioned during the chapter are included coupling both translational and rotational motion. Finally, the results regarding the unloading of the reaction wheels are also presented and their influence to the dynamics of the spacecraft. For this analysis the BFF is taken and thus all the axes are referred to it.

4.6.1. ABSOLUTE PERFORMANCE ERROR

To study the APE, first the external disturbances affecting the spacecraft are studied. When the observer adopts a nominal configuration (assumed to be close to the Sun-NEO line at a distance of ~ 5 km from the asteroid), SRP varies its value with a 1/2 year period. Although the SRP approaches a sine function, for short times, it can be seen as a step disturbance. An average distance of 1 au is taken for simulation purposes and the disturbance is approximated to a step response whose magnitude is the value of the perturbation at this distance. This is:

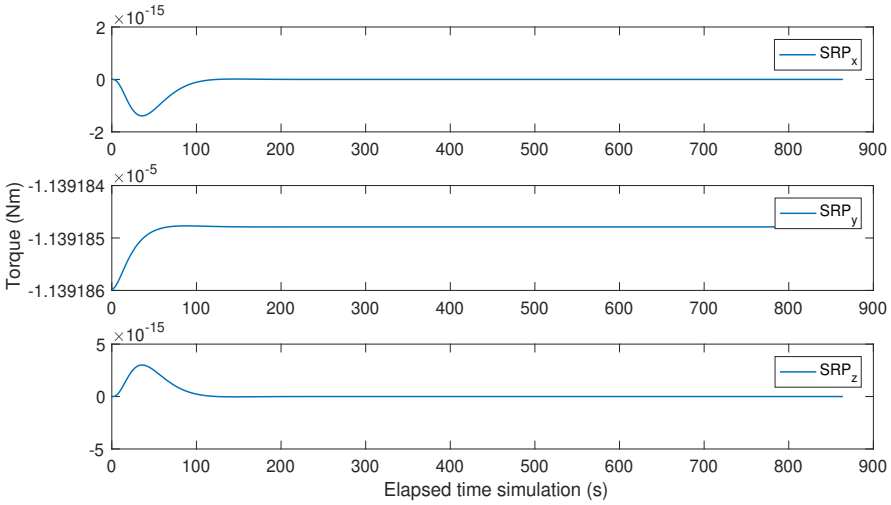

Figure 4.23: SRP torque exerted in each of the axes considering perfect knowledge of the system (no noise) and a fixed position.

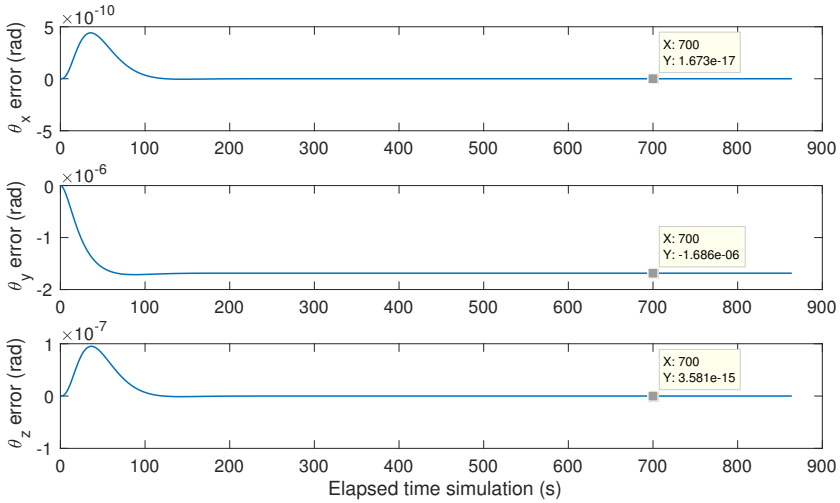

Figure 4.24: Pointing error caused by the unique effect of SRP.

$$d = \frac{\mathbf{J}^{-1}\boldsymbol{\tau}_{\text{SRP}}}{s} \tag{4.59}$$

where the steady state value of $\boldsymbol{\tau}_{\text{SRP}}$ is presented in Figure 4.23. For this analysis, it has been considered perfect knowledge of the system (no noise) and fixed position relative to the NEO. The only influence in the dynamics, the SRP, is isolated for its analysis.

The value reached is $[0, -1.1392 \cdot 10^{-5}, 0]$ Nm. Using Equation (4.43) and applying the final value theorem (FVT) the hang-off error introduced in the system is equal to:

$$\epsilon_p^d = \frac{\mathbf{J}^{-1}\boldsymbol{\tau}_{\text{SRP}}}{k_p} = \begin{pmatrix} 0 \\ -1.6855 \cdot 10^{-6} \\ 0 \end{pmatrix} \quad \text{rad} \tag{4.60}$$

and analysing the absolute pointing error of the spacecraft, the same result is obtained (Figure 4.24).

The second source of error is the motion of the spacecraft itself. If a continuous trajectory is assumed, the guidance command approximates to a ramp inducing a hang-off error into the system proportional to the variation of the position. This assumption can be done due to the low velocities of the spacecraft (e.g.

for a velocity of the order of 2 cm/s an increment in position of 1.2 m is produced between two consecutive measurements). With the use of Equation (4.44) and the FVT, the performance error is:

$$\epsilon_p^{\text{ref}} = -\frac{k_d}{k_p}\Delta\theta^{\text{ref}} \tag{4.61}$$

To analyse this error, only SRP effect and the motion of the spacecraft has been considered. In Figure 4.25, the trajectory of the spacecraft in the neoS frame is presented for a simulation time of 8000 s. With the information available, the mean variation of the guidance reference can be computed as:

$$\Delta\theta^{\text{ref}} = \left(\theta_f^{\text{ref}} - \theta_0^{\text{ref}}\right)/\Delta t = \left(\arctan\frac{y_f}{x_f} - \arctan\frac{y_0}{x_0}\right)/\Delta t = -2.4602\cdot 10^{-7}\,\text{rad/s} \tag{4.62}$$

Applying Equation (4.61), the motion is translated into an error equal to $2.7687\cdot 10^{-6}$ rad. Note that this source only induces an error in the x and y axis as the z-axis is constantly pointing the asteroid. Figure 4.26 shows the introduced hang-off error in the x-axis matching the predicted one.

Considering now that the baseline trajectory (Figure 3.44) covers the full span of the sphere (lateral and vertical), and this one has a diameter of 1500 m and a thrusting frequency of about ~ 0.7 commands/day, this introduces a hang-off error of $2.7151\cdot 10^{-5}$ rad in x and y axis. This is:

$$\Delta\theta^{\text{ref}} = 2\arctan\left(\frac{r_{\text{sphere}}}{d_{\text{ref}}}\right)/\left(\frac{1\text{ day}}{\text{manoeuvre freq.}}\right) \tag{4.63}$$

Note, however, that this errors do not occur at the same time in both axis and with the same magnitude. It is thus, a conservative value chosen.

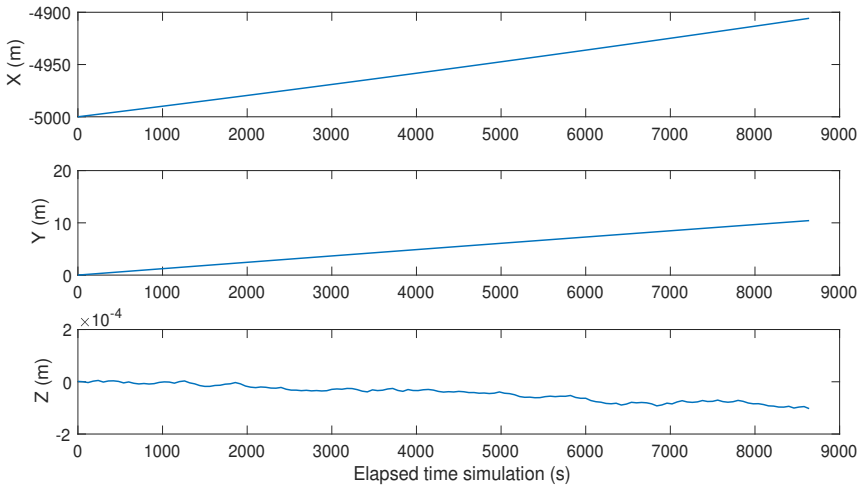

Figure 4.25: Relative trajectory described by the spacecraft during the elapsed time simulation represented in the neoS frame.

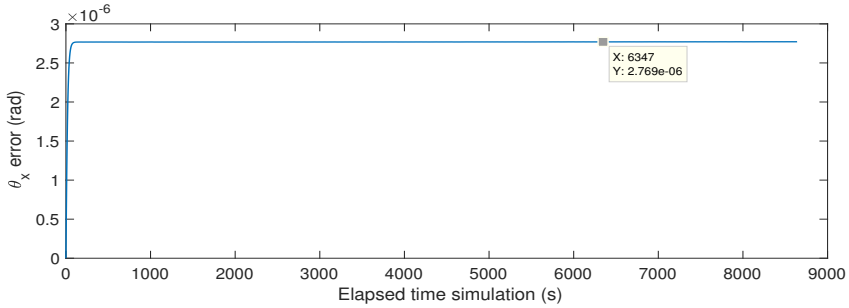

Figure 4.26: Introduced error due to the relative motion between the spacecraft and the NEO.

Another source of error related to the guidance and the translational EKF exists. As the position is updated every 60 s, the change between two consecutive steps introduce an initial error that converges after several seconds to the final error caused by the actual difference between the estimated reference and the trajectory itself. This error is difficult to quantify and for that reason, it has been estimated numerically. Figure 4.27 shows the attitude only affected by this error, whose standard deviation for each axis is shown in Table 4.9.

Regarding the attitude sensors, the star tracker introduces a noise of $[3,3,25]$ arcsec in each of the axis with a bias of $[5,5,3.5]$ arcsec with 1σ accuracy (Table 4.1). The noise is attenuated by the controller whereas the bias affects directly the plant. The attenuation is shown in Figure 4.28, where a white random noise according to the star tracker specifications is compared with the filtered one due to the transfer function that relates the measurement noise with the performance error (Equation (4.45)). The filtering corresponds to a reduction of the standard deviation of a factor ~ 10.

Finally, the last significant source of error refers to the gyroscopic term. Due to the amount of factors involved (uncertainly in inertia matrix, angular momentum of the wheels, low pass filter,...) the error must be studied numerically. However, it was noted that this error is strongly related with the angular momentum

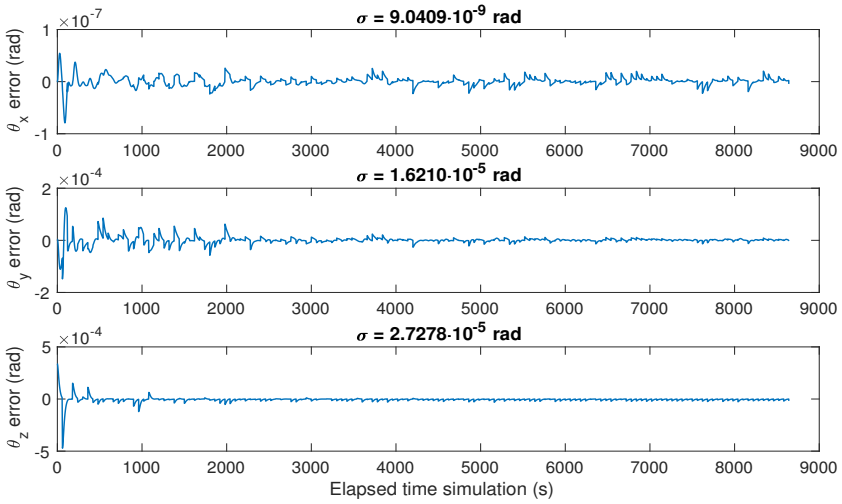

Figure 4.27: Introduced error due to the spacecraft translational EKF.

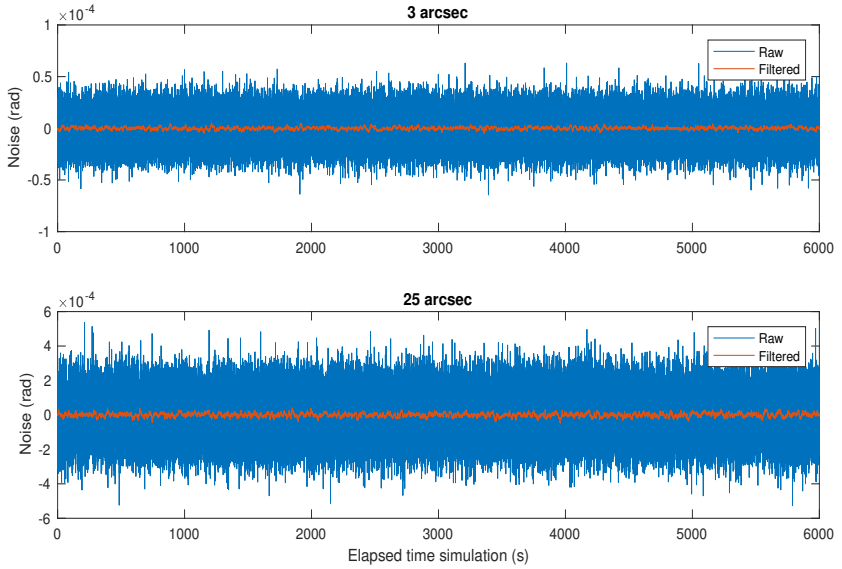

Figure 4.28: Noise reduction due to the controller filtering.

of the wheels ($\boldsymbol{\omega} \times \boldsymbol{h}_\omega$). To do this, a simulation has been run assuming perfect knowledge of the EKF and only with the star tracker noise (no bias). The error due to the inertia matrix has been considered negligible compared with the RW term, for containing ω^2 terms and being ω in general very small. Then the error due to the gyroscopic term is the difference between the standard deviations of the noise due to the star tracker and the numerical absolute pointing error noise obtained (Figure 4.29). For this operation, uncorrelated noise has been assumed (Ott et al., 2011), which is translated into:

$$\sigma^2_{\text{Total}} = \sigma^2_{\text{gyro}} + \sigma^2_{\text{STR}} \tag{4.64}$$

All the error sources with their values are collected in Table 4.9. Analysing these, it can be seen that they contribute in a different way to the performance error. First regarding the biases, the SRP represents one tenth of the error due to the bias of the star tracker, being almost negligible the action of this force in the pointing error. The star tracker predominates above the rest, as its value is 1σ accuracy in opposition with the bias related with the movement that its value is given by 3σ accuracy. With respect to the noises, the EKF noise due discrete update of the position, drives the noise in the body-fixed y and z axis whereas the noise due to the gyroscopic term actuating in the y axis is also relevant. Focusing on the gyroscopic term, this is formed by a term containing the inertia matrix and another term containing the angular momentum of the wheels. Because of the current disposition of the angular momentum in the wheels (along the BFF x-axis) the influence of this error is allocated in the BF y and z axis whereas the x-axis is dominated by the inertia matrix. Looking at the order of magnitude of the noises, the inertia matrix represents one tenth of the noise due to the angular momentum of the wheels. This suggests that allocating the angular momentum in another axis, the error in that axis will decrease considerably. One more remark regarding the BFF x-axis is that the biases predominate over the noises.

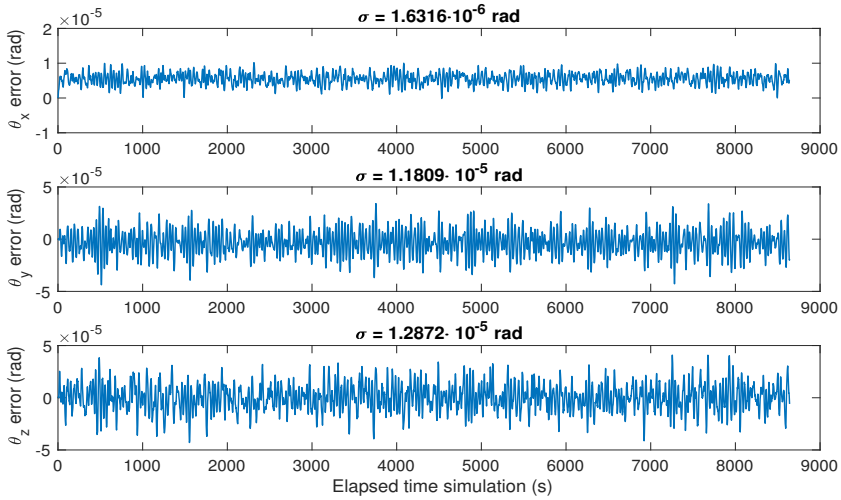

Figure 4.29: Absolute performance error considering only star tracker noise.

Table 4.9: Estimated pointing performance, assuming conservative values for each error source.

Error sources	**Axis, units (rad)**			**Remarks**
	X	**Y**	**Z**	
Bias SRP	0	$-1.6855 \cdot 10^{-6}$	0	-
Bias due to movement	$2.7151 \cdot 10^{-5}$	$2.7151 \cdot 10^{-5}$	0	The EKF assumes 3σ acc. thus, same is selected.
Bias star tracker	$2.4241 \cdot 10^{-5}$	$2.4241 \cdot 10^{-5}$	$1.6968 \cdot 10^{-5}$	1σ
Noise EKF	$9.0409 \cdot 10^{-9}$	$1.6210 \cdot 10^{-5}$	$2.7278 \cdot 10^{-5}$	1σ
Noise star tracker	$1.4544 \cdot 10^{-6}$	$1.4544 \cdot 10^{-6}$	$1.2120 \cdot 10^{-5}$	1σ
Noise gyroscopic term	$7.3944 \cdot 10^{-7}$	$1.1719 \cdot 10^{-5}$	$4.3338 \cdot 10^{-6}$	1σ
Total	$1.0424 \cdot 10^{-4}$	$[-1.6173, 1.5835] \cdot 10^{-4}$	$1.4139 \cdot 10^{-4}$	3σ

For the calculation of the error budget, each of the error sources has been considered uncorrelated. This assumption has been adopted because every source of error has been studied independently from each other. The only case in which the assumption is arguable is for the gyroscopic term, as both noises coming from the angular velocity of the spacecraft and angular momentum of the wheels are combined. For uncorrelated noise, Ott et al. (2011) establish the following criteria for adding noises:

$$\mu_B = \sum_{i=1}^{N} \mu_i \qquad \sigma_{\text{uc}}^2 = \sum_{i=1}^{N} \sigma_i^2 \tag{4.65}$$

where μ_i represents each of the biases and σ_i the standard deviation for the noises. The total error has been obtained adding the total error caused by the bias plus the resultant standard deviation.

Now, that pointing error has been bounded, the problem is studied in a numerical way running a 58-run Monte Carlo simulation. The reason for this amount of runs obeys the same reasoning as Section 3.4. The requirements are set based on Rosetta mission pointing performance (Fiebrich et al., 2004) as mentioned in Section 1.3. The pointing error boundaries (red) denote the predicted analytical APE. Note that this value is below the performance requirement NS-GNC-04 which establishes a limit of 0.0289 deg per axis. The results are shown in Figures 4.30 and 4.31.

From these results, it can be observed that the performance error remains always below Rosetta's one. However, this value must be treated carefully. Although using the three star trackers available some of the error could be reduced, there are other sources that will increase it. These are errors in the tachometers of the wheels, variations in the update rate of the star trackers, quantization, etc. Furthermore, the star tracker update rate has been assumed to be working at 16 Hz. This is a feasible value if apart from three star tracker heads, three processing units are included. However, if this assumption is relaxed and the update rate decreases, the pointing error will also increase.

Focusing on specific values per axis, some conclusions can be drawn (Figure 4.30). As predicted before,

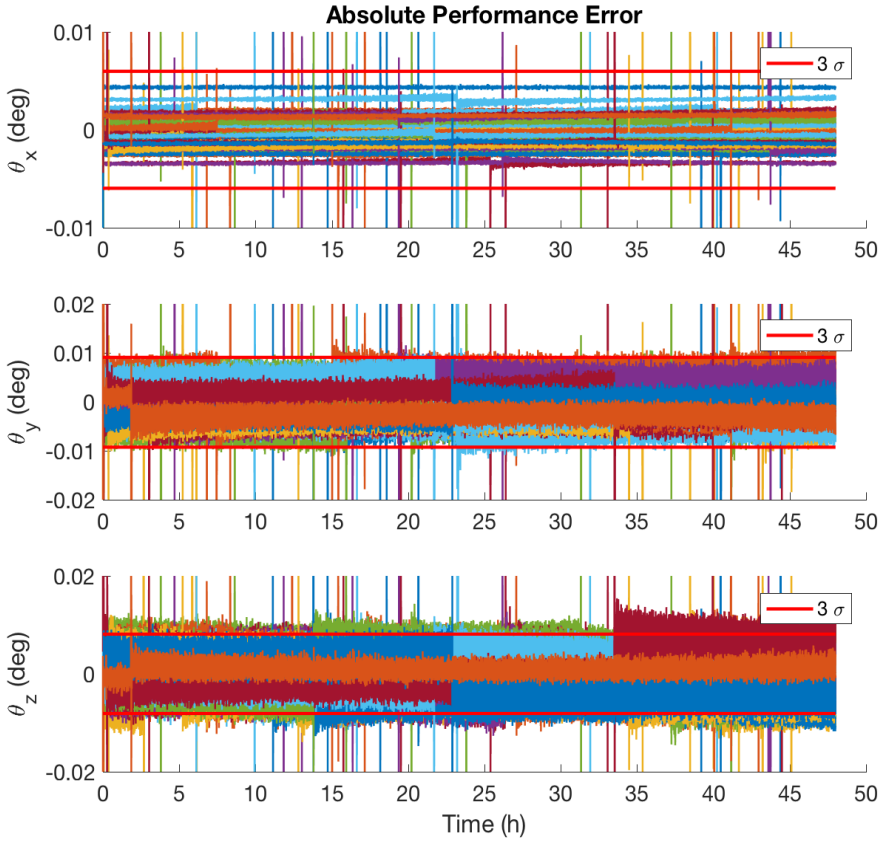

Figure 4.30: Absolute performance error for a 58-runs Monte Carlo simulation.

in the BFF x-axis, the APE is mainly driven by biases. This can clearly observed in the values close to the boundary, where there is a gap between some runs and the noise does not overlap. Analysing the BFF y-axis, similar conclusions matching the predicted data can be obtained. Taking only the data related to the bias, the maximum value (3σ) is $\sim 1 \cdot 10^{-4}$ rad (0.0057 deg). Looking at the results, for example the data set visualized in orange, it can be seen that the noise is displaced a value close to 0.005 deg. However, this is not the case for the BFF z-axis. The bias represents only ~ 0.003 deg out of the ~ 0.008 deg of the envelope, but looking at the data sets close to the boundary (e.g. maroon signal), it is possible to observe that some are centered with values higher than the predicted one. The consequence of this results is that there is an extra bias driving the pointing error and this is probably related with the gyroscopic term. Further research has to be done in that sense.

The peaks present in the plots are caused by translational manoeuvres due to disturbance torques that appear when the thrusters are commanded Section 4.1.2. Analysing the full range of the APE (Figure 4.31), it can be seen that they are below 0.4 deg for BFF x-axis and below 2 deg for the other two. In fact, this is a pessimistic boundary for the y and z axis. This can be due to the fact that the torques causing this error are mainly located at the first instants of time where the navigation filter is still converging and the state provided by the EKF contains largest errors (e.g. Figure 3.13). Taking only values for 1h onwards, the APE caused by the errors in the thrusters are ~ 1 deg for the BFF y-axis and ~ 0.5 deg for the BFF z-axis.

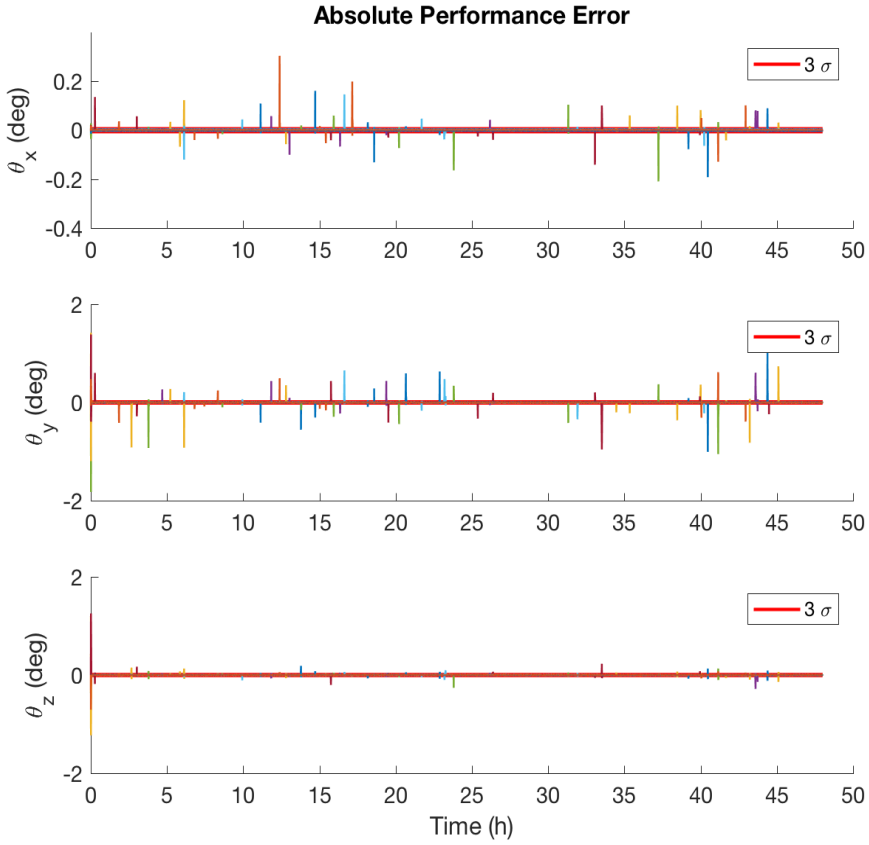

Figure 4.31: Absolute performance error for a 58-runs Monte Carlo simulation full view.

Regarding the angular velocity and angular rate, the results are shown in Figures 4.32 and 4.33 respectively. Analysing Figure 4.32b, it can be seen that the performance requirement NS-GNC-05 is sometimes violated. This means that during translational manoeuvres the image of the asteroid might be blurred, decreasing the performance of the navigation system. Zooming at some of the largest peaks, it can be observed that the time that the spacecraft takes to come back to the specified boundaries is about half a minute, whereas it takes a couple of minutes to come back to nominal performance Figure 4.32a. This situation might not pose a problem due to the fact that the navigation system is updated every 60 s. However, the best solution would be to

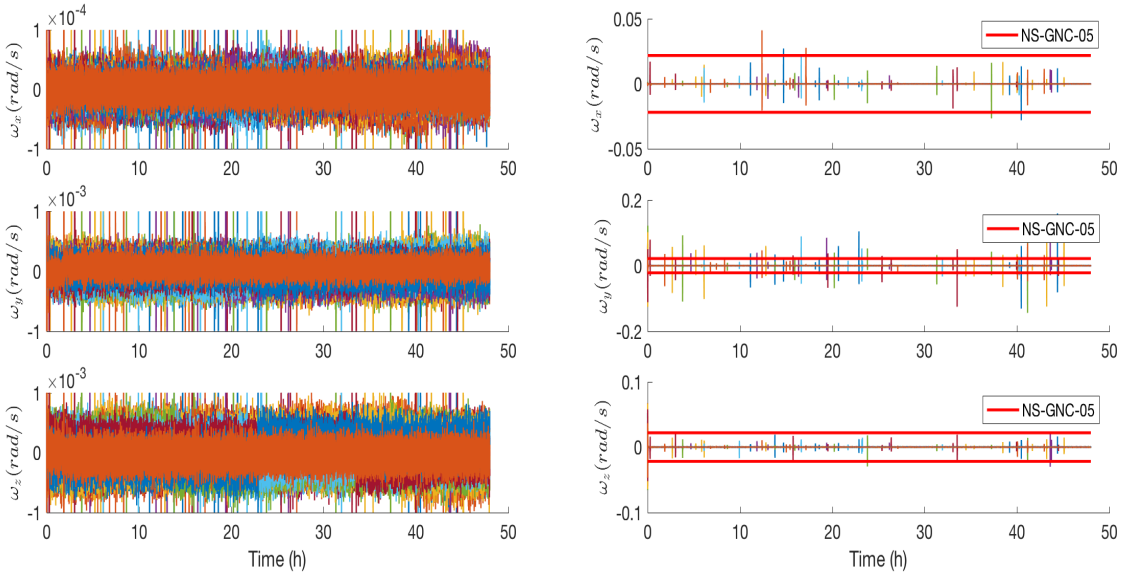

(a) Zoomed view (b) Full view

Figure 4.32: Angular velocity for a 58-runs Monte Carlo simulation.

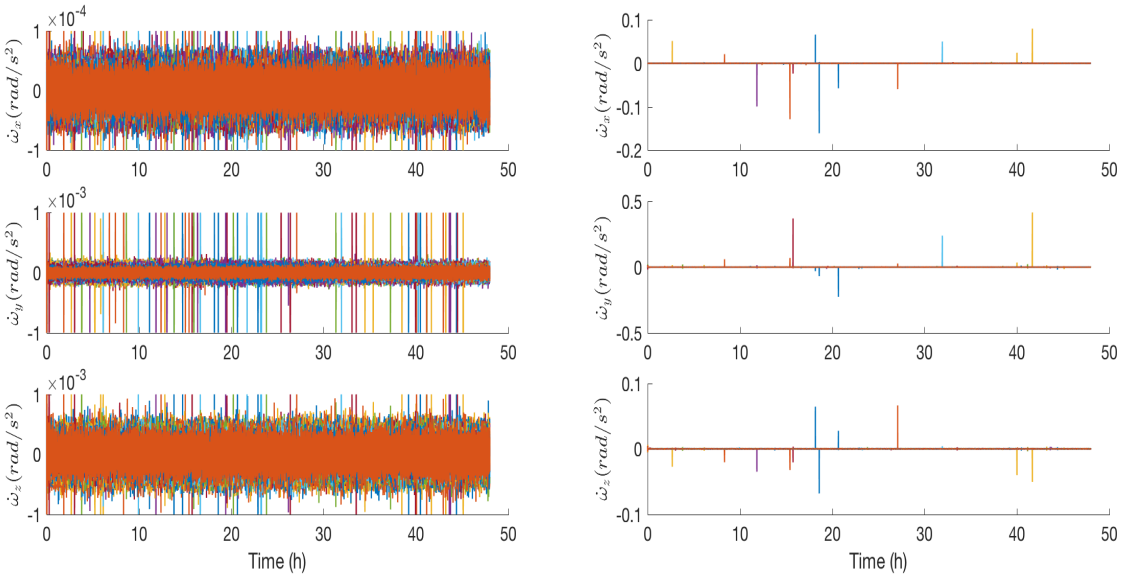

(a) Zoomed view (b) Full view

Figure 4.33: Angular acceleration for a 58-runs Monte Carlo simulation.

perform longer translational manoeuvres, so that the error in torque introduced is reduced. Furthermore, an important remark from these results is that at some peaks both angular velocity and angular rate exceed the performance properties of the star tracker: 6 deg/s and 2.5 deg/s^2 or 0.1047 rad/s and 0.0436 rad/s^2 respectively. This is specially true for the case of the angular acceleration Figure 4.33b. For this reason, a deeper analysis of the torques provoked by translational manoeuvres is recommended for future work. Finally, as a overall tendency, the largest noise is located in the BFF-y and BFF-z axis respectively. The only variable that has direct impact in those two axis is the gyroscopic term corresponding to the angular momentum of the wheels, which suggests that depending on the distribution of the momentum the noise can be decreased or

modified as desired. This analysis is also recommended for future work.

4.6.2. MOMENTUM UNLOADING

For the momentum unloading, the initial velocity assumed of the wheels is twice the nominal one (Equation (4.12)), which means that all the reaction wheels are saturated. This represents the worst case, as the momentum to dump is greater which implies longer manoeuvres. Studying the worst-case scenario also avoid the use of Monte Carlo campaigns to draw conclusions about the overall performance of the system (ECSS, 2014). $\boldsymbol{h}_{\omega,\text{ref}}$ has been chosen to be $[27.4, 0, 0]$ Nms, which is equivalent to a reference wheel speed of $[-314.2, -314.2, 314.2, 314.2]$ rad/s. Two extreme cases are presented: one for a thrust level of 7 N and another one for 24 N, comparing the similarities and differences between them.

When the system detects that a reaction wheel is saturated, the thruster management function compute the equivalent torque that needs to be distributed for each of the thrusters and then the PWPF modulator decides to switch on/off based of the activation/deactivation limits. Figures 4.34 and 4.35 show the activation of the thrusters that take part in the momentum unloading with their different pulse duration and the equivalent torque and force introduced to the spacecraft. For the unloading of a momentum in the BFF x-direction, thrusters number 6,7,9 and 12 take part in the manoeuvre. In the zoomed image of Figures 4.34 and 4.35 it can be seen that the duration of the pulses is about ~ 0.25 s which is superior than the minimum impulse bit (MIB) Table 4.2. This means that the pulse duration of the thrusters is still far from their physical limitations and the torque can be controlled more accurately improving the tuning of the PWPF.

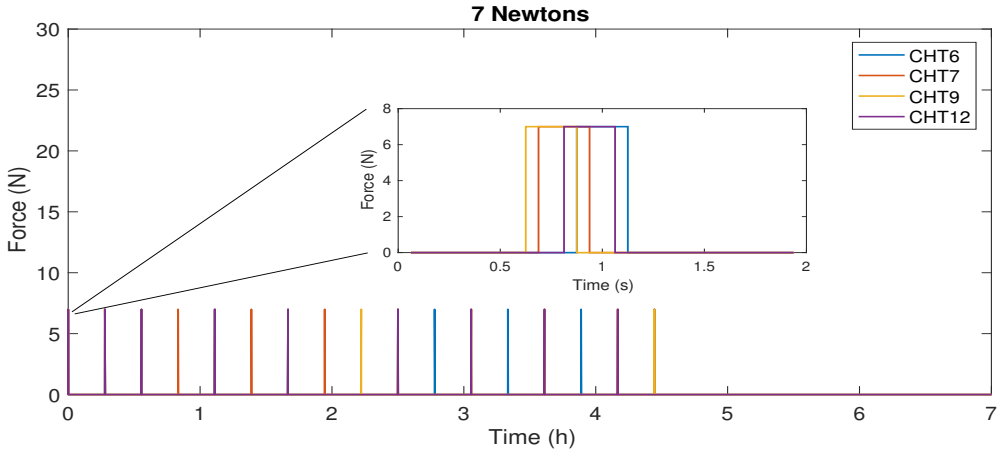

Figure 4.34: CHT commanded pulses resulting from the PWPF modulator.

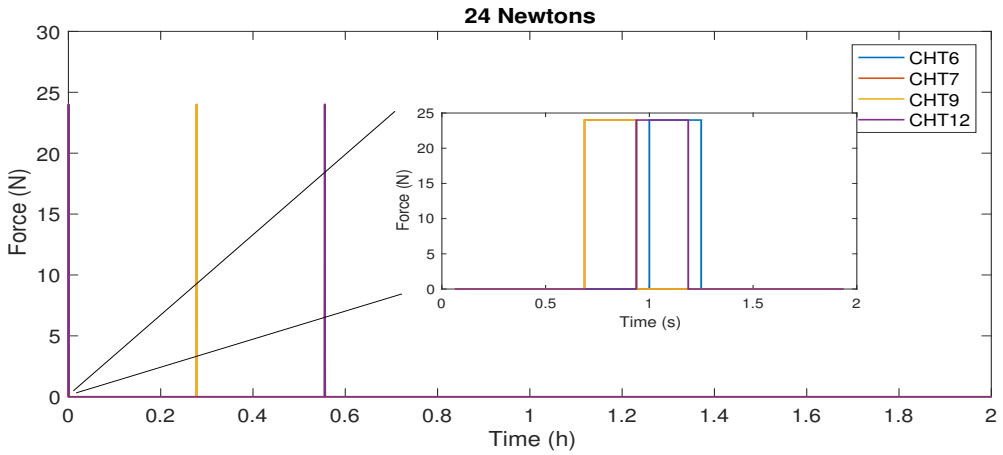

Figure 4.35: CHT commanded pulses resulting from the PWPF modulator.

The thrusters pulses are translated into torques and forces by means of the influence matrix. As it is possible to observe, the summation of torques in each of the directions is almost equal to zero in the axes that no torque is desired (Figure 4.36). This also happens with the forces in every axes as force-free torque is desired (Figure 4.38). However, the PWPF introduces some errors due to the fact that the input torque is not perfectly transmitted. These errors can be observed in Figure 4.39 in which forces in the y and z directions do not match perfectly, whereas they do it for the torque levels (Figure 4.37). This fact implies that no force-free torque has been commanded. The reason for this issue has to do with the fact that for this manoeuvre, the PWPF has not activated CHT7 (Figure 4.35), as it has not arrived to the switching point (U_{on}). For the 7N case (Figure 4.34), CHT7 does reach the switching point and thus its activation reduces the error induced in Figure 4.38. Actually the induced velocity error for the 7N case is practically null during the first command ($t \sim 0$ s) (Figure 4.40), whereas for the 24N case and initial error in the velocity is automatically introduced (Figure 4.41). Looking at the zoomed portion of Figure 4.40 it can be observed that the ΔV errors introduced are similar to the ones used for the translational motion (Figure 3.38), which shows that the method implemented can work with an appropriate tuning of the gains and smaller thrusters.

One significant difference between the different pulses is that although the same amount of torque is desired to be commanded at each manoeuvre, the torque varies at each one. This is due to the fact that the PWPF keeps the residual values for each of the thrusters and when the system is enabled again, these do not get load in the same way they did it in previous manoeuvre. In general, for the purpose of momentum unloading, this is a problem because introduces errors in translational velocity.

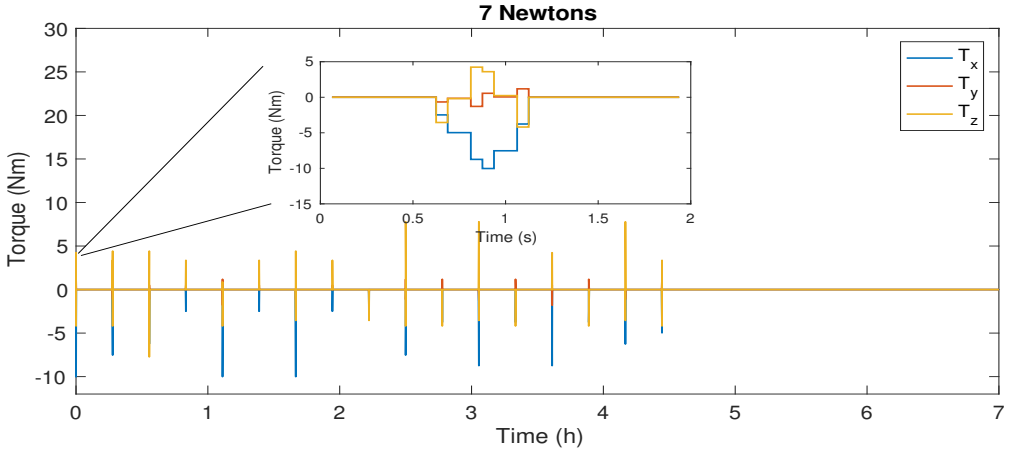

Figure 4.36: Equivalent torque introduced to the spacecraft due to thruster activation.

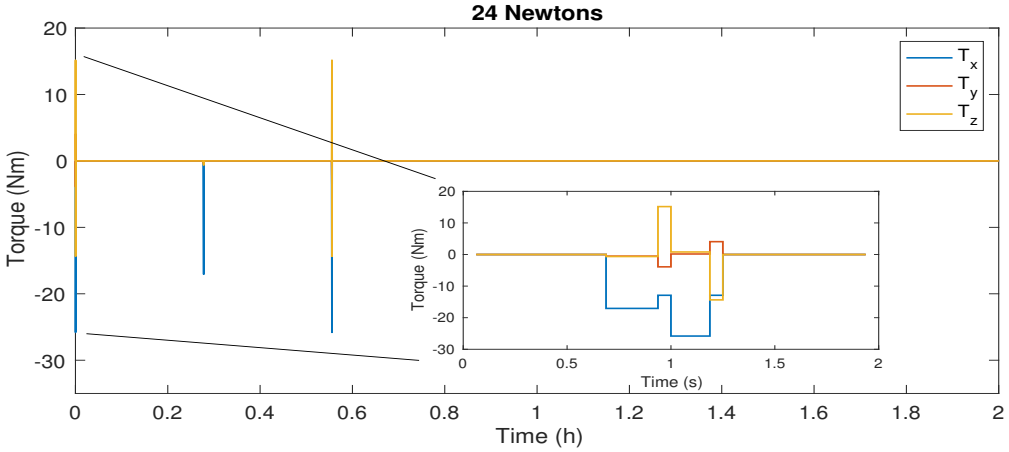

Figure 4.37: Equivalent torque introduced to the spacecraft due to thruster activation.

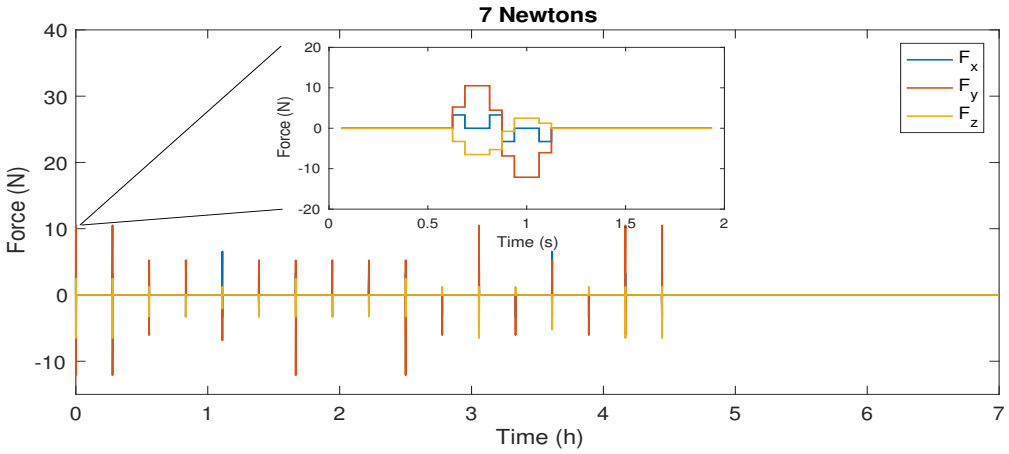

Figure 4.38: Equivalent force introduced to the spacecraft due to thruster activation.

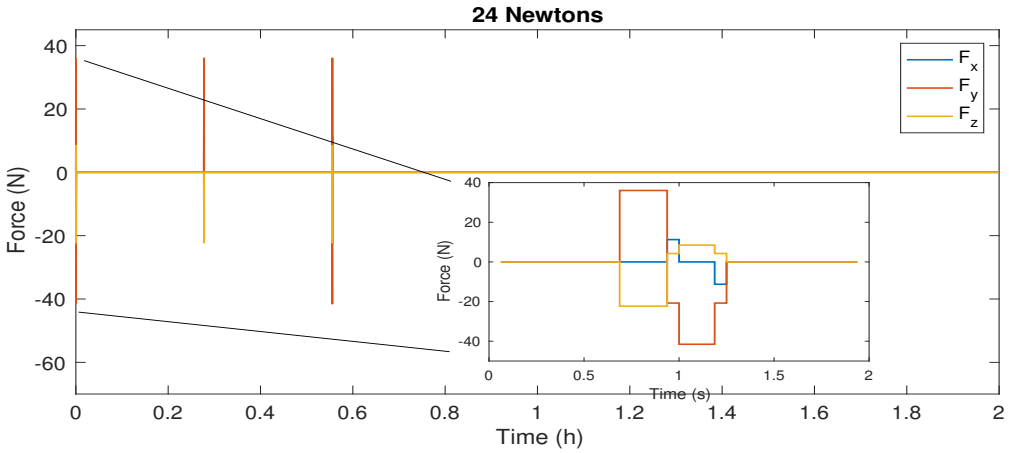

Figure 4.39: Equivalent force introduced to the spacecraft due to thruster activation.

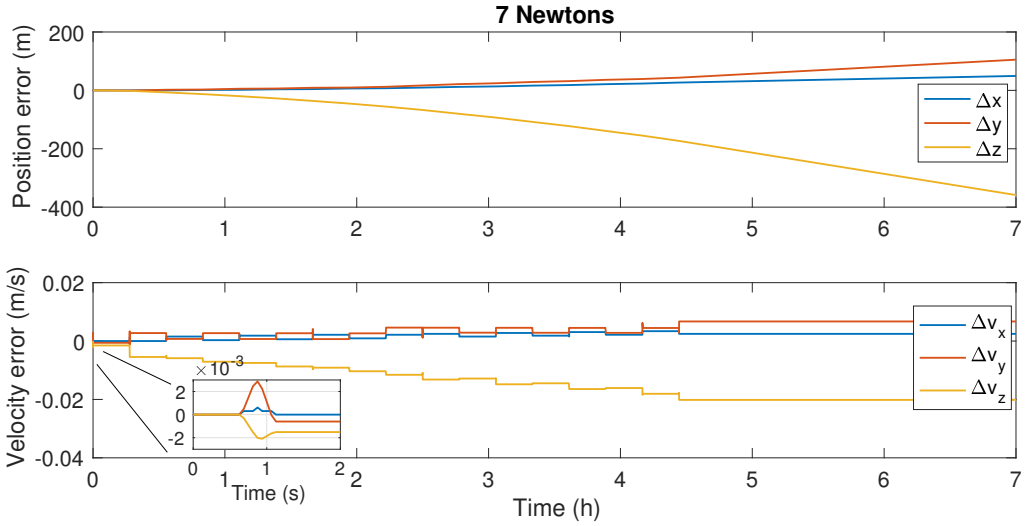

Figure 4.40: Error introduced in the translational motion as a consequence of the commanded torque errors.

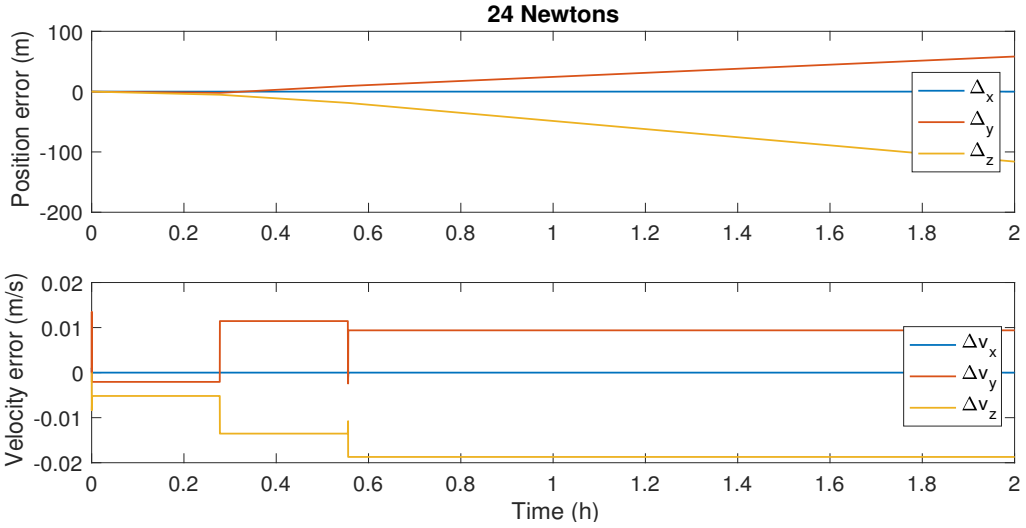

Figure 4.41: Error introduced in the translational motion as a consequence of the commanded torque errors.

With respect to the translational motion, the mentioned errors caused by PWPF and the fact that rotational and translational motion are coupled, introduce errors in terms of Δvel and Δpos. This indicates that either after each manoeuvre or after the complete unloading process, the velocity and position must be corrected. Although both rotational and translational motion are coupled because of the thruster location (no force-free torque or torque-free force), the distribution does allow to command ΔV manoeuvres with zero $\Delta\omega$ and vice-verse. This means that once the ΔV error is corrected, the reaction wheels will have to act again to bring the spacecraft from the resultant attitude to point towards the asteroid, modifying again a certain magnitude the angular momentum stored by the wheels.

The momentum introduced by the thrusters cause the reaction wheels to saturate as they are not able to decelerate at the same rate, Figures 4.42 and 4.44 show this behaviour. As the wheels saturate the momentum dumping needs to be controlled to allow the wheels to come back to nominal values. For that reason, a timer between commands need to be established. A flag that checks the switching of the thrusters was implemented for this purpose and after each manoeuvre the system was forced to wait for 1000 s for the next command. This flag is the responsible for the long duration time for the spacecraft to unload the wheels. However, this time can be reduced by a factor of 5 in the case of 7 N thrust level and a factor of 2 for the 24 N case. This information can be seen in Figures 4.42 and 4.44. In the first case, the wheels take around 200 s to be stabilized around their nominal values whereas for the 24 N case, it requires a bit more ~ 500 s. This sets a duration of the complete unloading manoeuvre between 30 min and 1 hour.

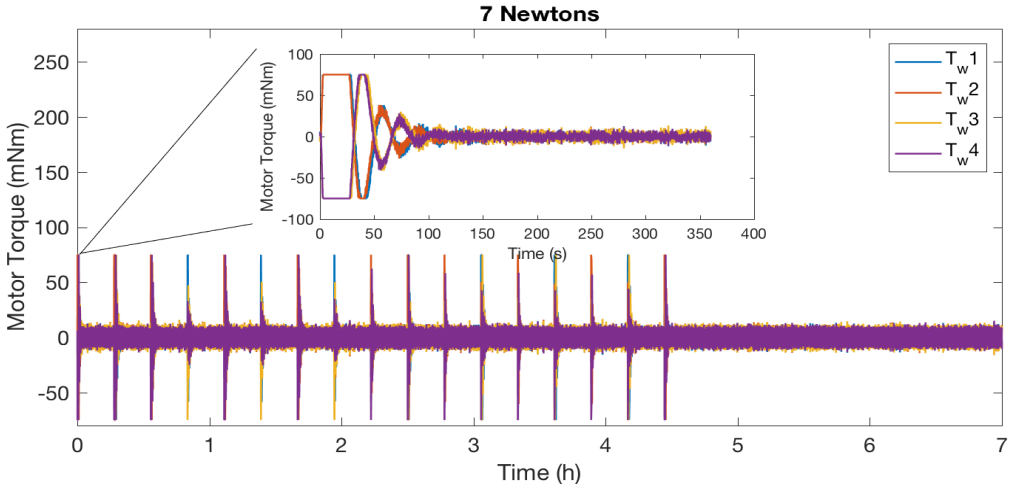

Figure 4.42: Motor torque applied to each of the reaction wheels during momentum dumping.

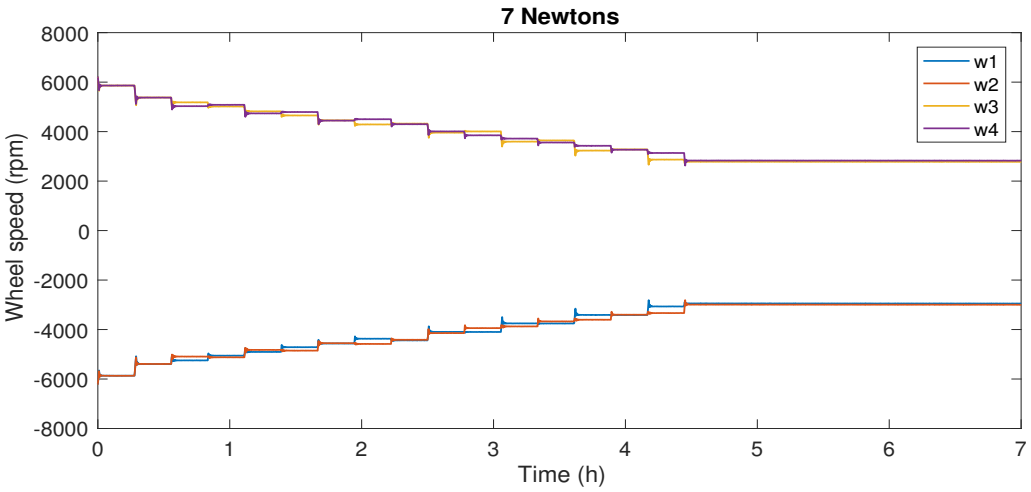

Figure 4.43: Time evolution of the reaction wheel speeds during momentum dumping.

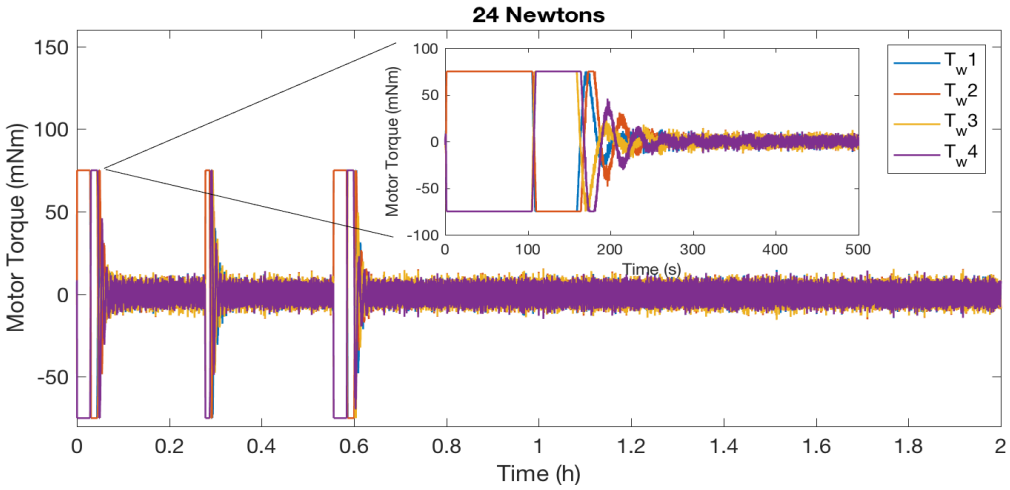

Figure 4.44: Motor torque applied to each of the reaction wheels during momentum dumping.

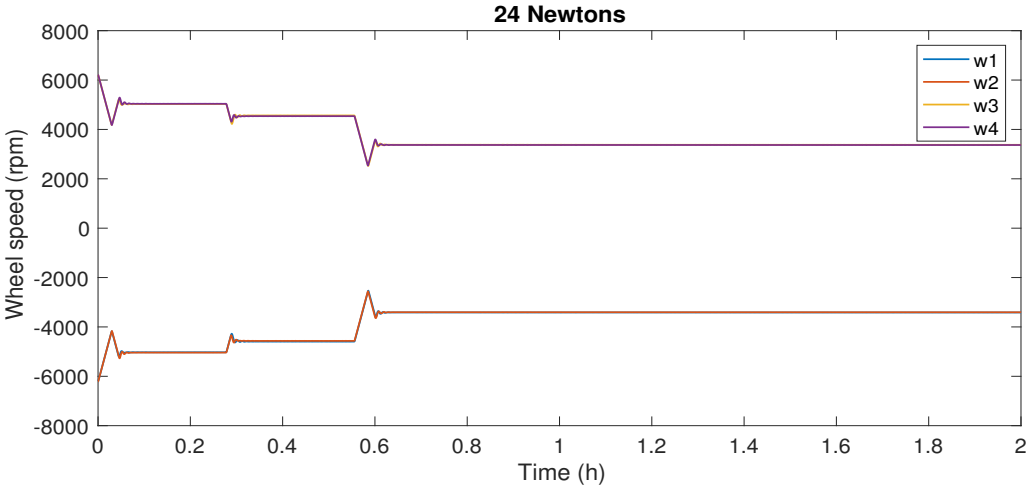

Figure 4.45: Time evolution of the reaction wheel speeds during momentum dumping.

Figures 4.46 to 4.51 show the impact in the attitude dynamics when a torque is introduced. First, regarding the line-of-sight error (LoS), the unloading does not pose a problem for the 7 N case Figure 4.46, as the error introduced is about 1.5 deg, which is below the NAC field of view capabilities (10.3 deg). However, for thrust levels of 24 N, the manoeuvre must be treated carefully, as it reaches values of 8 deg deviation and this can cause the spacecraft to loose the asteroid from the image. The good news is that during the observation phase, the typical pressurization values for the tank do not allow these thrust levels (Figure 4.1). Even so, momentum dumping manoeuvres are recommended to be avoided in regions close to the boundaries of the control box, as to stay close to the Sun-NEO line allows wider margins.

An important result from Figures 4.48 to 4.51 is that the angular velocities and rates are below the physical specifications for the star tracker, meaning that the star tracker is able to follow dumping manoeuvres in both cases. The reason why it is able to follow dumping manoeuvres but might suffer from translational ones has to do with the duration of the manoeuvre (0.5 s vs 1 s). Furthermore, the angular velocities are also far from the performance requirement NS-GNC-05, meaning that the navigation system will not process blurred images.

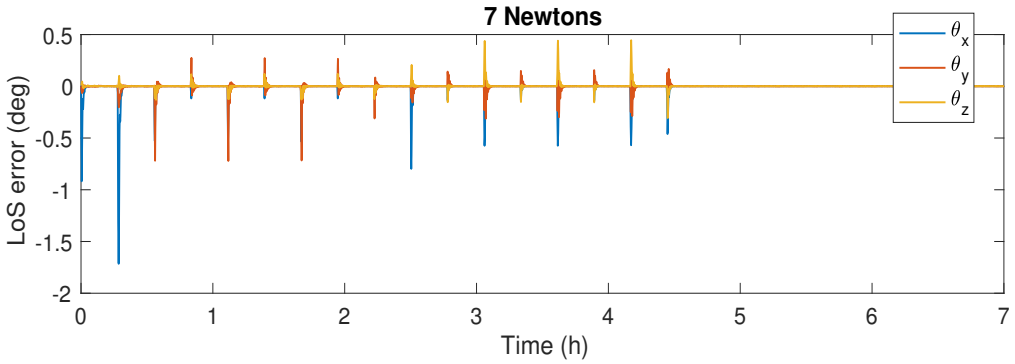

Figure 4.46: Error introduced in each of the axis due to the commanded torque.

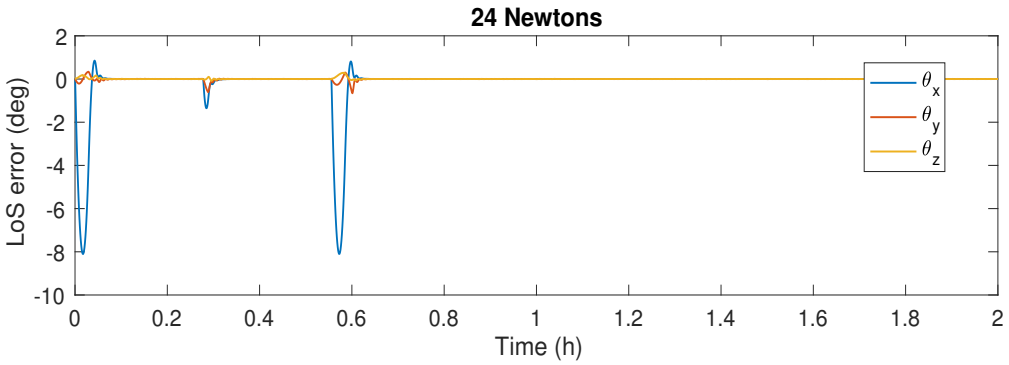

Figure 4.47: Error introduced in each of the axis due to the commanded torque.

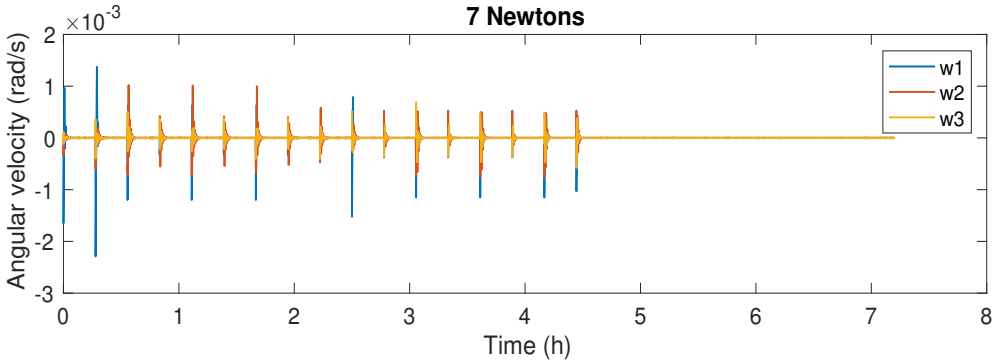

Figure 4.48: Angular velocity introduced in each of the axis due to the commanded torque.

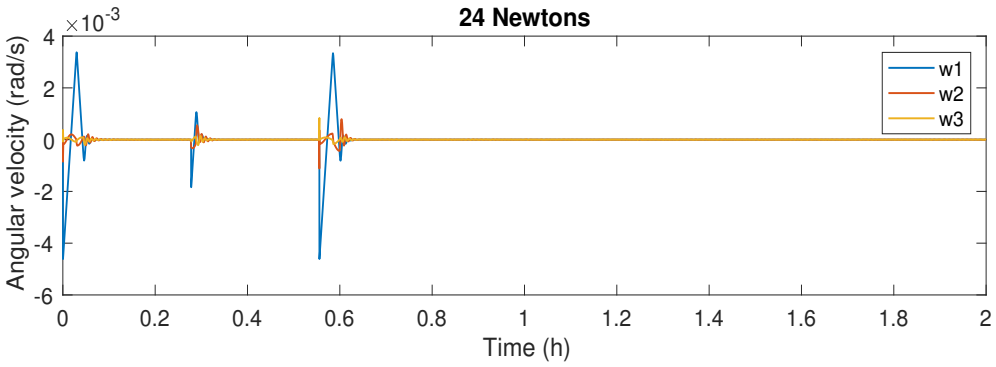

Figure 4.49: Angular velocity introduced in each of the axis due to the commanded torque.

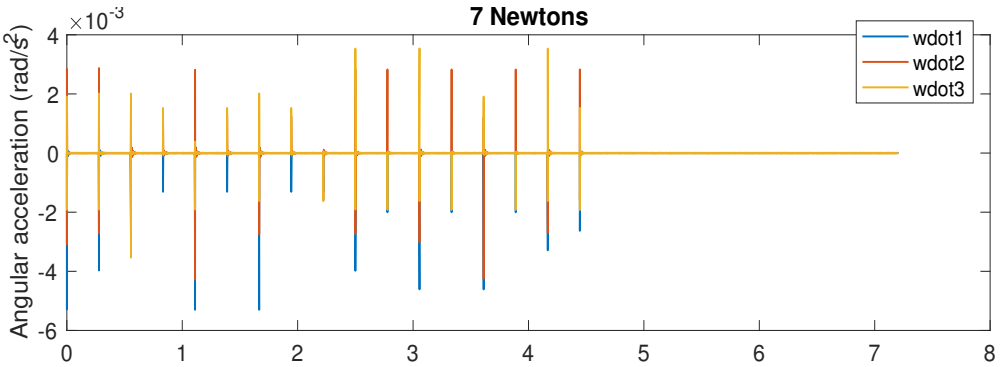

Figure 4.50: Angular acceleration introduced in each of the axis due to the commanded torque.

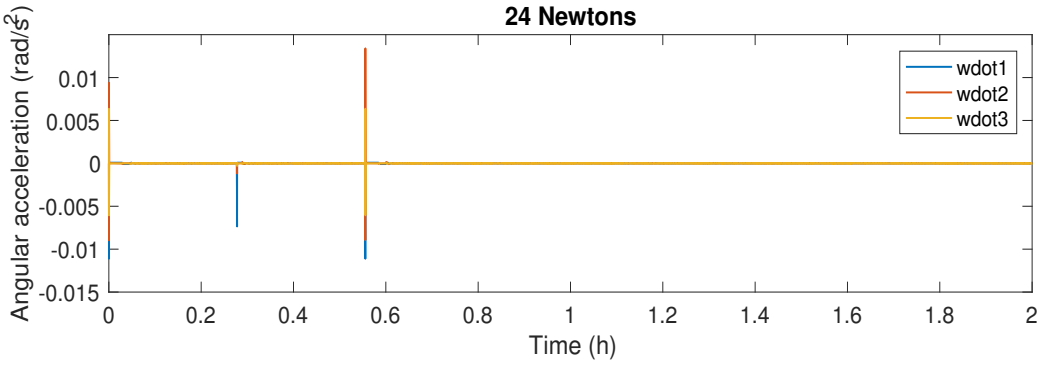

Figure 4.51: Angular acceleration introduced in each of the axis due to the commanded torque.

Finally, one more thing that needs to be study is how often the reaction wheels need to be unloaded. Unfortunately, the simulation times for this to happen where not feasible and thus no realistic data exist. For this reason, the frequency has to be approximated. Observing Figure 4.52, a typical trajectory arc can be observed. Focusing on y and z axis, it can be seen that a typical arc has a certain symmetry. This is because the spacecraft is displaced almost equally from left to right and from up to down with respect to the asteroid. Analysing Figure 4.53, this behaviour is also reproduced by the wheel speeds or by the associated angular momentum Figure 4.54, varying about ±1000 rpm the wheel speeds or about ±5 Nms the associated angular momentum. What suggest this result is that, on average, the trajectory does not influence the loading of the RW, as most of the times it cancels the induced angular momentum because of the symmetries. As the only remaining torque left is then the associated with the SRP, to locate the angular momentum in the y-axis in the way that this torque always loads the wheels would be the ideal configuration. This is because no zero-crossings would be produced. To give an approximation of the frequency of the unloading this case is used.

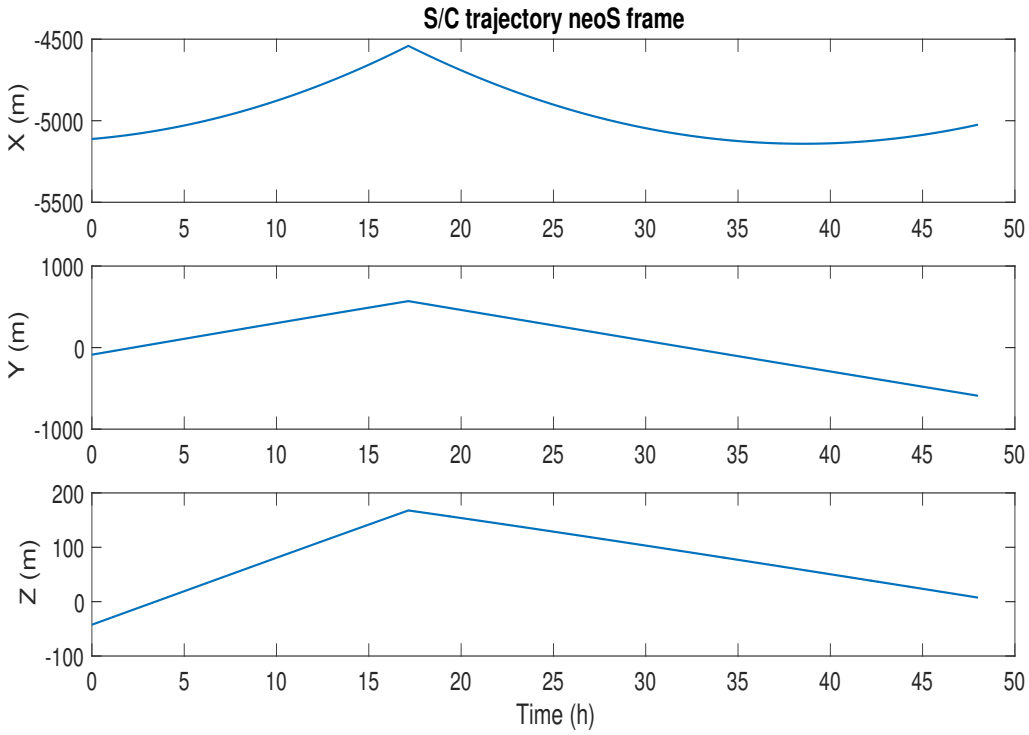

Figure 4.52: Spacecraft trajectory in the neoS frame for run no. 2 of the Monte Carlo simulation.

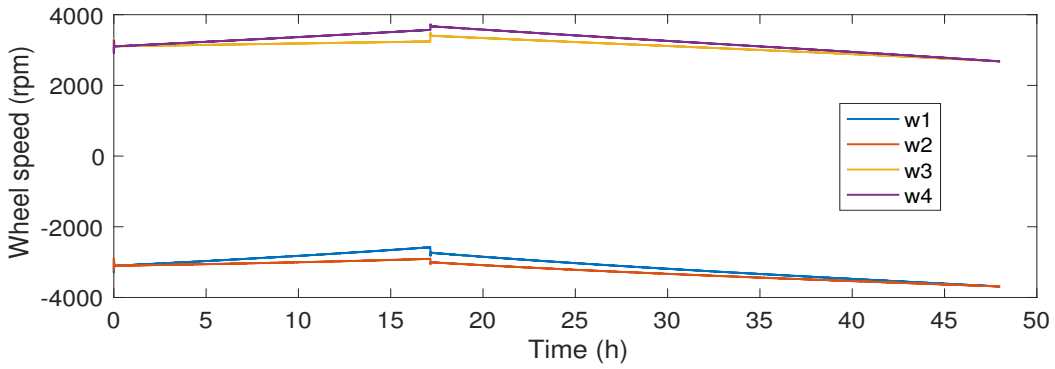

Figure 4.53: Time evolution of the reaction wheel speeds during a trajectory arc for the run no. 2 of the MC simulation.

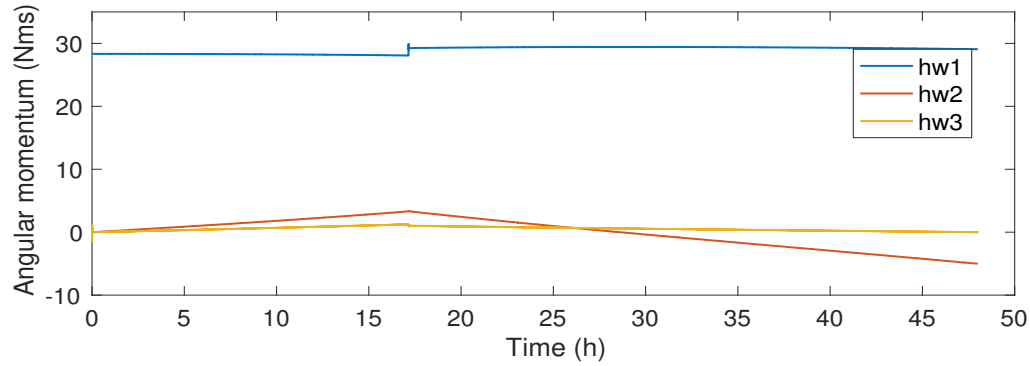

Figure 4.54: Time evolution of the angular momentum of the wheels during a trajectory arc for the run no. 2 of the MC simulation.

Imagine the wheels are in nominal speed and their speeds are configured so that they get loaded (increase their speeds) with the action of the SRP torque. Nominally, this would be: $\boldsymbol{\omega}_s = [-314.2, -314.2, 314.2, 314.2]$ rad/s or $\boldsymbol{h}_{\boldsymbol{\omega}} = [0, -38.2809, 0]$ Nms, whereas all the wheels saturated: $\boldsymbol{\omega}_s = [-628.3, -628.3, -628.3, -628.3]$ rad/s or $\boldsymbol{h}_{\boldsymbol{\omega}} = [0, -59.6417, 0]$ Nms. Assuming now that a trajectory arc can vary a maximum of 10 Nms the total angular momentum and that this variation occurs also so that the wheels get loaded (worst case), the angular momentum only reserved for the SRP torque before one of the wheels get loaded would be:

$$h_{\omega}^{\text{SRP}} = -59.6417 - (-38.2809) - (-10) \approx -10\text{Nms} \tag{4.66}$$

and knowing that the SRP torque is $\sim 1 \cdot 10^{-5}$, this implies an unloading manoeuvre each $\sim$ 12 days. Of course, this is an idealized case but offers an order of magnitude of the frequency. During the operations it might be desired to have the wheel speeds as lower as possible to save energy, this would also increase the frequency of the unloading.

Summarizing, the proposed method was originally thought for coarse pointing and thus, the advantages of controlling the torque appear. Specially for cases in which the thrust level is low, decreasing the hang-off errors caused by PWPF, the method works. Consequently, this could potentially be applied for the purpose when attitude thrusters are available of $\sim$ 1 N. However, for the momentum dumping, it is better to pre-compute the ideal sequence of firings or include onboard LP algorithms that determine the thrusting times. Although the advantages of a DNN in terms of speed could be applied (learning the distribution times instead of the distributed torques), the frequency of the manoeuvres is so low that the savings in time are not worth it. The results from this section must be then evaluated from a conservative point of view. Meaning that specially errors induced in translational motion can be decreased. Finally, in Hayabusa mission, the heads of the EP system where mounted on two axis gimbals making possible to unload momentum in those two axis without the need of chemical thruster activation. This alternative can also be explored in future work.

5

CONCLUSIONS AND RECOMMENDATIONS

Finally, in this chapter, the conclusions and recommendations for future studies are given.

5.1. CONCLUSIONS

The first part of the research objective was *to investigate the feasibility, safeness and robustness of autonomously control a spacecraft to hover in close proximity of a SSSB with diameter less than 300 m.* In this case, safeness and robustness has only been tested for 1 scenario. The spacecraft mass at arrival, Sun-NEO distance, NEO gravity field and the NEO shape have been kept constant. Further research with different scenarios are left for future studies. To answer the first part, the research questions are answered and repeated here for convenience.

1. *Is it feasible to hover autonomously around 2001 QC34 in a safe and robust way with the current baseline spacecraft?*
    1.1. *What are the forces that drive the motion of the spacecraft and how is the spacecraft affected by these ones?*
    1.2. *Which is the distance recommended to hover in a safe way?*
    1.3. *Is the opNav system able to allow hovering manoeuvres with an accuracy and update rate enough to ensure safe conditions?*
    1.4. *Is the control algorithm robust enough to deal with the operational conditions?*

The conclusions drawn in terms of these questions are given here:

- The motion of the spacecraft was determined to be mainly driven by the SRP for both translational and rotational motion. For the translational motion, the SRP pushes the spacecraft towards the NEO working as a solar sail. This effect can be used to bound the motion radially outwards. For the translational motion, the effect is almost negligible as the bias introduced due to the SRP torque is 10 times lower that other sources of error. The reason for this is in part due to the symmetry of the spacecraft, which contributes to reduce the torque. Regarding the gravitational effects, the low gravity field of the NEO forced the spacecraft to adopt a hovering strategy, as terminator orbits, although feasible at low altitudes, were strongly susceptible to velocity variations and definitely impossible using the chemical propulsion thrusters available on board. Furthermore, the velocity performance error of the translational navigation was of the same order than the ΔV needed for escaping the orbit, making impossible the use of terminator orbits. The gravity torque was found to be negligible for the distances used to hover.

- In terms of robustness and safeness, the ideal distance to hover the NEO is at ~ 5 km, as the body can be well located in the image (1/3) and the gravity field is low enough to not require big amounts of ΔV. Also the distance to the asteroid allow certain manoeuvrability before crashing in case of failure (at least one day).

- The frequency of the navigation system (60 s) was found to be enough for the requirements of the mission, as it allows to keep the spacecraft within the established performance requirements. If the overshooting wants to be decreased, predictive navigation could be developed. However, a reduction of the frequency will decrease the error associated with the attitude guidance, as the difference between two consecutive states will be smaller.

- With the only use of a monocamera and a star tracker, the attitude of the spacecraft can be obtained with a level of robustness typical for a space mission. However, in terms of safeness the operation of the star tracker might be limited when translational manoeuvres are performed. Limiting the torques introduced into the system will fix this problem.

It was found to be feasible to hover autonomously in a safe and robust way with the current baseline spacecraft. The only aspect in which these conditions might suffer refer to the translational manoeuvres. These must be done as smoothly as possible. To do this, one option could be to replace the current chemical thrusters by others with less thrust, such as in Rosetta and OSIRIS-REx missions where 10 and 4.5 N thrusters are used respectively. This also allows more accurate manoeuvres.

Once it was demonstrated to be feasible with a certain level of safeness and robustness, the second part of the research, *the performance*, was evaluated. The conclusions are drawn below and here the research questions to answer are repeated.

1. *What is the performance of the GNC system?*

   1.1. *Does the GNC system ensure the minimum performance requirements?*

   1.2. *What is the autonomy of the spacecraft and how many manoeuvres per day are required?*

   1.3. *What is the ΔV needed to hover 2001 QC34?*

   1.4. *What is the nominal pointing performance?*

   1.5. *What is the impact of external disturbances on pointing performance?*

   1.6. *What is the impact of sensors and actuators on pointing performance?*

   1.7. *What is the impact of orbital and momentum dumping manoeuvres on pointing performance?*

- Except NS-GNC-05 that is sometimes violated during translational manoeuvres, the rest of the performance requirements are within the limits established.

- Classical hovering strategies reflection/inversion were evaluated showing that they are not suitable for hovering when the amount of commands want to be minimized. This is caused by two factors: the geometry and lateral accelerations. The geometrical one is related with the convexity of the surfaces that tend to force the spacecraft to hit the walls in a short period of time or even provoke that it gets stuck on them. Two solve this problem, three new strategies were introduced, two based on deadband control and one based on a Lyapunov control function. The first solution based on reflecting the velocity always towards the center solves the problem but offers standard performance (1 manoeuvre per day). The second one proposed, based on controlling the hysteresis value, suffers from thruster errors and momentum dumping as the control strategy is based also in reflecting the incoming velocity. However, with a disposition of the thrusters specially located for hovering manoeuvres and momentum dumping, this method could be an attractive alternative. Finally, the last method, for being based in a Lyapunov control function is more able to deal with the uncertainties and thus was the one selected. It is important to highlight that hysteresis control represented an improvement of close to a 100% from the starting point (1 manoeuvre per day) whereas the Lyapunov one, improved around 50%. It was also shown that with larger control boxes the amount of propellant was reduced. For example for the case of the Lyapunov controller, an increase of the control box of the ~ 30% is equivalent to save ~ 8% of propellant. The required velocity budget was estimated to be about 0.02-0.03 cm/day. Specially, when using reflection method concave boundary surfaces might help to reduce the above mentioned problem.

- The absolute pointing performance was found to be below the one from Rosetta mission with a certain margin (total APE of 0.15 deg, or distributed per axis [0.005, 0.01, 0.01] deg). This margin was in part achieved by the assumption that the star tracker has an update rate of 16 Hz. However, this value

might increase up to 1 Hz, which may bring the pointing performance above the specified limit. The use of the redundant star trackers and the inclusion of a gyroscope might mitigate this problem. It is recommended to further study these issues.

- The impact of the SRP torque into the pointing performance was found to be $-1.6855 \cdot 10^{-6}$ rad at 1 au in the BFF y-axis. This was the largest interaction of the environment to the pointing performance.
- One of the main sources of noise was found to be the one due to the gyroscopic term, in particular the one coming from the angular momentum of the reaction wheels. Aligning the angular momentum to another axis will decrease the noise in that axis. The choice must also be based in the angular velocity of the different axis. It was also found that the BFF x-axis APE is mainly driven by biases, as opposed with the other two axis that the noise is an important aspect.
- The angular momentum of the wheels was initially set up to be aligned with the BFF x-axis. If one assumes that the arcs described by the spacecraft have certain symmetry, the only external torque is the one coming from the SRP so a most appropriate choice would be to select the angular momentum of the wheels aligned with the y-axis so that the wheels get loaded avoiding zero-crossing situations. However, it is important to have in mind that for being in a rotational frame (neoS) the average motion of the spacecraft will tend to rotate the spacecraft around the positive BFF x-axis. Due to the short integration times for the attitude dynamics this effect was negligible and thus further study is recommended.
- To apply machine learning techniques and in particular DNN for thrust allocation seems to be a good idea due to its computational speed and accuracy. Moreover, as oppose to LP methods where the time spent depends on the number of iterations, the DNN outputs a solution always in a certain fixed time, no matter the complexity of the solution. However, the limitations of the method learned must be taken into account. First, if combined with PWPF the gains must be carefully tuned, increasing the complexity of the system. Second, when using large thrust levels hang-off errors induce errors in the translational motion that have to be compensated.
- It was found that the pointing performance is not achieved when manoeuvres are commanded (translational and momentum dumping), exceeding even the physical capabilities of the star trackers in some situations (translational manoeuvres). These issues can be solved locating the thrusters specially for hovering manoeuvres and allowing independent force-free torque. Furthermore, reducing the thrust level of the chemical propulsion system will increase the accuracy of the manoeuvres. Regarding the momentum unloading, the advantages of using DNNs with respect to classical approaches do not provide benefits. This is due to the fact that the frequency of the manoeuvres is not high enough to provide savings in computational time. Furthermore, pre-store nominal ideal firing times will be more robust. However, for off-nominal situations and specially if coarse pointing is required with low level thrusters, the advantages of the method can be used.

5.2. RECOMMENDATIONS

In this section, recommendations for future studies are given.

- Study different scenarios varying the mass of the spacecraft, Sun-NEO distance and NEO shape and gravity field.
- Improve the attitude simulator by including appropriate delays and signal quantization to get a more realistic environment.
- Improve the reaction wheel model, and specifically, the wheel speed feedback control by modelling the tachometer (noise, frequency sample, etc.)
- Study in depth the force/torque coupling and determine if a better allocation of the thrusters, specially located for hovering strategies, could improve the errors due to operational manoeuvres. If same configuration is chosen, a deep study regarding the thruster management function has to be done for nominal and off-nominal operations.
- More accurate analysis of the torques induced by thrusters misalignments errors and differences between the commanded thrust level and the real one. Furthermore, to determine how "smooth" a ΔV manoeuvre of a couple of cm/s can be executed.

- Study the coarse pointing with the current chemical propulsion system and the APE level achieved.
- Study if for hovering strategies, it is beneficial to select smaller chemical thrusters. This will improve the accuracy in terms of ΔV commands and coarse pointing.
- Integrate the attitude errors into the translational navigation system. So far, the attitude of the spacecraft was assumed to be perfectly known by the navigation filter.
- Simulate for longer periods of time to evaluate, in a more realistic way, how often momentum dumping manoeuvres are needed.
- Evaluate the influence of the average rotation around the Sun into the way the reaction wheels get loaded.
- Deeper study of the influence of the gyroscopic term into the pointing performance, varying the distribution of the angular momentum of the wheels and selecting the best configuration in terms of APE.
- Increase the update rate of the star tracker and determine when the established APE limits are exceed and if it is better to include a gyroscope to mitigate this problem.
- Study the momentum unloading using the gimbal EP system as done in Hayabusa mission and if this approach increases the amount of manoeuvres per day.
- It was also noticed that the lateral accelerations due to the relative motion between NEO-spacecraft are a couple of orders of magnitude lower than the nominal acceleration due to SRP. If the camera is mounted into a gimbal system that allows to point independently to the asteroid, the lateral acceleration could be counteracted by tilting the solar panels. By doing this, almost a static radial position could be achieved.

A

2001 QC34

This appendix provides information about the baseline NEO properties, asteroid 2001 QC34 [1]. Some are known from observations carried out and others are assumed for this study. Figure A.1 shows its trajectory observing a future close approach with the Earth. This is one of the reasons why this particular asteroid has been chosen, because it could at some point in the future collide with the Earth. Table A.1 show the characteristics of the orbit together with the physical properties of the NEO.

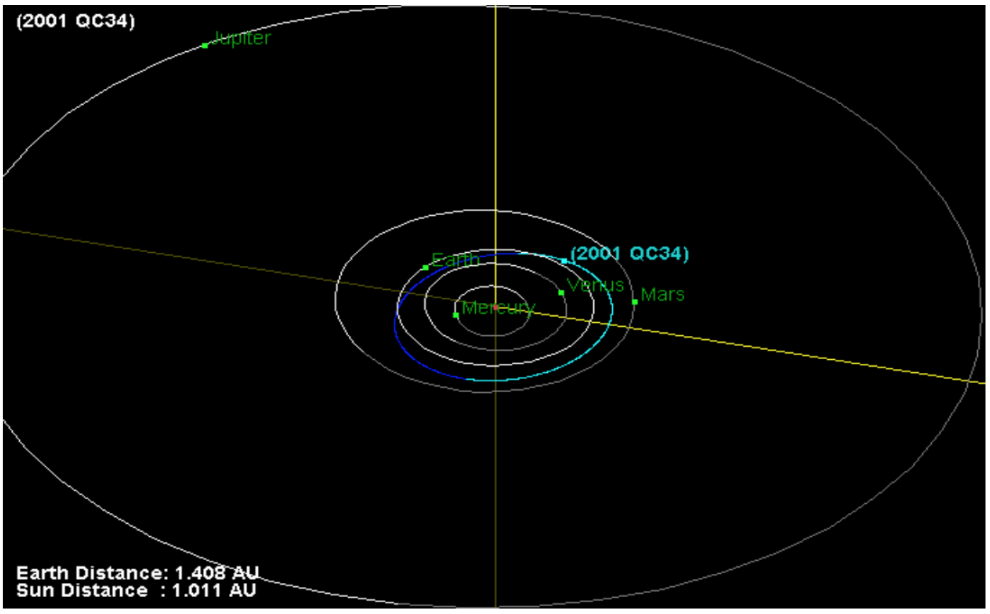

Figure A.1: Orbit trajectory of 2001 QC34 together with the closest main bodies of the solar system[1].

[1] 2001 QC34 - Reference: JPL 91 (heliocentric ecliptic J2000): https://ssd.jpl.nasa.gov/sbdb.cgi. Accessed: 22-09-2017

Table A.1: NEO physical properties and its orbital elements.
The values with an asterisk (*) are assumptions for this work[1].

Property	**Value**
Semi-major axis	1.128299427485589 au
Eccentricity	0.187484966777044
Inclination	6.235545956912984 deg
Mass	$5.88 \cdot 10^9$ kg
Spin Rate	3.655 h
Dimension(*)	230 m x 165 m x 165 m
Density(*)	2.25 g/cm^3
Pole Direction(*)	0.75 deg

B

SPACECRAFT PROPERTIES

In this appendix the spacecraft physical properties, together with the location of sensors and actuators are given. Table B.2 gives the physical properties of the spacecraft at arrival, Table B.1 shows the main properties for the optical cameras used for assumptions during this research and Tables B.3 to B.5 the location and DCMs for the sensors and actuators used onboard. In this case, the DCM relates the rotation from the local axis to the MRF (Figure B.1).

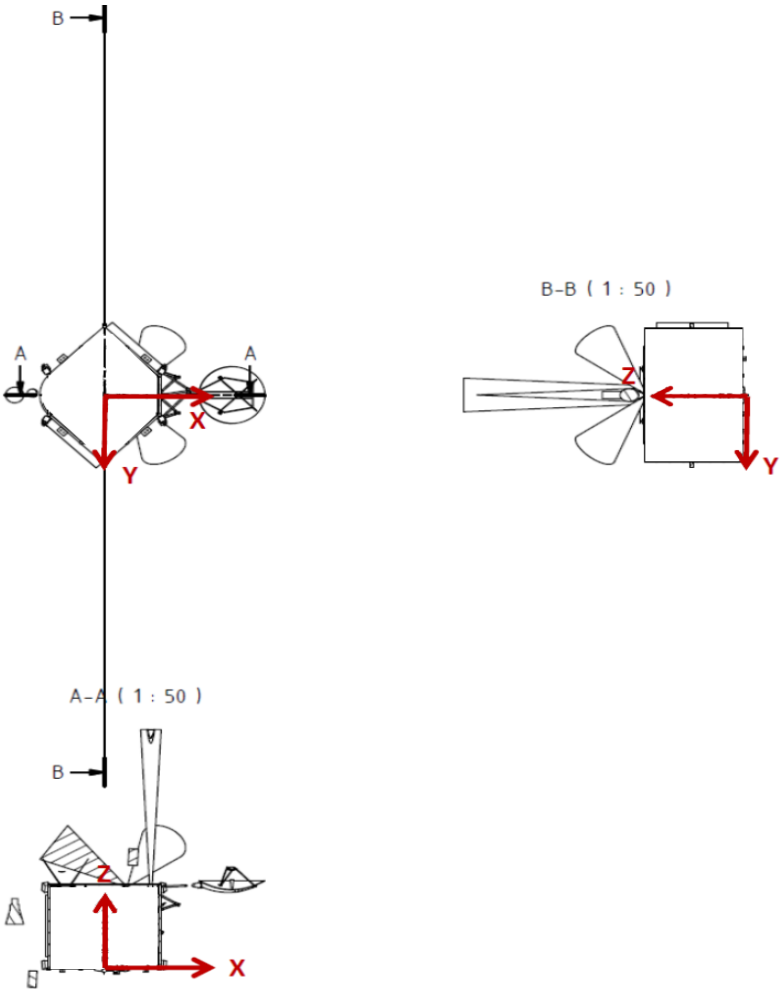

Figure B.1: Mechanical Reference Frame (Ziegler and Delchambre, 2016)

Table B.4: Reaction wheels position and orientation in the spacecraft MRF (Ziegler and Delchambre, 2016)

Unit	#	X (mm)	Y (mm)	Z (mm)	DCM		
Reaction Wheel	1	570.537	-621.202	540.894	$7.939972 \cdot 10^{-1}$	$-1.494601 \cdot 10^{-1}$	$-5.892622 \cdot 10^{-1}$
					$5.722922 \cdot 10^{-1}$	$5.107284 \cdot 10^{-1}$	$6.415902 \cdot 10^{-1}$
					$2.050608 \cdot 10^{-1}$	$-8.466510 \cdot 10^{-1}$	$4.910519 \cdot 10^{-1}$
Reaction Wheel	2	570.537	-621.202	1491.789	$7.939972 \cdot 10^{-1}$	$1.494601 \cdot 10^{-1}$	$-5.892622 \cdot 10^{-1}$
					$5.722922 \cdot 10^{-1}$	$-5.107284 \cdot 10^{-1}$	$6.415902 \cdot 10^{-1}$
					$-2.050608 \cdot 10^{-1}$	$-8.466510 \cdot 10^{-1}$	$-4.910519 \cdot 10^{-1}$
Reaction Wheel	3	-570.537	-621.202	1491.789	$7.939972 \cdot 10^{-1}$	$-1.494601 \cdot 10^{-1}$	$5.892622 \cdot 10^{-1}$
					$-5.722922 \cdot 10^{-1}$	$-5.107284 \cdot 10^{-1}$	$6.415902 \cdot 10^{-1}$
					$2.050608 \cdot 10^{-1}$	$-8.466510 \cdot 10^{-1}$	$-4.910519 \cdot 10^{-1}$
Reaction Wheel	4	-570.537	-621.202	540.894	$7.939972 \cdot 10^{-1}$	$1.494601 \cdot 10^{-1}$	$5.892622 \cdot 10^{-1}$
					$-5.722922 \cdot 10^{-1}$	$5.107284 \cdot 10^{-1}$	$6.415902 \cdot 10^{-1}$
					$-2.050608 \cdot 10^{-1}$	$-8.466510 \cdot 10^{-1}$	$4.910519 \cdot 10^{-1}$

Table B.1: Onboard cameras optical properties.

Narrow angle camera (NAC)	
Pixel Matrix	2048 × 2048
Field of View (FOV)	10.3°
Wide angle camera (WAC)	
Pixel Matrix	1024 × 1024
Field of View (FOV)	21.8°

Table B.2: Physical properties of the spacecraft at arrival at 2001 QC34

Property	Value		
Mass	628 kg		
Fuel at arrival	50 kg		
Box size	2.0 × 2.0 × 1.6 m		
Solar panel surface	2 × (6.0 m × 1.2 m)		
Antenna surface	$0.275^2 \pi$ m^2		
Matrix of Inertia (**J**) (kg m^2)	2352	0	-11
	0	428	0
	-11	0	2496
Location CoM (mm)	19.4	0.0	829.0

Table B.3: Star tracker position and orientation in the spacecraft MRF (Ziegler and Delchambre, 2016)

Unit	#	X (mm)	Y (mm)	Z (mm)	DCM		
Star Tracker Head	1	383.245	0	1620.943	$-9.127035 \cdot 10^{-1}$	$1.569810 \cdot 10^{-2}$	$4.083207 \cdot 10^{-1}$
					$3.054316 \cdot 10^{-1}$	$-6.376001 \cdot 10^{-1}$	$7.072323 \cdot 10^{-1}$
					$2.714475 \cdot 10^{-1}$	$7.702075 \cdot 10^{-1}$	$5.771451 \cdot 10^{-1}$
Star Tracker Head	2	383.245	0	1620.943	$-8.915736 \cdot 10^{-1}$	$-1.958842 \cdot 10^{-1}$	$4.083207 \cdot 10^{-1}$
					$-1.733077 \cdot 10^{-1}$	$-6.854099 \cdot 10^{-1}$	$-7.072323 \cdot 10^{-1}$
					$4.184028 \cdot 10^{-1}$	$-7.013148 \cdot 10^{-1}$	$5.771451 \cdot 10^{-1}$
Star Tracker Head	3	383.245	0	1620.943	$5.432950 \cdot 10^{-2}$	$-5.745823 \cdot 10^{-1}$	$-8.166415 \cdot 10^{-1}$
					$9.955594 \cdot 10^{-1}$	$9.413490 \cdot 10^{-2}$	0
					$7.687440 \cdot 10^{-2}$	$-8.130152 \cdot 10^{-1}$	$5.771451 \cdot 10^{-1}$

Table B.5: CMP position and orientation of the thrusters in the spacecraft MRF (Ziegler and Delchambre, 2016)

Unit	#	X (mm)	Y (mm)	Z (mm)	DCM		
CMP Thruster	1	700.778	704.780	120	$7.071067 \cdot 10^{-1}$ $-7.071067 \cdot 10^{-1}$ 0	$-7.071067 \cdot 10^{-1}$ $-7.071067 \cdot 10^{-1}$ 0	0 0 -1
CMP Thruster	2	-700.778	704.780	120	$-7.071067 \cdot 10^{-1}$ $-7.071067 \cdot 10^{-1}$ 0	$-7.071067 \cdot 10^{-1}$ $7.071067 \cdot 10^{-1}$ 0	0 0 -1
CMP Thruster	3	700.778	-704.780	120	$7.071067 \cdot 10^{-1}$ $7.071067 \cdot 10^{-1}$ 0	$7.071067 \cdot 10^{-1}$ $-7.071067 \cdot 10^{-1}$ 0	0 0 -1
CMP Thruster	4	-700.778	-704.780	120	$-7.071067 \cdot 10^{-1}$ $7.071067 \cdot 10^{-1}$ 0	$7.071067 \cdot 10^{-1}$ $7.071067 \cdot 10^{-1}$ 0	0 0 -1
CMP Thruster	5	945.861	433.044	1586.656	$6.550650 \cdot 10^{-2}$ $4.975051 \cdot 10^{-1}$ $-8.649841 \cdot 10^{-1}$	$-8.806493 \cdot 10^{-1}$ $4.364392 \cdot 10^{-1}$ $1.843299 \cdot 10^{-1}$	$4.692181 \cdot 10^{-1}$ $7.496728 \cdot 10^{-1}$ $4.667171 \cdot 10^{-1}$
CMP Thruster	6	945.861	433.044	119.064	$6.550650 \cdot 10^{-2}$ $1.653878 \cdot 10^{-1}$ $9.840506 \cdot 10^{-1}$	$8.806493 \cdot 10^{-1}$ $-4.733063 \cdot 10^{-1}$ $2.092453 \cdot 10^{-1}$	$4.692181 \cdot 10^{-1}$ $8.652328 \cdot 10^{-1}$ $-1.766533 \cdot 10^{-1}$
CMP Thruster	7	945.861	-461.064	1586.656	$6.550650 \cdot 10^{-2}$ $-4.927057 \cdot 10^{-1}$ $-8.677268 \cdot 10^{-1}$	$8.806493 \cdot 10^{-1}$ $4.374537 \cdot 10^{-1}$ $-1.819093 \cdot 10^{-1}$	$4.692181 \cdot 10^{-1}$ $-7.522468 \cdot 10^{-1}$ $4.625570 \cdot 10^{-1}$
CMP Thruster	8	945.861	-433.044	119.064	$6.550650 \cdot 10^{-2}$ $-1.653878 \cdot 10^{-1}$ $9.840506 \cdot 10^{-1}$	$-8.806493 \cdot 10^{-1}$ $-4.733063 \cdot 10^{-1}$ $-2.092450 \cdot 10^{-2}$	$4.692181 \cdot 10^{-1}$ $-8.652328 \cdot 10^{-1}$ $-1.766533 \cdot 10^{-1}$
CMP Thruster	9	-945.861	-461.113	1589.126	$-6.550650 \cdot 10^{-2}$ $-4.979282 \cdot 10^{-1}$ $-8.647406 \cdot 10^{-1}$	$8.806493 \cdot 10^{-1}$ $-4.363490 \cdot 10^{-1}$ $1.845434 \cdot 10^{-1}$	$-4.692181 \cdot 10^{-1}$ $-7.494444 \cdot 10^{-1}$ $4.670838 \cdot 10^{-1}$
CMP Thruster	10	-945.861	-433.044	119.064	$-6.550650 \cdot 10^{-2}$ $-1.653878 \cdot 10^{-1}$ $9.840506 \cdot 10^{-1}$	$-8.806493 \cdot 10^{-1}$ $4.733063 \cdot 10^{-1}$ $2.092450 \cdot 10^{-2}$	$-4.692181 \cdot 10^{-1}$ $-8.652328 \cdot 10^{-1}$ $-1.766533 \cdot 10^{-1}$
CMP Thruster	11	-945.861	460.488	1589.792	$-6.550650 \cdot 10^{-2}$ $4.924671 \cdot 10^{-1}$ $-8.678623 \cdot 10^{-1}$	$-8.806493 \cdot 10^{-1}$ $-4.375037 \cdot 10^{-1}$ $-1.817890 \cdot 10^{-1}$	$-4.692181 \cdot 10^{-1}$ $7.523740 \cdot 10^{-1}$ $4.623502 \cdot 10^{-1}$
CMP Thruster	12	-945.861	433.044	119.064	$-6.550650 \cdot 10^{-2}$ $1.653878 \cdot 10^{-1}$ $9.840506 \cdot 10^{-1}$	$8.806493 \cdot 10^{-1}$ $4.733063 \cdot 10^{-1}$ $-2.092450 \cdot 10^{-2}$	$-4.692181 \cdot 10^{-1}$ $8.652328 \cdot 10^{-1}$ $-1.766533 \cdot 10^{-1}$

BIBLIOGRAPHY

Abadi *et al.* TensorFlow: "Large-Scale Machine Learning on Heterogeneous Systems", 2015. URL https://www.tensorflow.org/. Software available from tensorflow.org.

Ankersen, F., Wu, S., Aleshin, A., Vankov, A., and Volochinov, V. "Optimization of Spacecraft Thruster Management Function". *Journal of Guidance, Control, and Dynamics*, vol. 28, no. 6:pp. 1283–1290, 2005.

Antreasian, P. G., Moreau, M., Jackman, C., Williams, K., Page, B., and Leonard, J. M. "OSIRIS-REx Orbit Determination Covariance Studies at Bennu". 2016.

Azor, R., Bar-Itzhack, I. Y., Deutschmann, J. K., and Harman, R. R. "Angular-Rate Estimation Using Delayed Quaternion Measurements". *Journal of Guidance, Control, and Dynamics*, vol. 24, no. 3:pp. 436–443, 2001.

Bae, J., Kim, Y., and Kim, H. S. "Satellite Attitude Determination and Estimation Using Two Star Trackers". In *Guidance, Navigation, and Control Conference, Toronto, Ontario, Canada*, 2010.

Bar-Itzhack, I. Y. "Classification of algorithms for angular velocity estimation". *Journal of Guidance, Control, and Dynamics*, vol. 24, no. 2:pp. 214–218, 2001.

Bar-Itzhack, I. Y., Harman, R. R., and Thienel, J. K. "On the extraction of angular velocity from attitude measurements". 2006.

Bayard, D. S. "High-Precision Three-Axis Pointing and Control". *Encyclopedia of Aerospace Engineering*, 2010. Available: http://dx.doi.org/10.1002/9780470686652.eae300.

Bellei, G., Cano, J. L., and Sánchez, M. "Operational Orbiting Strategies About Minor Bodies". In *21st International Symposium on Space Flight Dynamics ISSFD*, 2009.

Bergmann, E. V., Croopnick, S. R., Turkovich, J. J., and Work, C. C. "An Advanced Spacecraft Autopilot Concept". *Journal of Guidance and Control*, vol. 2, no. 3:p. 161, 1979.

Blanke, M. and Larsen, M. B. "Satellite Dynamics and Control in a Quaternion Formulation". Technical report, Technical University of Denmark, Department of Electrical Engineering, 2010.

Broschart, S. B. and Scheeres, D. J. "Boundedness of Spacecraft Hovering Under Dead-Band Control in Time-Invariant Systems". *Journal of Guidance, Control, and Dynamics*, vol. 30, no. 2:pp. 601–610, 2007.

Carrara, V. and Kuga, H. K. "Torque and Speed Control Loops Of A Reaction Wheel". In *11th International Conference on Vibration Problems*, 2013.

Challa, M. S. "Simultaneous Estimation of Attitude and Markov-Modeled Rate Corrections of Gyroless Spacecraft". *Journal of Guidance, Control, and Dynamics*, 2017.

Cheng, A. F. "Near Earth asteroid rendezvous: mission summary". *Asteroids III*, pages pp. 351–366, 2002.

Chesley, S. R., Farnocchia, D., Nolan, M. C., Vokrouhlickỳ, D., Chodas, P. W., Milani, A., Spoto, F., Rozitis, B., Benner, L. A. M., Bottke, W. F., et al. "Orbit and Bulk Density of the OSIRIS-REx Target Asteroid (101955) Bennu". *Icarus*, vol. 235:pp. 5–22, 2014.

Cocci, E. "Optimal Control of Reaction Wheels Disturbance Transients". *TU Delft, Available: http://resolver.tudelft.nl/uuid:1465fa5a-9d68-4d20-97db-1133405b9579*, 2016.

Dankowicz, H. "Some Special Orbits in the Two-Body Problem with Radiation Pressure". *Celestial Mechanics and Dynamical Astronomy*, vol. 58, no. 4:pp. 353–370, 1994.

Delchambre, S. "Closed-Loop Transfer Functions and Bandwidth Notes." Airbus Defence and Space. Internal document., 2017a.

Delchambre, S. Reaction wheels friction model. Personal communication: internal email. Airbus Defence and Space., 2017b.

Delchambre, S., Ziegler, T., Falke, A., Johann, U., Willich, G., and Janschek, K. "Measurement Strategy of the Momentum Enhancement Beta-Factor for Near Earth Object Mitigation Missions". In *Aerospace Conference, 2017 IEEE*, pages 1–9. IEEE, 2017a.

Delchambre, S., Ziegler, T., Johann, U., Falke, A., and Janschek, K. "Landmark Based Pose Estimation for Autonomous Inertial Hovering around Small Solar System Bodies". *10th ESA Guidance Navigation and Control Conference, Salzburg, Austria*, 2017b.

ECSS, Secretariat. ECSS-E-HB-60-10A - Control Performance Guidelines. *European Cooperation for Space Standardization*, 2014.

Fab Labs Central, MIT. "Noise in Physical Systems. Lecture Notes."

Feng, J., Noomen, R., and Yuan, J. "Orbital Motion in the Vicinity of the Non-collinear Equilibrium Points of a Contact Binary Asteroid". *Planetary and Space Science*, vol. 117:pp. 1–14, 2015.

Fiebrich, H., Martinez Ripoll, D., Noyes, J., Rouquet, J., and Stramaccioni, D. "ROSETTA: Mission Commissioning Results Review Spacecraft Performance Report". Technical report, European Space Agency, 2004.

Glorot, X., Bordes, A., and Bengio, Y. "Deep Sparse Rectifier Neural Networks". In *Proceedings of the Fourteenth International Conference on Artificial Intelligence and Statistics*, pages 315–323, 2011.

Harbulot, Q. "Relative Navigation at Close Proximity of Small Solar System Bodies". *Politecnico di Milano*, 2017.

Holtkamp, G. C. MSc Thesis. *TU Delft, Available: http://resolver.tudelft.nl/uuid:68c13b85-9dfe-42e0-bb9f-7982d0a1a108*, 2014.

Kaula, W. M. *Theory of Satellite Geodesy: Applications of Satellites to Geodesy*. Courier Corporation, 2013.

Keskar, N. S., Mudigere, D., Nocedal, J., Smelyanskiy, M., and Tang, P. T. P. "On Large-Batch Training for Deep Learning: Generalization Gap and Sharp Minima". *arXiv preprint arXiv:1609.04836*, 2016.

Kingma, D. and Ba, J. "Adam: A Method for Stochastic Optimization". *arXiv preprint arXiv:1412.6980*, 2014.

Kominato, T., Matsuoka, M., Uo, M., and Hashimoto, J., T.and Kawaguchi. "Optical Hybrid Navigation and Station Keeping Around Itokawa". In *AIAA/AAS Astrodynamics Specialist Conference and Exhibit*, page 6535, 2006.

Krovel, T. D. "Optimal Tuning of PWPF Modulator for attitude Control". *Norwegian University of Science and Technology*, 2005.

Kubota, T., Hashimoto, T., Kawaguchi, J., Uo, M., and Shirakawa, K. "Guidance and Navigation of Hayabusa Spacecraft for Asteroid Exploration and Sample Return Mission". In *SICE-ICASE, 2006. International Joint Conference*, pages 2793–2796. IEEE, 2006.

Lantukh, D., Russell, R. P., and Broschart, S. B. "Heliotropic Orbits at Asteroids: Zonal Gravity Perturbations and Application at Bennu". *Advances in the Astronautical Sciences, Spaceflight Mechanics 2015*, vol. 155, 2015.

Lautenschlager, G. "The Rosetta Mission Challenging Navigation in Space". Airbus Defence & Space, 2015. ESA GNCISB Workshop.

Lenoir, B., Lévy, A., Foulon, B., Lamine, B., Christophe, B., and Reynaud, S. "Electrostatic Accelerometer with Bias Rejection for Gravitation and Solar System Physics". *Advances in Space Research*, vol. 48, no. 7:pp. 1248–1257, 2011.

Markley, F. L. and Crassidis, J. L. *Fundamentals of spacecraft attitude determination and control*, volume 33. Springer, 2014. doi: 10.1007/978-1-4939-0802-8.

Maurice, M. and Delchambre, S. "Spacecraft-NEO-State Determination Techniques". *TU Berlin*, 2016.

McClelland, R. S. "Spacecraft Attitude Control System Performance Using Pulse-Width Pulse-Frequency Modulated Thrusters." Technical report, Naval Postgraduate School Monterey CA, 1994.

Miller, J. K., Konopliv, A. S., Antreasian, P. G., Bordi, J. J., Chesley, S., Helfrich, C. E., Owen, W. M., Wang, T. C., Williams, B. G., Yeomans, D. K., et al. "Determination of Shape, Gravity, and Rotational State of Asteroid 433 Eros". *Icarus*, vol. 155, no. 1:pp. 3–17, 2002.

Muñoz, P., Budnik, F., Godard, B., Morley, T., Companys, V., Herfort, U., and Casas, C. "Preparations and Strategy for Navigation during Rosetta Comet Phase". In *Proceedings 23rd International Symposium on Space Flight Dynamics-23rd ISSFD, Pasadena, USA*, 2012.

NASA/NAIF. "An Overview of Reference Frames and Coordinate Systems in the SPICE Context". NASA, 2017.

Oshman, Y. and Markley, F. L. "Sequential attitude and attitude-rate estimation using integrated-rate parameters". *Journal of Guidance, Control, and Dynamics*, vol. 22, no. 3:pp. 385–394, 1999.

Ott, T., Benoit, A., Van den Braembussche, P., and Fichter, W. "ESA Pointing Error Engineering Handbook". *8th International ESA conference on Guidance, Navigation and control Systems, Karlovy Vary, Czech*, 2011.

Quadrelli, M. B., Wood, L. J., Riedel, J. E., McHenry, M. C., Aung, M., Cangahuala, L. A., Volpe, R. A., Beauchamp, P. M., and Cutts, J. A. "Guidance, Navigation, and Control Technology Assessment for Future Planetary Science Missions". *Journal of Guidance, Control, and Dynamics*, vol. 38, no. 7:pp. 1165–1186, 2015.

Razgus, B., Mooij, E., and Choukroun, D. "Relative Navigation in Asteroid Missions: A Dual Quaternion Approach". *AIAA Guidance, Navigation, and Control Conference*, 2016.

Richter, K. and Keller, H. U. "On the Stability of Dust Particle Orbits Around Cometary Nuclei". *Icarus*, vol. 114, no. 2:pp. 355–371, 1995.

Rubincam, D. P. "Radiative Spin-Up and Spin-Down of Small Asteroids". *Icarus*, vol. 148, no. 1:pp. 2–11, 2000.

Ruder, S. "An Overview of Gradient Descent Optimization Algorithms". *arXiv preprint arXiv:1609.04747*, 2016.

Sánchez-Sánchez, C. and Izzo, D. "Real-time Optimal Control Via Deep Neural Networks: Study on Landing Problems". *arXiv preprint arXiv:1610.08668*, 2016.

Santo, A. G., Lee, S. C., and Gold, R. E. "NEAR Spacecraft and Instrumentation". *Journal of the Astronautical Sciences*, vol. 43, no. 4:pp. 373–397, 1995.

Scheeres, D. J. "Satellite Dynamics about Small Bodies: Averaged Solar Radiation Pressure Effects1". *Ann Arbor*, vol. 1001:pp. 48109–2140, 1999.

Scheeres, D. J. "Orbit Mechanics About Asteroids and Comets". *Journal of Guidance, Control, and Dynamics*, vol. 35, no. 3:pp. 987, 2012.

Scheeres, D. J. "Close proximity dynamics and control about asteroids". In *American Control Conference (ACC), 2014*, pages 1584–1598. IEEE, 2014.

Scheeres, D. J. *Orbital Motion in Strongly Perturbed Environments: Applications to Asteroid, Comet and Planetary Satellite Orbiters*. Springer, 2016.

Scheeres, D. J. and Marzari, F. "Spacecraft Dynamics in the Vicinity of a Comet". *Journal of the Astronautical Sciences*, vol. 50, no. 1:pp. 35–52, 2002.

Storn, R. and Price, K. "Differential Evolution - A Simple and Efficient Heuristic for Global Optimization over Continuous Spaces". *Journal of global optimization*, vol. 11, no. 4:pp. 341–359, 1997.

Takahashi, Y. and Scheeres, D. J. "Small-Body Postrendezvous Characterization Via Slow Hyperbolic Flybys". *Journal of Guidance, Control and Dynamics*, vol. 34, no. 6:pp. 1815–1827, 2011.

Trawny, N. and Roumeliotis, S. I. "Indirect Kalman filter for 3D attitude estimation". *University of Minnesota, Department of Computer Science & Engineering Technical Report*, vol. 2:2005–002, 2005.

Uo, M., Shirakawa, K., Hashimoto, T., Kubota, T., and Kawaguchi, J. "Attitude control challenges and solutions for Hayabusa spacecraft". In *Proceedings of 16th Workshop on JAXA Astrodynamics and Flight Mechanics*, page I2, 2006.

Vallado, D. A. *Fundamentals of Astrodynamics and Applications*, volume 12. Springer Science & Business Media, 2001.

Vetrisano, M. and Cano, J. L. "Asteroid Proximity GNC Assessment through High-Fidelity Asteroid Deflection Evaluation Software (HADES)".

Wakker, K. F. *Fundamentals of Astrodynamics*. TU Delft Library, http://resolver.tudelft.nl/uuid:3fc91471-8e47-4215-af43-718740e6694e, 2015.

Werner, R. A. and Scheeres, D. J. "Exterior Gravitation of a Polyhedron Derived and Compared with Harmonic and Mascon Gravitation Representations of Asteroid 4769 Castalia". *Celestial Mechanics and Dynamical Astronomy*, vol. 65, no. 3:pp. 313–344, 1996.

Wie, B. *Space Vehicle Dynamics and Control, 2nd ed.* AIAA, 1998.

Yamashita, T., Uo, M., and Hashimoto, T. "Nonlinear Six-Degree-of-Freedom Control for Flexible Spacecraft". *IFAC Proceedings Volumes*, vol. 34, no. 15:pp. 344–349, 2001.

Yeomans, D. K. "Asteroid 433 Eros: The Target Body of the NEAR Mission". *Journal of the Astronautical Sciences*, 1995.

Ziegler, T. and Delchambre, S. NEOShield-2 - GNC Verification ICD. NEOShield-2 Consortium, 2016.